UNIVERSITÀ
DEGLI STUDI
DI PADOVA

Sede Amministrativa: Università degli Studi di Padova

Dipartimento di Ingegneria dell'informazione

CORSO DI DOTTORATO DI RICERCA IN: Ingegneria dell'informazione
CURRICOLO: Scienza e Tecnologia dell'informazione
CICLO: XXXI

Development of spectroscopic instrumentation for Ultrafast pulses in the XUV domain

Coordinatore: Ch.mo Prof. Andrea Neviani
Supervisore: Ch.mo Dr. Luca Poletto

Dottorando : Paolo Miotti

UNIVERSITÀ DEGLI STUDI DI PADOVA

DOCTORAL THESIS

Development of spectroscopic instrumentation for Ultrafast pulses in the XUV domain

---

Autor:
Paolo MIOTTI

Supervisor:
Dr. Luca POLETTO

Dipartimento di ingegneria dell'informazione

November 27, 2018

UNIVERSITÀ DEGLI STUDI DI PADOVA

Abstract

Dipartimento di ingegneria dell'informazione

DOCTORAL THESIS

Development of spectroscopic instrumentation for Ultrafast pulses in the XUV domain

by Paolo MIOTTI

In questa dissertazione viene presentato il lavoro realizzato nell'ambito dello sviluppo di strumentazione spettroscopica per impulsi ultrabrevi nell'XUV. Le attività relative all'installazione, allo sviluppo e alla caratterizzazione di strumentazione ultraveloce per la manipolazione, il condizionamento e la rivelazione di impulsi ultrabrevi sono descritte in dettaglio. Inoltre, i progressi tecnici e scientifici raggiunti e i risultati sperimentali ottenuti sono riportati e discussi.

In this dissertation the work performed in the framework of the development of spectroscopic instrumentation for Ultrafast pulses in the XUV domain is presented. The activities on the installation, development and characterization of ultrafast instrumentation for handling, conditioning and detection of ultrashort pulses are described in detail. Moreover, the technical and scientific advances achieved, as well as the experimental results obtained, are reported and discussed.

Acknowledgements

I would like to express my immense gratitude to all the people who supported me during my PhD research. First of all, I would like to thank my super-advisor, Luca Poletto, for his constant support, patience and guidance. He gives me the great opportunity to work and gain experience on ultrafast instrumentation in the XUV/Soft X-ray domain and gives me the chance to attend this PhD course, helping me in the writing of this thesis. I am also very grateful to the National Research Council - Institute for Photonics and Nanotechnologies and to the University of Padova - Department of Electrical, Electronic and Information Engineering, for making it possible for me to attend the PhD course. Then, I would like to thank my research-group members Fabio Frassetto and Nicola Fabris. Fabio and Nicola worked with me on the installation and characterization of multiple instruments and on different topics discussed in this manuscript. I am particularly grateful to Fabio, since he gave me a huge help during the writing of this manuscript. He had the patience to read my entire thesis, giving me valuable and precious advices. During these years he also helped me to understand a lot of subjects I considered extremely difficult. He was always there to make sure I understood and I didn't do something wrong. Nicola wrote all the software used for the control of the many instruments we installed in the last three years. Thanks to both of them for all the discussions on physics and culture had during the multiple beamtimes performed in these years. I would like to acknowledge all the colleagues and scientists with whom I collaborated during this period at CNR-IFN Padova and at the multiple beamlines where I have worked at ELETTRA Sincrotrone Trieste. Thanks to Paola Zuppella, Enrico Tessarolo, Lorenzo Cocola, Alain J. Corso, Stefano Bonora at CNR-IFN Padova, for all the useful discussions had in these years. Special thanks to Marcello Coreno and colleagues - Gas-Phase Beamline @ ELETTRA; Carlo Callegari and his staff - LDM Beamline @ FERMI; Emiliano Principi and his team - EIS-TIMEX Beamline @ FERMI; Giancarlo Panaccione, Federico Cilento, Riccardo Cucini and their guys at the beamlines T-REX and ULTRASPIN @ FERMI; Nicola Zema and his partners - CIPO Beamline @ ELETTRA. Last but not least, the FERMI Machine Physics Team, in particular Giovanni De Ninno and Luca Giannessi. I have to mention also other people that worked with me at Elettra and that have been extremely helpful by allowing me to use some of their data and images: David Gauthier, Tommaso Pincelli, Damir Kopić, Gian Marco Pierantozzi and Laura Foglia. It wouldn't be possible not to thank my colleague and big friend Cesare Grazioli (also because I think he pretend a mention in this thesis). Cesare offered me a bed and a meal on several occasions during my stays in Trieste. I think I'm not overdoing it if I say he's like my 50 years old mommy. Let me also thank my colleagues Michele Di Fraia and Carlo Spezzani for the friendship they have shown me over the years. Of course, I am also extremely grateful to all the other colleagues met at CNR-IFN Padova and at Elettra Sincrotrone Trieste not mentioned here. I express my gratitude for the hospitality I received from my Chinese colleagues headed by Yongbing Xu during the time I spent at the University of

Nanjing. Thanks so much to Zhonghui Nie and Yao Li; first of all for all the help they gave me there and then for consenting me to use some of their material for this thesis. I would also like to thank the FLASH Photon Diagnostics and Controls group at DESY: in particular Stefan Düsterer and Rosen Ivanov, who made me feel at ease during my three month period in Hamburg. I must also thank the "American" team headed by Royce Lam and Craig Schwartz for giving me the chance to participate to the experiments they conceived and for letting me show some of the data of the experiments in this manuscript. Thanks so much also to all the other people who have supported me outside of the laboratories. My special thanks to my family who always believed in me and in my skills. Thank you very much to Maria and Tiziano for all the support and the help they gave me in these years. I also owe a great deal of gratitude to my friends, those deserving of a mention include Francesco, Bruno, Juri, Anna Viola, Marco, Luca, Daniele, Andrea P., Giulio, Umberto, Andrea C., Enrico, Raimondo, Pippo. I have learned so much about life from each one them. Thanks for making me laugh so much and for all the wonderful time spent together. Finally, I would like to immensely thank my girlfriend Livia, for having brought so much patience during this period and during the writing of this thesis. She encouraged me and she helped me to face the difficulties many times. Without her anything wouldn't be possible. I promise her that sooner or later we will have a proper holiday together. ...

Contents

List of Figures

List of Tables

Chapter 1

Introduction

1.1 Organization of the thesis

The work described in this thesis has been performed in the framework of the development of spectroscopic instrumentation for ultrafast pulses in the XUV domain and articulates in the following main activities:

- The installation and the characterization of two monochromatic High Harmonic beamlines for time-resolved experiments.
- The development and the characterization of a grating compressor for the conditioning of chirped ultrafast pulses.
- The use of a spectrometer employed in a Second Harmonic Generation in graphite experiment.

After a short introduction about the importance of ultrafast XUV pulses and the motivations that push the scientific community to develop ultrafast XUV technologies, this thesis is structured as follows:

In order to give an understanding of the experimental setups and results presented in this dissertation, Chapter 2 reports all the background theory related to each of the activities listed above. This chapter is structured in three parts: the first one contains the theoretical description of the High Harmonic Generation (HHG) process, the second deals with Chirped Pulse Amplification (CPA) in seeded Free Electron Lasers (FELs), while the third describes photon-in photon out experiments, with a special consideration for Second Harmonic Generation (SHG).

In chapter 3, a short introduction about High Harmonic beamlines for Time-Resolved Angular-Resolved PhotoEmission Spectroscopy using grating monochromators, is given. The main elements and issues that characterize a grating monochromator and the different geometries employed for the design of this kind of instruments are described. Successively, a detailed description of the design and the activities related to the installation and the characterization of two monochromatic High Harmonic beamlines for ultrafast time-resolved photoemission experiments, located respectively at Nanjing University and Elettra Sincrotrone Trieste, is provided.

In chapter 4, the development and the characterization of a XUV grating compressor installed at the FERMI seeded Free Electron Laser light-source at Elettra Sincrotrone Trieste and an overview of the experiments regarding the CPA technique performed at FERMI during the PhD period are presented.

In chapter 5, the description of a portable and compact spectrometer conceived for photon-in photon-out experiments and all the activities related to the optimization of the optical performance and the use of the instrument employed in a Second Harmonic Generation in graphite experiment performed at FERMI is reported. The analysis of the acquired data and the results of the experiment are presented.

Conclusions and an overview of future perspectives are reported in chapter 6.

Finally, in chapter 7 the list of the publications drawn up during the PhD period is reported.

1.2 Author's contribution

In the following, a brief description of the contribution I gave in each one of the three main activities discussed in this manuscript is given.

- Installation and characterization of two monochromatic High Harmonic Generation (HHG) beamlines for time-resolved experiments:

I have been involved in the installation, alignment and characterization of two different beamlines for the monochromatization of HHG radiation. The beamlines are located in Nanjing University, China (where I spent two months of my experience abroad) and in Elettra Sincrotrone Trieste, Italy. The activities cited above are described in detail in subsections 3.2.2 and 3.3.2. These sources are conceived for TR-ARPES (Time Resolved-Angle Resolved PhotoEmission Spectroscopy) experiments; In the case of the beamline located in Trieste, I also took part in the first experiments realized after the commissioning of the beamline and some of which are described in subsection 3.3.3.

- Development and characterization of a grating compressors for the conditioning of the spectral phase of chirped ultrafast pulses:

I have been involved in a project for the development and the characterization of an XUV grating compressor to be installed at the FERMI seeded Free Electron Laser light-source at Elettra Sincrotrone Trieste for Chirped Pulse Amplification (CPA) experiments. These activities are described in detail in sections 4.1 and 4.2. In addition to the contribution in the installation and in the alignment of the instrument, I took also part in all the experimental runs regarding the CPA technique performed in this period and described in detail in section 4.3.

- Use of a portable and compact photon spectrometer employed for a Second Harmonic Generation experiment:

The work has been related to the installation, the optimization of the optical performances and the operation of a compact spectrometer in view of measuring Second Harmonic Generation in graphite at Carbon K-edge. I took also part in the experimental runs at FERMI dedicated to the experiment and described in subsection 5.2.1. I worked on the analysis of the acquired data reported in subsection 5.2.2. In particular, I provided the intensity calibration of the instrument in order to calculate the intensity of the photon flux emitted by the sample in second harmonic. The calibration methods employed here are described in subsection 5.2.3.

1.3 Introduction to XUV ultrafast pulses

The comprehension of fundamental atomic and molecular processes has revolutionized many areas of science, leading to a better understanding of the most interesting mechanisms of physics. Many processes in atoms and molecules happen in the femtosecond (1 fs =10^{-15} s) and attosecond time scales (1 as = 10^{-18} s). Hence, the exploration of this kind of phenomena requires the use of ultra-short light pulses in the sub-femtosecond domain [1,2]. Ultra-short pulses enable us to record "movies" of these phenomena with extremely high temporal resolution. These movies are usually made through pump and probe techniques, where an ultrashort pulse (the pump) interacts with the sample and brings it out of the equilibrium. A second laser pulse (the probe) measures the real evolution in time of the process. Scanning the delay between the two pulses, the complete temporal evolution of the system can be measured. Of course, the obtainable resolution depends on the duration of the two pulses, therefore producing shorter laser pulses enables us to resolve faster processes. Research and experimental developments of ultra-fast technologies are therefore essential for providing novel tools for high-resolution time-domain spectroscopy. It should be taken into consideration that the temporal duration of a light pulse is limited by its optical cycle: therefore, Infra-Red (IR) and Visible light gives too long pulses to study processes in the femtosecond or attosecond time-scale. Thanks to the advances occurred over the last years, it is nowadays possible to produce eXtreme UtraViolet (XUV) and Soft X-ray pulses in the sub-femtosecond range, using different approaches [3]. The availability of these sources makes possible to apply time-resolved spectroscopic techniques in the XUV/ Soft X-rays domains. XUV and X-ray Free-Electron Lasers (FELs) are based on Self-Amplification of Spontaneous Emission (SASE) of relativistic electrons moving through the periodic magnetic field of an undulator. As the electrons go through the magnet structure, they undergo oscillations and begin to radiate coherently. This technique allows to generate femtosecond pulses with extremely high peak brilliance. The FEL emission, which is quite narrow, can be tuned in a broad range of energies by adjusting the electron-beam energy, the undulator period and the strength of the magnetic field [4,5]. Since the longitudinal coherence of a SASE FEL is not excellent (due to

the nature of the spontaneous emission process) in seeded FEL the temporal coherence of the machine is improved by using a seed pulse tuned to the FEL resonance. This temporally coherent signal can be produced by conventional high peak power laser. High Harmonic Generation (HHG) is an important tool for the generation of XUV radiation having extremely high coherence, ultra-short duration (down to the attosecond time scale) and high brilliance. Essentially, it is a process in which an ultrashort driving laser pulse at a given frequency is converted into integer multiples of this fundamental frequency due to the highly nonlinear interaction with a conversion medium. The high harmonic spectrum is composed of a sequence of peaks corresponding to the odd harmonics of the fundamental laser wavelength. The harmonic intensity decreases rapidly for low harmonic orders, while for higher orders a plateau of equally intense harmonics is found, which extends up the so called the cut-off wavelength [6]. Therefore, HHs bandwidth is very broad, since multiple orders of harmonics are generated coaxially. XUV and Soft X-ray harmonics cannot reach the intensities generated by FELs, but the shorter pulses make this technique a useful tool for the studies of novel ultra-fast phenomena [7]. Several systems have been conceived for the handling and the conditioning of the pulses generated by FELs and HH beamlines, in order to obtain a radiation with the desired characteristics. Ultrashort pulses can be monochromatized, reshaped or further compressed using specifically designed ultrafast instruments. For example, the spectral selection of a single harmonic of a HH spectrum in a narrow XUV band or the increase of the spectral purity of the FEL radiation can be accomplished using a grating monochromator, while the shortening of the duration and the increment of power of a FEL pulse can be performed using a grating compressor [8]. Moreover, the availability of efficient detectors for ultrashort pulses in the XUV/Soft X-ray domains, such as spectrometers, would help the deeper understanding of ultrafast phenomena. In this thesis the development, the characterization and the operation of ultrafast instrumentations applied for the handling, the conditioning and the detection of ultrashort pulses in the XUV and soft X-rays is discussed.

Chapter 2

Theory and background

2.1 High Harmonic Generation

High Harmonic Generation (HHG) is an important tool for the generation of ultrashort XUV (eXtreme Ultra Violet) pulses down to the atto-second time scale. HHG is a process in which an ultrashort intense driving laser pulse at a given frequency is converted into integer multiples of this fundamental frequency due to the highly nonlinear interaction with a conversion medium. When an ultrashort pulse is focused into an atomic or molecular targets, if the intensity is high enough it can distorts the atomic or molecular potential enabling a frequency up-conversion process to occur. The high harmonic spectrum is composed of a sequence of peaks corresponding to the odd harmonics of the fundamental laser wavelength. The harmonic intensity decreases rapidly for low harmonic orders, while for higher orders a plateau of equally intense harmonics is found, which extends up to the cut-off wavelength. The HHG process can be described by a three-step semi-classical model. According to the works of Corkum [9] and Kulander [10], the electron cannot be treated as a bound particle during the interaction with a high electric field. The electron is initially ionized (released from the binding force of the nucleus) by tunnel effect when the absolute electric field of the laser is close to its peak during an optical cycle and is carried away from the parent ion. The laser electric field changes the sign about a quarter of a period later, and the electron will slow down and start to accelerate back towards the ion. At this point, the electron can possess an amount of kinetic energy that is larger than the driving laser photon energy. This energy, added to the ionization potential, will be transferred into photon energy when the electron recombines with its parent atom. The cumulative emission of the individual atoms of the medium, gives the typical spectrum of the HHG mechanism. The described process is thus a three steps model: tunnel ionization of the atom, propagation of the electron in the laser field and recombination with the parent ion. In this section, the mechanism of High-Harmonic generation will be analyzed in more detail. The single particle response is examined in sub-section 2.1.1, while propagation effects, including phase-matching and absorption are described in section 2.1.2.

2.1.1 Single Particle Response

The High-Harmonic Generation process is described by a semi-classical approach composed by three steps: the ionization of the atom due the electric field of the driving laser, the propagation of the electron in the continuum and the recombination of the electron with the parent ion. In the following, each one of these fundamental mechanisms will be treated.

- Ionization:

If the intensity of the light interacting with the matter is increased constantly, the electric field of the electromagnetic wave associated to the laser radiation, $E(t) = E_0 cos(\omega_t)$, at some point becomes comparable to the interatomic field strength. The electron can thus escape the binding potential of the atom by tunneling. The electric field of the laser will produce a potential, $e\overrightarrow{E}(t)\overrightarrow{r}$, in addition to the Coulomb potential of the ion:

$$V(\overrightarrow{r}, t) = -\frac{e^2}{4\pi\epsilon_0 r} + e\overrightarrow{E}(t)\overrightarrow{r} \tag{2.1}$$

If the laser field strengths are big enough, the Coulomb potential can be significantly distorted. The barrier representing the bound electronic state can be overcame by tunneling, upon which the electron can be considered affected only by the electric field of the laser, as shown in Fig. 2.2 a). Since the atom can be actually ionized in other two different ways (multi-photon ionization and above-barrier ionization) the Keldysh parameter γ is introduced. It is defined as the ratio of the laser frequency to the tunneling frequency and determines for which range of laser field strengths E_0, angular frequency ω, together defining the ponderomotive potential U_p, in combination with a particular ionization potential of the medium I_p, the tunneling description is valid.

$$\gamma = \frac{\omega_{laser}}{\omega_{tunnel}} = \sqrt{\frac{I_p}{2U_p}}, \quad where \quad U_p = \frac{e^2 E_0^2}{4 m_e \omega^2} \tag{2.2}$$

where e is the electron charge and m_e is the electron mass.

In terms of the laser intensity and wavelength, the ponderomotive energy is given by

$$U_p[eV] = 0.97 \cdot 10^{-13} I[Wcm^{-2}]\lambda^2[\mu m^2] \tag{2.3}$$

Using this parameter it is possible to determine if the atom is ionized in the tunnel ($\gamma << 1$) or the multi-photon regime ($\gamma << 1$). The laser-distorted Coulomb potential is oscillating with the laser frequency. For higher and higher frequency (and thus larger and larger γ) the electron does not have enough time to follow to the fast changes in the potential. The electron motion will be then governed by an average over many cycles of the laser field rather than by the tunneling process in

a single cycle, since the tunneling time, depending on E_0 and I_p, is larger than the optical period. The nonlinear interaction with the laser field (absorption of many photons) will lead to an electronic state with an energy larger than zero, thus a free electron, as shown in Figure 2.1 b).

In the other case, the field of the laser can get high enough to suppress the barrier, as shown in Fig. 2.1 c). The electron is then classically 'ripped off' the atom. This ionization process is called the 'barrier-suppression ionization'. The tunnel-ionization is the best suited regime to high-harmonic generation.

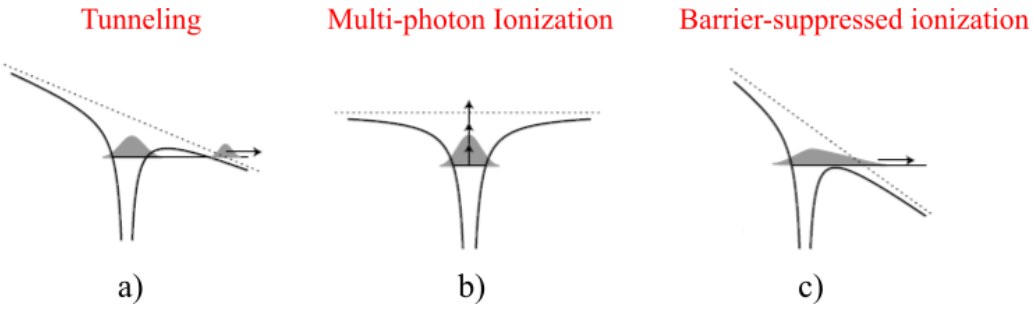

FIGURE 2.1: Different processes of ionization: a) the tunneling, b) the multi-photon ionization and c) the barrier-suppressed ionization.

- Propagation:

After the ionization, the electron passes from a condition in which it could occupy only a certain quantized energy states to one in which it can assume a continuum set of energies. In the continuum the classical mechanics can be used to describe the electron motion and to find its trajectories. Its motion can be thought as that of a charge in an oscillating electric field. If we suppose the electron is subjected only to the force produced by the incident laser electric field the velocity of the electron is:

$$v(t) = \int_0^t -\frac{e}{m}E(t')\,dt' + v_0 = -\frac{E_0 e}{m\omega}sin(\omega t) + v_0 \tag{2.4}$$

where the vector arrows are omitted in the case of one-dimensional motion of the electron. If we consider only electrons possessing a zero drift velocity, $v_0 = 0$, their average kinetic energy defines the ponderomotive potential mentioned above. If the electron, initially bound to an atom at $x = 0$, is ionized at the time zero with initial velocity $v_0 = 0$ and at an arbitrary phase φ of the electric field, the velocity $v(t)$ and position $x(t)$ can be calculated:

$$v(t) = -\frac{E_0 e}{m\omega}(sin(\omega t + \varphi) - sin(\varphi)) \tag{2.5}$$

$$x(t) = \int_0^t v(t')\,dt' = -\frac{E_0 e}{m\omega^2}(cos(\omega t + \varphi) - cos(\varphi)) + sin(\varphi)t \tag{2.6}$$

The time-independent term in the velocity can be interpreted as drift velocity. If it is zero, the electron is oscillating around a fixed reference position. If it is nonzero, the reference position is moving in time. The maximum kinetic energy of an electron can also be derived, and it is $8U_p$. The amplitude of the oscillatory position is referred to as the ponderomotive radius a_0. At laser intensities in the order of $10^{14}[Wcm^{-2}]$ typical values of a_0 are on the order of some nanometers (much larger than the atomic radius). These values denote the validity to consider the electron as a free particle in the laser field. It is worth to be noted that a_0 is limited to a quarter of the wavelength for electrons moving close to c. These relativistically moving electrons do not play a role in the high harmonic generation process. The laser intensities (at $\approx$ 800 nm) typically used for high-harmonic generation are below $10^{15}[Wcm^{-2}]$, while the laser intensities needed to accelerate electrons to relativistic intensities are beyond $10^{17}[Wcm^{-2}]$. The electron trajectories versus time in a linearly polarized laser electric field are shown in Fig. 2.2. It is possible to observe the different paths for electrons that become ionized at different phases of the laser field. Only few electron trajectories return to the origin, where the electron can recombine with the parent ion. The absolute value of the slope of the trajectories at the zero crossings is the velocity of the electron and thus a measure for their kinetic energy. Its highest value is obtained at an ionizing phase close to 20 degrees. In addition, only the first two zero crossings lead to significant photon emission. This can be explained with the quantum-mechanical nature of the electron, which suffers from spreading of the wave-function as soon as it is not bound to a potential.

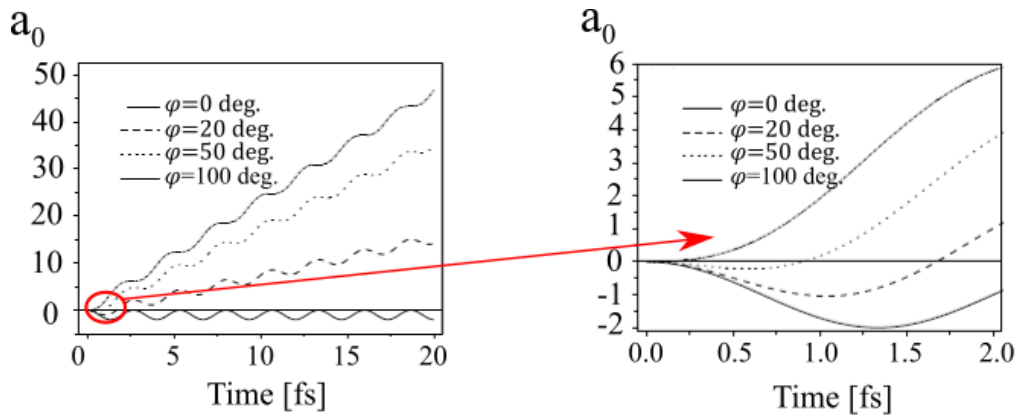

FIGURE 2.2: Electron trajectories in a linearly polarized laser electric field (a_0 versus time for a unidirectional motion).

- Recombination:

The electron oscillating with the electric field has a finite probability to collide with the parent ion in a specific time. As also mentioned, the more it rests in the continuum, the more its wave function broads and the more the superposition with the wave function of the bound state decreases and thus lower is the probability to collide with the ion. When an electron recombines with the parent ion, typically a

photon is emitted carrying away the excess energy of the electron. In particular, the accelerated electrons emit a high harmonic photon with energy $\hbar\omega = E_{kin} + I_p$. As seen above, the slope of the trajectories at the zero crossing assumes different values, corresponding to different velocities and thus different kinetic energies. The maximum kinetic energy that the electron can have when it recombine with its parent ion corresponds to the maximum photon energy which can be generated in the process. The maximum kinetic energy is $\approx 3.17U_p$, occurring at a phase of ≈ 18 degrees. All the electrons ionized at this time produce harmonic photons with the highest energy. The high-harmonic soft x-ray spectrum vanishes at photon energies higher than $\hbar\omega_c = 3.17U_p + I_p$. This relation is the cut-off law for the high harmonic generation process. This law is the confirmation that the tunneling regime supports the generation of high harmonic radiation. The highest photon energies are produced when the electric field is close to its peak in the optical wave. In the tunneling regime, the ionization rate increases with the electric field. Therefore, many ionized electrons will contribute to high-harmonic generation. Considering the cut-off law, it is evident that in order to generate higher harmonic orders a larger pondero-motive potential is needed. This is fulfilled in the tunneling regime, where the Keldysh parameter γ has to be much smaller than unity. The dependence of the high-harmonic process on the phase of the driving field also evidence that the harmonic radiation is intrinsically coherent to the fundamental field. The harmonic peaks of a high order harmonic spectrum exist at odd integer multiples of the fundamental frequency f of the driving laser. This happens because the three-step process repeats every half-cycle of the laser field. The Fourier transform will be thus discrete, with a separation corresponding to $2f$, which is what it is observable in the spectrum. If the conversion medium has broken inversion symmetry, harmonic emission will not occur at every half-cycle but at every cycle of the laser field. This happens also if the plasma is driven at very high intensities, where the magnetic field of the laser becomes high enough to break the inversion symmetry. In this case the laser intensities are on the order of $10^{18}[Wcm^{-2}]$ and the electron motion is not harmonic anymore as described by the classical propagation equations. In Fig. 2.3 the three-step model is finally summarized.

Finally, a typical high-harmonic spectrum generated in neon is shown in Fig. 2.4. As mentioned, for low orders the harmonic intensity is rapidly decreasing. A plateau is visible for higher orders, which is terminated at the cut-off, the highest harmonics that can be generated. The spectral position of the plateau depends on both the gas used and the intensity of the driving light.

2.1.2 Propagation effects

The phase matching issues of the high harmonic generation process is here discussed. The equation for the wave-vector mismatch for the generation of the mth harmonic can be written as:

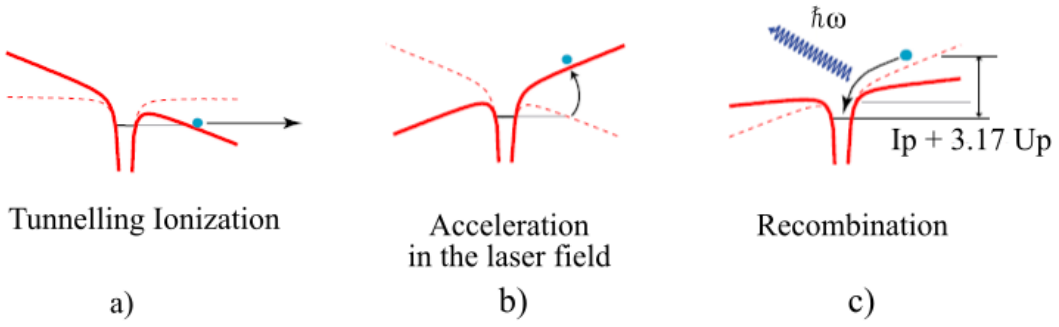

FIGURE 2.3: The three steps model. a) The ionization of the atom, b) the acceleration of the electron in the laser field , c) the recombination of the electron with the parent ion.

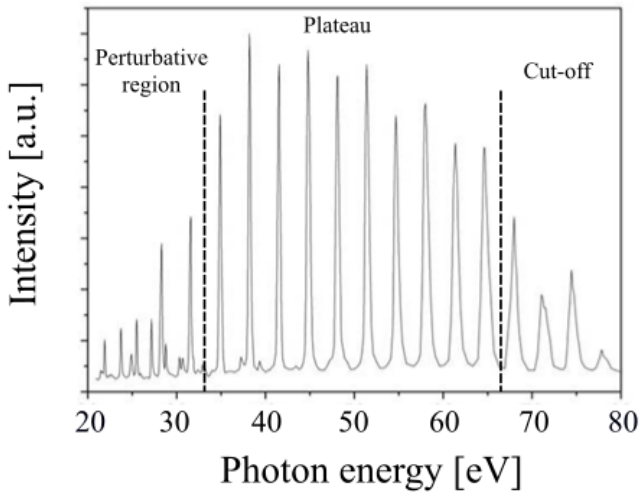

FIGURE 2.4: A typical high-harmonic spectrum generated in Neon.

$$\Delta k = mk(\omega_f) - k(m\omega_f) \tag{2.7}$$

where ω_f is the fundamental laser angular frequency. Since the collinear harmonic generation geometry is considered, the formula can be written in the scalar form. The medium used for the generation process is generally a gas which exhibits dispersion and its refractive index depends on ω. The dispersion modifies the wave-vector by the amount Δk_{disp}. Moreover, the high intensities employed to drive the high order harmonic generation leads to the generation of free electrons, the majority of them do not recombine with their parent ion. The generated plasma gives origin to a resonance that modifies the refractive index and creates the contribution Δk_{plasma}. In addition, the focusing and propagation of the driving laser brings to a geometrical modification Δk_{geom} of the wave-vector. Then, the wave-vector can be written as:

$$k(\omega) = k_{vac}(\omega) + k_{disp}(\omega) + k_{plasma}(\omega) + k_{geom}(\omega) \tag{2.8}$$

where $k_{vac}(\omega) = \frac{2\pi\omega}{c}$ is the wave-vector in free space. The wave-vector mismatch can be thus written as:

$$\Delta k = \Delta k_{disp} + \Delta k_{plasma} + \Delta k_{geom} \tag{2.9}$$

The phase matching is always achieved in vacuum, since the contribution Δk_{vac} vanishes because:

$$\Delta k_{vac} = m\frac{\omega_f}{c} - \frac{m\omega_f}{c} \tag{2.10}$$

The conversion media used for high generation exhibits all dispersion, which is the dependence of the refractive index $n(\omega)$ to the frequency of the radiation. The wave-vector mismatch due to dispersion can be written as:

$$\Delta k_{disp}(\omega) = mk_{disp}(\omega_f) - k_{disp}(m\omega_f) = (n(\omega_f) - n(m\omega_f))\frac{m\omega_f}{c} \tag{2.11}$$

In general, the refractive index is larger than 1 in the near-infrared (wavelengths range of the fundamental laser light) and smaller than 1 in the XUV, where the harmonics are located. Therefore $\Delta k_{disp} > 0$. In the High order Harmonic generation process only few electrons recombine with the parent ion to emit a harmonic photon. The remaining electrons become free for a long time compared with the duration of the laser pulse (several ns). The plasma contribution to the wave-vector mismatch is:

$$\Delta k_{plasma} = mk_{plasma}(\omega_f) - k_{plasma}(m\omega_f) = \frac{\omega_p^2(1-m^2)}{2mc\omega_f} \tag{2.12}$$

where ω_p is the plasma resonance frequency. Therefore $\Delta k_{plasma} < 0$. Since we need to generate high intensities, also the geometry contribution has to be taken into account. Basically two geometries can be employed for high harmonic generation: focusing onto a gas jet or cell in a free space geometry or propagating the gas in a hollow capillary as a waveguide. The focusing on a free space geometry contribution will be analyzed, since this kind of approach is the most widely used in high harmonic generation beamlines. In Fig. 2.5 the free space focusing geometry sketch is reported. The focusing on a free space geometry contribution to the wave-vector mismatch is

$$\Delta k_{foc} = mk_{foc}(\omega_f) - k_{foc}(m\omega_f) = 2\frac{m-1}{b} \tag{2.13}$$

where $b = 2z_r$ is the confocal parameter, with z_r the Rayleigh length of the beam. Therefore $\Delta k_{foc} > 0$.

In order to generate high-harmonic radiation at the maximum efficiency, we have to ensure phase-matching conditions, taking into account all the contributions to the

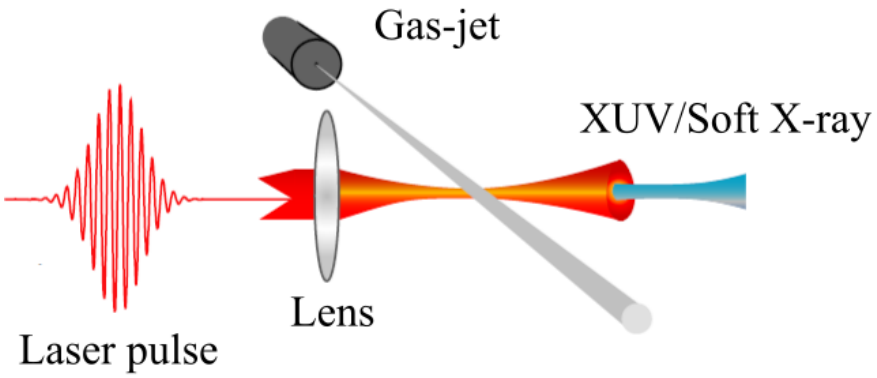

FIGURE 2.5: The sketch of the free space focusing geometry.

phase mismatch. At this point, the total phase mismatch for the focusing geometry can be rewritten as:

$$\Delta k = \Delta k_{disp} + \Delta k_{plasma} + \Delta k_{foc} \tag{2.14}$$

Since it necessary to achieve $\Delta k = 0$ for a most efficient conversion of the driving laser radiation into m^th harmonic radiation, the contribution of neutral dispersion and the focusing geometry have to be counter-balanced by the plasma dispersion. The Δk_{foc} term in general depends on z, the distance from the focus on the optical axis. Moreover, the intensity also changes along the propagation direction as the beam is focused. The atomic dipole phase depends on intensity for one particular trajectory of the electron affect the wave-vector of the harmonic radiation [11,12]. This brings to different spatial distributions of the harmonic intensity in the generated beam depending on whether the gas jet is placed before or behind the focus[12, 13]. Beam shaping techniques can be used in order to optimize the harmonic production process in the free focusing geometry [14]. The density of the gas can also be varied in order to improve the phase matching. This can be done increasing the pressure in the gas cell. Moreover, the plasma density depends on the ionization potential of a given gas and it can be controlled by means of the intensity or the duration of the laser pulse. Note that the change in intensity will cause a change in the maximum harmonic order (cut-off law) that can be generated. As can be seen from equation (2.12), Δk_{plasma} becomes higher increasing the harmonic order m. Therefore, keeping the plasma density at low values is fundamental. On the other hand, it is necessary to apply high intensities to generate very high harmonic orders. The solution to overcome this contradiction is using very short driving laser pulses [15,16]. Using shorter pulses higher peak intensities of the harmonics can be obtained (compared with a longer pulse) for the same amount of plasma being created. When a long pulse ionize completely the medium by the time it reaches its peak intensity, the available high intensities cannot be used for harmonic generation since the HHG process is based on the availability of non-ionized electrons. A shorter pulse

reaches the same peak intensities in a shorter time, in which the medium does not have enough time to become completely ionized (assuming the ionization rate depending mainly on the instantaneous electric field or intensity). A limitation for the phase-matching is the re-absorption of the generated harmonic radiation within the conversion medium; the high-harmonic spectrum is generated in the XUV/Soft x-ray spectral region, where light is strongly absorbed by matter. The absorption length of a conversion medium (which is the distance after which the intensity of the propagating radiation drops to $1/e$) is $L_a = \sigma\rho$, where σ is the particle density. The driving laser propagates through the conversion medium and generates new harmonic light that is added to the co-propagating harmonic radiation generated earlier, which is affected by absorption. Summing over all contributions to the m^th harmonic radiation at the point where the harmonic pulse leaves the conversion medium the following relation is obtained:

$$I_m \propto \left| \int_0^L \rho A_m(z) e^{-\frac{L-z}{2L_a}} e^{i\varphi_m(z)}\, dz \right|^2 \tag{2.15}$$

where $A_m(z)$ is the harmonic amplitude of the single-particle response and phase $\varphi_m(z)$, at the exit of the conversion medium of length L. If $A_m(z)$ is not depending on the position z along the optical axis as it is approximately the case of a loose focusing geometry, where the laser intensity stays roughly constant along the interaction region, the equation above becomes:

$$I_m \propto \rho^2 A_m^2 \frac{4L_a^2}{1+4\pi^2(L_a^2/L_c^2)}(1+e^{-\frac{L}{L_a}} - 2cos(\frac{\pi L}{L_c})e^{-\frac{L}{2L_a}}) \tag{2.16}$$

where $L_c = \frac{\pi}{\Delta k}$ is the coherence length that can be calculated from the total wavevector mismatch. It is worth to be noted that the equation converges to a finite value for the case of $L \longrightarrow \infty$. In order to generate close to the maximum amount of harmonic radiation that is possible, given the absorption of the gas, the conditions $L > 3L_a$ and $L_c > 5L_a$ must be fulfilled [17,18].

2.2 Chirped Pulse Amplification (CPA) in seeded Free Electron Lasers

Chirped pulse amplification (CPA) in optical lasers is a well known technique which allows the generation of femtosecond pulses in the infrared and visible spectral ranges with extremely high power [19]. Thanks to the advances occurred in the recent years, it is nowadays possible to produce eXtreme UtraViolet (XUV) and Soft X-ray pulses in the sub-femtosecond range to be used for experiments in a large variety of disciplines. Free Electron Lasers allows generating femtosecond pulses radiation with extremely high peak brilliance in the XUV/Soft X-ray domain. Unfortunately, for any given FEL setup, a temporal limit exists in the generation of ultra-short pulses carrying substantial energy. Several methods have been proposed

to shorten the ultra-short duration of FEL pulses such as time slicing and reduction of the electron bunch charge [20-23]. In these methods, the output pulse energy is strongly limited by the lower number of electrons participating in the amplification process. Recently, other innovative theoretical schemes have been proposed, in order to increase the peak power of the FEL radiation up to the terawatt [24]. However, in these cases, the pulse shortening is limited by the FEL gain bandwidth. Moreover, none of these methods allows the control of the spectral and temporal properties of the generated light, which is a fundamental requisite for the generation of extremely high-coherence optical pulses [25]. A different approach is the optical compression of the pulse generated by the whole electron beam, applying the CPA technique to seeded FEL pulses [26, 27]. CPA, in fact, can be also applied to seeded FELs if the seeding pulse is stretched in time before the interaction with the electron beam. In this way the whole electron beam charge is employed, obtaining a significantly higher number of photons with ultra-short duration. In this section, the mechanism of the CPA on seeded FELs will be analyzed in detail. The basic description of the FEL process, with a comparison between SASE FELs and Seeded FELs is examined in sub-section 2.2.1. The theoretical description of the CPA technique on seeded FELs is described in section 2.2.2.

2.2.1 Free Electron Lasers

Free Electron Lasers (FELs) are coherent light sources which produce ultra-short, tunable and extremely high brilliant radiation from the infra-red (IR) to the X-ray domain. In a FEL the electrons are accelerated at relativistic kinetic energies and travel through the periodic magnetic field of an undulator in which the radiation is emitted. The interaction with the electromagnetic radiation field leads to an exponential growth of the radiation emitted by the electrons. Self Amplified Spontaneous Emission (SASE) FELs are based on the amplification of the spontaneous emission emitted in the undulator, whereas Seeded FELs use an external radiation (i.e. a seed laser) to initiate the radiative process. Since the electrons in the FEL are not bound to atoms and thus not limited to specific transitions, the FEL is tunable over a wide range of wavelengths, depending on the accelerator energy and undulator parameters. For IR and visible FELs, the amplification can be obtained using an optical cavity with mirrors on both sides and the electrons passing the undulator as the gain medium in between. In this way the light from many successive electron bunches can be stored and amplified. For XUV and X-ray FELs, mirrors cannot be applied due to their low reflectivities in normal incidence in this domain and potential mirror damage due to the high absorbed power. Since a SASE FEL operates in the high-gain regime, it does not require any optical cavity. FELs in the visible and UV range can be realized in synchrotron radiation storage rings, while, due to the higher demands on the electron beam properties, a linear accelerator is needed to generate FEL radiation in the XUV and X-ray range. The most promising approach

is the setup of a single pass SASE FEL at a state of the art linear accelerator in combination with a high-performance radio frequency photo-cathode electron gun and longitudinal bunch compression. While travelling with relativistic velocity through the undulator, the FEL electrons are accelerated in the direction transverse to their propagation due to the Lorentz force introduced by the magnetic field. They propagate along a sinusoidal path and emit radiation in a narrow cone in the forward direction. The opening angle of the wavelength integrated radiation is:

$$\frac{1}{\gamma} = \frac{m_e c^2}{E_e} \tag{2.17}$$

where m_e is the electron mass $511 KeV/c^2$ and E_e the electron energy. The radiation generated by the electrons while travelling along the individual magnetic periods overlaps and the formula for the wavelength $\lambda_p h$ of the first harmonic of the spontaneous, on-axis undulator emission becomes:

$$\lambda_p h = \frac{\lambda_u}{2\gamma^2}(1 + K_{rms}^2), \qquad K_{rms} = \frac{eB_u\lambda_u}{2\pi m_e c} \tag{2.18}$$

where λ_u is the length of the magnetic period of the undulator and K_{rms} is the averaged undulator parameter that provides the ratio between the average deflection angle and the typical opening cone of the synchrotron radiation. B_u is the rms magnetic field of the undulator and e is the electron charge. To obtain an exponential amplification of the spontaneous emission in the undulator, a good electron beam quality and a sufficient overlap between radiation pulse and electron bunch along the structure must be achieved. This means that low emittance, low energy spread of the electron beam with an extremely high charge density together with a precise magnetic field and accurate beam steering through the undulator must be provided. During the oscillation through the undulator, the electron bunch interacts with its own radiation created via spontaneous emission. Depending on the phase between the electromagnetic field and electron oscillation, electrons can be decelerated or accelerated: when they are in phase with the electromagnetic field they are retarded, whereas when they own opposite phase they gain energy. In this way a longitudinal structure (called micro-bunching) which amplifies the electromagnetic field, is established. In Fig. 2.6 the scheme of the SASE process in a FEL undulator is shown. The longitudinal density modulation of the electrons with the resulting exponential growth of the radiation power are shown in the lower part of the picture.

The electrons in the longitudinal direction within the bunch are "sliced" with a separation corresponding to the wavelength where λ_{ph}, which is the wavelength of the emitted radiation which causes the modulation. The electrons begin to radiate in phase increasingly with a subsequent growing coherent superposition of the radiation emitted from the micro-bunched electrons. The more intense the power of the radiation become, the more intense the longitudinal density modulation of the electron bunch is and vice versa. Initially, all the electrons in the bunch $N_e \geq 10^9$ can be

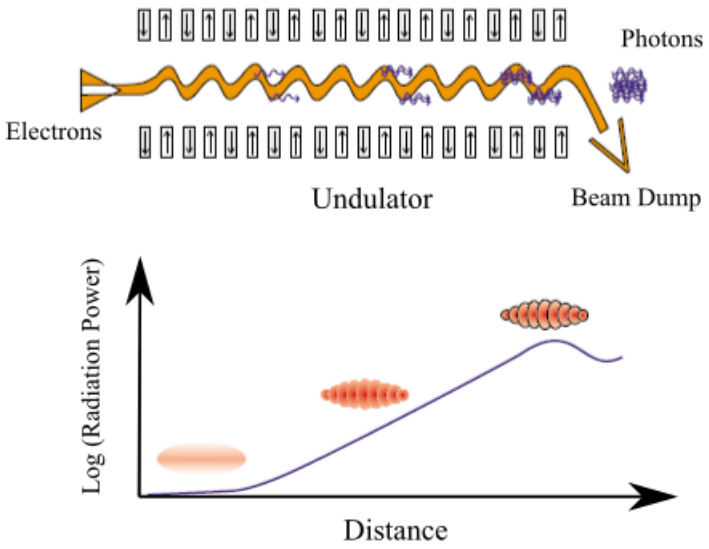

FIGURE 2.6: Scheme of the self-amplification of spontaneous emission (SASE) in an undulator.

treated as charges that radiates singularly with the power of the spontaneous emission, which is linearly proportional to the number of electrons in the bunch $P \propto N_e$. When the bunching is achieved, all the electrons radiate almost in phase. This leads to a radiation power quadratically proportional to the number of electrons in the bunch $P \propto N_e^2$. The progressing micro-bunching leads to an exponential growth of the radiation power $P(z)$ with the distance z along the undulator [28- 30]:

$$P(z) = AP_{in}e^{\frac{2z}{L_g}} \tag{2.19}$$

where L_g is the field gain length, P_in is the input power and A the input coupling factor, which is equal to $1/9$ in one-dimensional FEL theory with an ideal electron beam. For the estimation of the input power one can use the spontaneous radiation power on the first gain length inside a coherence angle and within the FEL bandwidth. It is worth to be noted that the exponential growth takes place until the electron beam is completely bunched, after which saturation effects take place. The main properties of the FEL radiation can be derived from the FEL parameter ρ [31]: the field gain length is $L_g = \frac{\lambda_u}{4\pi\rho}$, the FEL amplifier bandwidth $\frac{\Delta_\omega}{\omega}$ and saturation efficiency (ratio of the output radiation power to the electron beam power) are about ρ. This factor depends on the parameters of the electron beam and of the undulator of the FEL and is always much smaller than unity. The radiation from an XUV-Soft X-ray FEL has a narrow bandwidth, is fully polarized and transversely coherent. The transverse coherence is also reflected in the development of the transverse intensity distribution along the undulator, as shown in Fig. 2.7. On the other hand, the longitudinal coherence of a SASE FEL is not excellent, due to the nature of the spontaneous emission process. Examples of the spectral and temporal structure of the radiation pulse from a SASE Soft X-ray FEL are presented in Fig. 2.8.

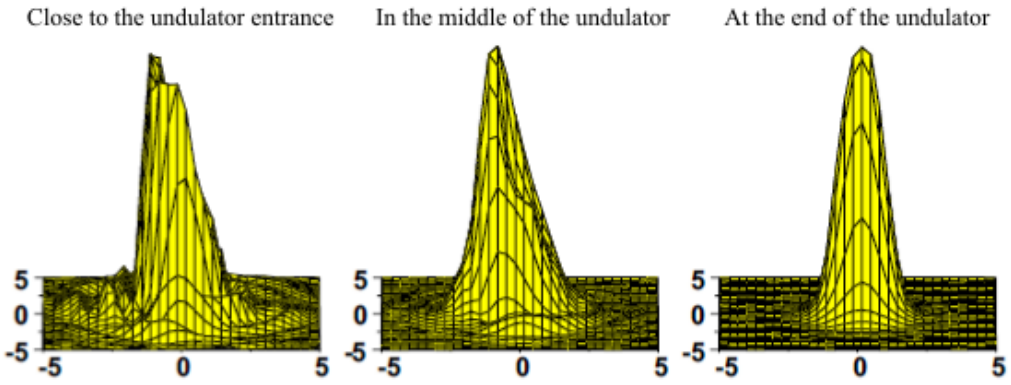

FIGURE 2.7: Distribution of the radiation intensity across one slice of the pulse along the undulator. The figure shows the intensity vs. the transverse coordinates.

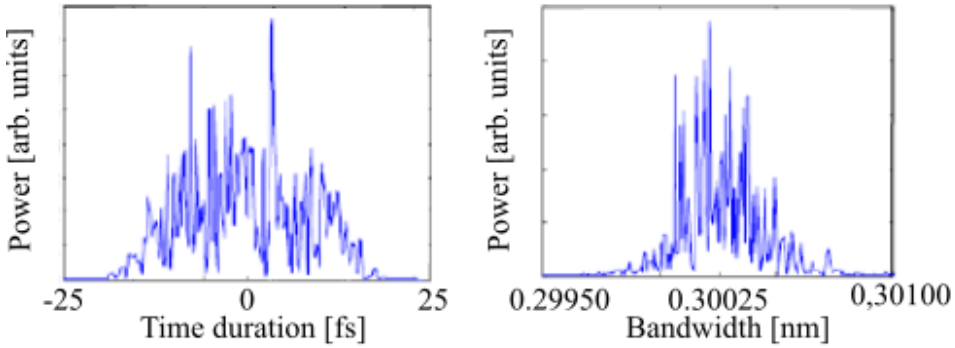

FIGURE 2.8: Spectral and temporal structure of the radiation pulse from a SASE Soft-X-ray FEL.

The spectral and temporal profiles of the output radiation are a consequence of the SASE process: considering that the electron bunch consists of discrete charges randomly emitted from a cathode, the charge density presents random fluctuations in time and space. The SASE radiation has random amplitudes and phases in time and space. It is also worth mentioning that using a planar undulator, a SASE FEL also generates higher harmonics, since the micro-bunching of the electrons at the fundamental wavelength of the undulator can also push a bunching at the higher harmonics of this fundamental wavelength. To improve the temporal coherence of the machine, a seed pulse tuned to the resonance of the FEL can be employed in order to initiate the amplification process. This temporally coherent signal can be produced by high-harmonic generation (HHG) or by conventional high peak power laser. The purposes of seeded FELs are, besides to overcome the limitation of longitudinal coherence of the SASE FELs (thus improving the brilliance of the output signal), synchronizing the FEL with an external signal and improving the stability of the FEL power from shot-to-shot [32]. In Fig. 2.9 examples of the spectral and temporal structure of the radiation pulse from a Seeded XUV-Soft X-ray FEL are shown.

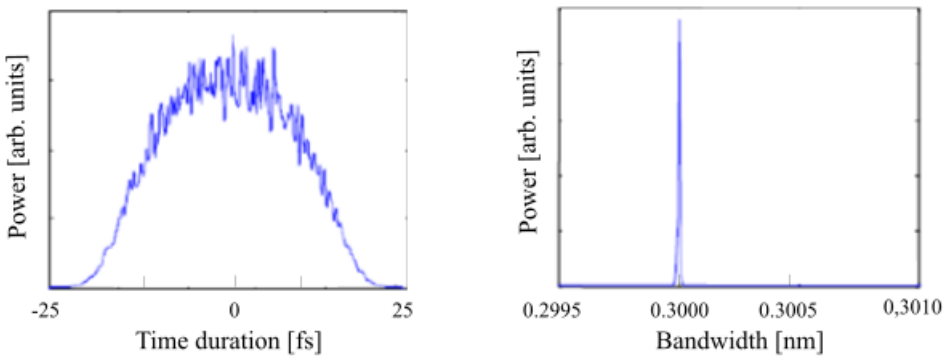

FIGURE 2.9: Spectral and temporal structure of the radiation pulse from a Seeded Soft-X-ray FEL.

As already mentioned, the characteristics of the FEL radiation are high power, short pulse length, narrow bandwidth, spatial coherence and wavelength tunability. The FERMI FEL light-source at Elettra Sincrotrone Trieste is one of the major FEL projects in Europe. It is a unique international user facility for scientific investigations employing ultra high brilliance X-ray pulses based on an external seeding scheme. In Figure 2.10 some typical photon beam parameters of the FERMI @ ELETTRA seeded Free Electron Laser are reported.

Parameters	Units	FEL-1	FEL-2
Wavelength range	nm	20 – 100	4 – 20
Photon energy	eV	62 – 12	62 – 310
Energy per pulse	mJ	50 – 300	10 – 100
Relative bandwidth (FWHM)	%	0.1	0.1
Pulse length	fs	50 – 100	30 – 70
Power fluctuations (rms)	%	10	30
Polarization		Hor/Vert/Circ	Hor/Vert/Circ

FIGURE 2.10: Photon beam parameters of the FERMI @ ELETTRA Free Electron Laser.

2.2.2 The CPA technique

In a solid-state laser, the frequency chirping is employed to stretch a short duration pulse before the amplification process, in order to reduce the phase distortion in the medium. After the pulse amplification, the chirp is compensated in order to recover the short duration and the high power of the pulse. Similarly, CPA in FELs consists on stretching the seed pulse in time before the interaction with the electron beam. In this way the bunching is induced on a larger number of electrons, and the output energy of the generated FEL pulse is linearly increased. In ideal conditions, the frequency chirp carried by the phase of the seed is transmitted to the phase of

the FEL pulse. The compensation of the chirp of the FEL pulse enable the recovery of the duration of the short pulse (ideally limited by the Fourier limit) and a larger peak power with respect to what obtained, for the same operating conditions, in the no chirped seed operation mode. Another advantage of the CPA technique is the possibility of significantly shortening the duration of the FEL pulse, with respect to what obtained in "standard" operation mode. Moreover, as demonstrated below, the bandwidth of a seeded FEL operated in CPA mode increases with the harmonic number n. This effect can be obtained by properly chirping in energy the electron beam in order to match the FEL resonant condition. This allows to bypass the limit due to the finite FEL gain bandwidth, removing the limit on the shortest FEL pulse duration reachable with an optical compressor [27, 33]. Consider a Gaussian chirped laser pulse having an electric field in the frequency domain:

$$E(\omega) \sim e^{-\frac{\omega^2}{2\sigma_\omega^2}} e^{-\frac{i\beta\omega^2}{4}} \tag{2.20}$$

where σ_ω is the rms laser bandwidth and β is the Group Delay Dispersion (GDD), used to quantify the frequency dispersion. The Fourier transform of E_ω is:

$$E(t) \sim e^{-\frac{t^2}{2\sigma_t^2}} e^{i\Gamma t^2} \tag{2.21}$$

where the coefficient of the quadratic temporal phase, Γ, and the (rms) laser pulse duration σ_t, are related to β and σ_ω through the following relations:

$$\Gamma = \frac{\beta}{4/\sigma_\omega^4 + \beta^2} \tag{2.22}$$

$$\sigma_t^2 = 1/\sigma_\omega^2 + 1/4\beta^2\sigma_\omega^2 \tag{2.23}$$

Based on the previous equations, two regimes can be distinguished: For $\beta << 2/\sigma_\omega^2$ and thus for $\sigma_t \simeq 1/\sigma_\omega$; for $\beta >> 2/\sigma_\omega^2$ and thus $\sigma_t \simeq 1/2\beta\sigma_\omega$. The second one is the suitable regime for the CPA technique. If the FEL is seeded by a gaussian seed laser pulse, the FEL is expected to have an almost gaussian pulse profile. According to the literature [34], the duration of the FEL pulse in the standard operating mode is:

$$(\sigma_t)_{FEL}^{NoCPA} = n^{-\alpha}(\sigma_t)_{tseed} \tag{2.24}$$

where n is the harmonic order of the FEL radiation, $(\sigma_t)_{tseed}$ is the duration of the seed pulse and α (positive and smaller than 1/2) is a factor that depends on the regime in which the FEL is operated. As a consequence of this frequency up-conversion, the phase of the FEL pulse is n times that of the seed. On this basis, it can be easily shown that if the seed is characterized by a strong chirp (and the longitudinal electron-beam energy profile can be assumed to be almost flat), the same is for the FEL pulse [35]. In this case, the amount of GDD to be compensated by the optical compressor is related to β_{seed} by the following relation:

$$\beta_{FEL} \simeq \beta_{seed}/n \tag{2.25}$$

Combining the previous equations the FWHM FEL pulse bandwidth $(\Delta\omega)_{FEL}$ scales according to the relation:

$$(\Delta\omega)_{FEL} = n^{1-\alpha}(\Delta\omega)_{seed} \tag{2.26}$$

In the following, it is assumed to work with a FEL in moderately saturated regime, corresponding to $\alpha \simeq 1/3$ [34]. It is worth to be noted that in seeded FELs the broadening of the FEL pulse bandwidth respect to that of the seed pulse originates from two competing phenomena: the frequency up-conversion process increases the FEL pulse bandwidth by a factor n relative to the bandwidth of the seed, while the dynamic reduction of the FEL pulse duration due to the nonlinear laser-electron interaction within the modulator, represented by the factor α, counterbalance the effect. The shortest FEL pulse duration, $(\Delta_t)_{FEL}^{min}$ obtainable after compressing the FEL pulse can be thus derived from the equation above and it is:

$$(\Delta_t)_{FEL}^{min} = \frac{(\Delta_t)_{seed}^{TL}}{n^{1-\alpha}} \tag{2.27}$$

where $(\Delta_t)_{seed}^{TL}$ is the seed pulse duration at the transform limit (i.e. in the absence of chirp).

2.3 Photon-in photon out experiments and SHG

Photon-in photon-out XUV/Soft-X-ray spectroscopy techniques are long-standing approaches applied for material analysis at 3rd generation synchrotron radiation sources [36- 39]. Moreover, the development of 4th generation XUV/Soft-X-ray free-electron-laser (FEL) sources have opened new perspectives in the study of the structure and dynamics of materials at atomic level and ultra-fast timescale using this kind of techniques [40- 44]. As also outlined in the previous sections FELs are capable of delivering XUV/ Soft X-ray pulses with high brightness, ultrashort pulse duration, and extremely high coherence. The availability of an extremely high number of photons in a single pulse in the fs time scale allows to study ultrafast single and multi-photon excitation and, by using a pump and probe scheme, excitation dynamics involving core levels. It is worth to be noted that the high photon per pulse obtainable with FEL sources, brought also to a considerable improvement in the realization of instrumentation for the detection of high-quality spectra with a single shot or with a limited number of pulses. This opened the way to unprecedented applications of photon-in photon-out techniques under extreme conditions or to isolated molecules and clusters in the soft and X-ray regimes. In this section, Photon-in photon out experiments, with a special consideration for the Second Harmonic Generation (SHG) process, are described. In subsection 2.3.1 a brief overview of the main

elements of photon-in photon-out spectroscopy is first of all given, together with an outline regarding the instrumentation for analyzing Soft X-ray emission spectra. In subsection 2.3.2 a detailed description of the SHG process is given.

2.3.1 Introduction and instrumentation

X-ray emission spectroscopy (XES) is a standard technique for probing the occupied density of electronic states of a material. In this process a core electron is excited by an incident X-ray photon and this excited state decays by emitting an X-ray photon to fill the core. The energy of the emitted photon is equal to the energy difference between the involved electronic levels. The analysis of the energy dependence of these emitted photons provides information about the electronic structure of a given material. XES is element-specific and site-specific, and can occur in two ways: non-resonant x-ray emission spectroscopy (NXES) and resonant inelastic x-ray emission spectroscopy (RIXS). NXES probes the occupied density of electronic states of a material. In this case, when an electron is excited to an unoccupied state, a core hole is created. This core hole can be filled by the previously excited electron or by an electron from higher occupied states. RIXS technique is based in the inelastic scattering of photons that are of a specific energy that corresponds to a resonance peak in the absorption spectrum of the material. In this process the energy and momentum change of the scattered photon are measured by analyzing the excitations in the material caused by the transfer of energy. Whereas, X-ray absorption spectroscopy (XAS) is complementary to XES and is a fundamental tool for probing the unoccupied density of electronic states of a material. The measurement analyze the fraction of photons that are absorbed by the sample. Photons are absorbed by atomic core energy level electrons, which are then promoted to higher previously unoccupied energy levels. Again, the decay of electrons from these unstable states originates the emission of photons having an energy equivalent to the energy difference between the core level and excited state. XAS is also a powerful technique for measuring density of states because it is, as it is XES, element and site specific. In Fig. 2.12 the schematic energy level diagram of the XES and XAS processes is reported.

The development of 4th generation XUV/Soft X-ray FEL sources have opened the way to unprecedented applications of photon-in photon out spectroscopies. A wide range of experiments on organic molecules [45] metal-organic complexes [46] and clusters [47] have taken advantages from the improvements in the FEL radiation sources, given the extremely low number of target particles available in these experiments. An additional degree of freedom can also be obtained with pump-probe schemes using FELs. The probing of core electrons will allow a direct investigation of photo-physical and photo-chemical processes with the elemental sensitivity of core electron spectroscopies. However, various combinations of photon-in photon-out techniques have been used for chemical and structural investigations of condensed matter [48]. The availability of efficient detectors for this kind of experiments would help a deeper understanding of ultrafast transitions occurring in solid

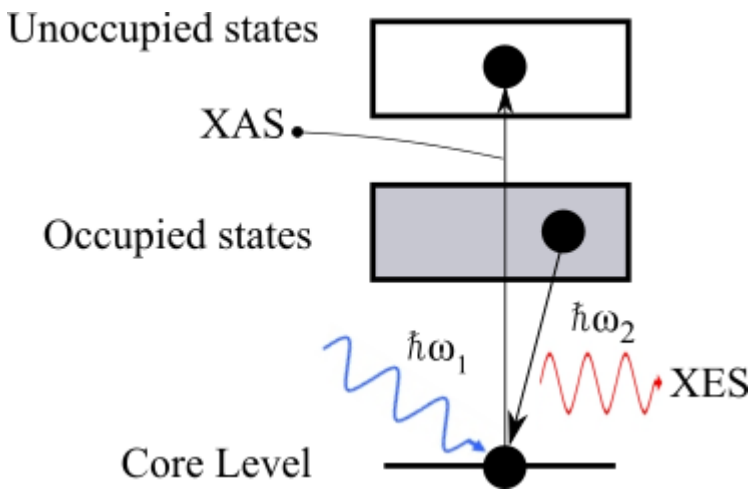

FIGURE 2.11: Schematic energy level diagram of the XES and XAS processes.

targets (surfaces and thin films) in the femtosecond time scale. The extremely high photon per pulse obtainable with FEL sources brought to a considerable improvement in the realization of instrumentation for the detection of high-quality spectra with a single shot or with a limited number of pulses. Several instruments for analyzing emission spectra in the XUV and soft X-ray region are available currently. The main specifications of these devices are the detection efficiency (throughput) and the resolving power. Grating spectrometers are one of the most used tools for the analysis of X-ray emission spectra. In this kind of instruments the X-rays radiation from a sample usually enters a source-defining slit and is then dispersed (e.g. each wavelength is sent into a different direction) by a diffraction grating. A detector, placed at the focal point of the instrument, finally acquire the diffracted radiation. If the repetition rate is not too high, single shot spectra within a certain wavelength range can be recorded simultaneously by using a two-dimensional detector such as a micro-channel plate or an X-ray sensitive CCD chip. Grating spectrometers can be divided into two main categories: plane gratings spectrometer and Variable Line Spacing (VLS) grating spectrometers. A plane grating spectrometer usually needs optical element that makes the divergent rays emitted by the source into a parallel beam. This is typically achieved by using a toroidal mirror. The parallel rays coming from this mirror are sent to a plane grating (having a constant groove density) and are diffracted depending to their wavelength. A second toroidal mirror, placed after the grating, collects the diffracted rays at a certain angle and creates an image on a detector. A VLS spectrometer consists, instead, in using a spherical or toroidal grating with variable line spacing along the surfaces, to provide a flat spectral focal plane that is almost perpendicular to the direction of the diffracted light [49]. In this case no other additional mirrors are required either to collimate the beam before the grating and to focus it in to the detector [50]. The optimal design of these instruments should ensure minimal optical aberrations (and thus maximal resolution) at

maximal angular acceptance (and thus maximal spectrometer throughput) [49, 51] making this kind of tools very suitable for photon-in photon-out applications. In fact, the use of these techniques is still limited, the main limiting factor being the low density of the samples under analysis.

2.3.2 Second Harmonic Generation

One fundamental nonlinear probe is second harmonic generation (SHG), a second order non-linear process in which two photons at the same energy are combined together to generate a single photon having twice the energy [52]. This technique exploits the enhancement of the second-order nonlinear response to a high intensity, coherent photon beam when either the intermediate or final state is resonant with a real state within the target material. A schematic energy level diagram of the SHG process is shown in Fig. 2.13. Second harmonic generation is based on the conversion of two photons of frequency ω into a single photon of frequency 2ω.

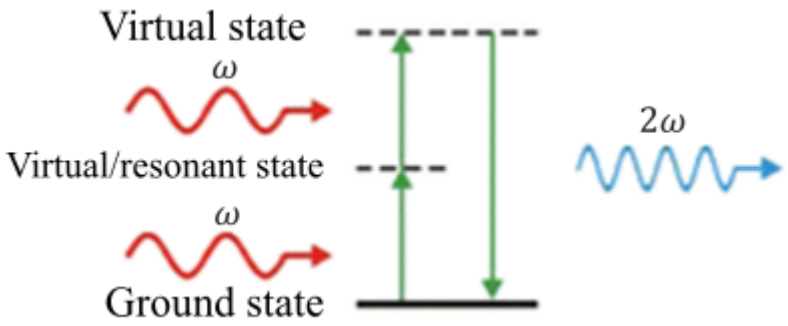

FIGURE 2.12: Schematic energy level diagram of the SHG process.

In the infrared, visible, and ultraviolet domains, second order non-linear spectroscopies are well-known technique for the surface analysis, since symmetry examination within the dipole approximation constrain signal generation to regions without centrosymmetry, such as surfaces and interfaces [53]. On the other hand, at hard x-ray wavelengths, SHG is a bulk-sensitive technique, since it has been observed in centrosymmetric materials with a non-uniform electron density [54]. In the soft x-ray domain there has been uncertainty regarding the interface specificity of soft x-ray SHG. Recently, using a highly coherent, soft x-ray free electron laser, soft x-ray second harmonic generation near the carbon K edge ($\sim$ 284 eV) has been observed [55]. Experimental results and theoretical analysis demonstrate that soft x-ray SHG is an interface-specific probe with symmetry constraints similar to optical SHG, and is sensitive to resonance effects. This could open new perspective for surface and interface analysis in various scientific fields, since the technique combines the elemental specificity of x-ray absorption spectroscopy with the interfacial specificity of second-order nonlinear spectroscopies. The nonlinear response to a coherent input

beam of frequency ω can be derived from an expansion of the polarization of the target medium

$$\overrightarrow{P} = \overrightarrow{X}(1)E + \overrightarrow{X}(2)EE + \overrightarrow{X}(3)EEE \tag{2.28}$$

where $\overrightarrow{X}(n)$ is the nth order susceptibility tensor. Under the dipole approximation the even orders vanish in centrosymmetric media. This makes SHG a surface specific process in centrosymmetric media, as this symmetry is broken only at the interfaces. Assuming a broken-symmetry region with thickness $t << \lambda$, wavelength of the incident radiation, at the resonant photon energies of a given material the intensity of the SHG signal from a given interface is given by:

$$I_{2\omega} \propto \left|X(2)_{eff}\right|^2 I_{\omega}^2 \tag{2.29}$$

where $X(2)_{eff}$ is the effective susceptibility of the interfacial region and I_{ω} is the intensity of the fundamental beam. It is worth to be noted the quadratic dependence of the second harmonic (SH) intensity on the input intensity. Moreover, the surface sensitivity in centrosymmetric media implies that the power dependence of the SH signal is largely invariant with the sample thickness. Prior to the development of XFELs, the lack of light sources with sufficient intensity and coherence has heavily limited the development of nonlinear soft x-ray spectroscopies. With the advent of these sources SHG will open the way to a novel class of interface analysis experiments with higher interfacial specificity than other existing soft x-ray techniques.

Chapter 3

Monochromatic beamlines for TR-ARPES experiments

Angle-Resolved Photo-Emission Spectroscopy (ARPES) is a well known method for studying the electronic structure of materials [56]. The technique is based on photoemission spectroscopy, studying the emission of electrons from a sample illuminated with XUV or soft X-rays radiation. In particular, ARPES measures the distribution of the emitted photoelectrons as a function of their kinetic energy and momentum. Time-Resolved-ARPES (TR-ARPES) extends and complements conventional ARPES by adding time-resolution, usually in the femtosecond time scale [57]. The technique is able to resolve ultrafast dynamics monitoring the behaviour of the electron states after an optical excitation. In detail, a femtosecond pulse (the pump) excites the sample and a subsequent XUV pulse probes the transient electronic structure, after a certain time delay. The High-order Harmonic Generation process described in section 2.1 is a powerful tool for the generation of ultra-short radiation in the XUV/Soft X-ray domain. Although producing a flux that cannot compete with conventional synchrotron sources, HHG temporal properties offer the possibility to perform time-resolved experiments on ultrafast processes never investigated so far. As also claimed, the High Harmonic spectrum is composed of a sequence of peaks corresponding to the odd harmonics of the fundamental laser wavelength. The harmonic intensity decreases rapidly for low harmonic orders, while for higher orders a plateau of equally intense harmonics is found, which extends up to the cut-off wavelength. HHs inherent bandwidth is then often too wide for a large class of experiments, since multiple orders of harmonics are generated coaxially. Therefore, the spectral selection of a single harmonic in a narrow XUV band preserving the pulse duration, is crucial for many time-resolved spectroscopic applications and different technique aimed to study the electronic structures of materials, e.g. TR-ARPES. In this chapter a detailed description of the activities related to the installation and the characterization of two High Harmonic beamlines for TR-ARPES experiments using grating monochromators, is provided. The beamlines are respectively located at the Nanjing University and at Elettra Sincrotrone Trieste. A short technical overview about beamlines for high harmonics using grating monochromators is first of all given in section 3.1. The design and the characterization of the beamlines and the

first experimental results obtained using these sources are described in section 3.2 and in section 3.3.

3.1 Beamlines for High Harmonics using grating monochromators

Different methods are used for the monochromatization of High order Harmonics, such as multi-layer mirrors [58], pulse shaping [59], zone-plate monochromators [60] and monochromator using gratings at grazing incidence [61]. Multilayer mirrors are the simplest optical elements for the spectral selection of harmonics, but they give a poor contrast ratio between adjacent harmonics [62]. A grating monochromator, although more complex than a single multilayer mirror, gives both tunability in a broad range and high spectral selectivity. The process of spectral selection achieved by a grating monochromator should not influence the spatial and temporal characteristics of the pulse that must be monochromatized. Nevertheless, a diffraction grating introduces a stretch of the pulse duration because of the pulse-front tilt, compromising the ultrafast duration of HHs. The pulse front tilt originates from the angular dispersion introduced by an optical element, in this case a grating (but a prism also can be considered), and depends on the spectral content and transversal spatial extension of the considered beam. A very useful model for quantify the effect rely on the consideration that the absolute delay given by each adjacent groove is $m\lambda$, the tilt introduced by a grating is $Nm\lambda$, where N is the number of illuminated grooves, m is the diffraction order, and λ is the incident wavelength. This issue is almost negligible in the picosecond or longer time scale but may completely alter the temporal duration of the XUV pulse in the sub-femtosecond regime. Let us consider a 600 grooves/mm grating illuminated by radiation at 30 nm over a length of 10 mm; the total number of grooves involved in the diffraction is 6000, corresponding to a pulse-front tilt of 180 μm, i.e., 600 fs. Let us examine the condition for the minimum temporal broadening of a XUV pulse using a single grating at the first diffraction order. It is possible to calculate the minimum number of illuminated grooves N_{min} to support a bandwidth $\Delta\lambda$ at wavelength λ using the relation $N_{min} = \lambda/\Delta\lambda$ [63]. The corresponding minimum pulse front-tilt at half-width $\Delta\tau_{G,min}$ for a given bandwidth $\Delta\lambda$ is

$$\Delta\tau_{G,min} \simeq \frac{1}{2}\frac{\lambda N_{min}}{c} = 0.5\frac{\lambda^2}{c\Delta\lambda} \tag{3.1}$$

$\Delta\tau_{G,min}$ is close to $\Delta\tau$, the Fourier limit of a Gaussian pulse with no phase modulation

$$\Delta\tau = \frac{2ln2}{\pi}\frac{\lambda^2}{c\Delta\lambda} \simeq 0.44\frac{\lambda^2}{c\Delta\lambda} \tag{3.2}$$

Since an XUV pulse may be produced to be close to its transform limit, if it passes through a monochromator with minimum pulse-front tilt the minimum pulse duration is the convolution of Eq. (3.1) and (3.2). Hence, a single grating monochromator can be used for the spectral selection of ultrafast pulses without altering too much the pulse duration if the number of illuminated grooves of the grating is equal to the actual resolution. The design of grating monochromators for ultrafast pulses aims to get as closest as possible to this condition. Two different configurations can be employed for the design of grazing-incidence diffraction grating monochromator [64]: the classical-diffraction mount (CDM) and the off-plane mount (OPM).

3.1.1 Grating configurations for ultrafast monochromators

In the CDM geometry, shown in Fig. 3.1 a) the incidence angle α and the diffraction angle β are respectively defined as the angles between the direction of the input beam and the normal to the grating and the direction of the diffracted beam and the normal to the grating. The grating equation is $sin\alpha + sin\beta = m\lambda\sigma_{CD}$, where σ_{CDM} is the groove density of the grating. For a CDM grating monochromator, the subtended angle $K = \alpha + \beta$ is constant and the wavelength selection is performed by rotating the grating around the axis that is tangent to the surface, passes through the grating center and is parallel to the grooves, following the relation

$$\alpha = \frac{K}{2} + arcsin[\frac{m\lambda\sigma_{CDM}}{2cos(K/2)}] \tag{3.3}$$

The number of illuminated grooves of the grating is $N_{CDM} = S\sigma_{CDM}/cos\alpha$, where S is the beam section of the collimated beam. It is worth to be noted that the number of illuminated grooves is reduced if the grating is used at the order $m = -1$. This is a usual choice in order to maintain the number of illuminated grooves as small as possible. The design of a CDM plane-grating monochromator is shown in Fig. 3.1 b). The layout consists of three optical elements: two toroidal mirrors and a plane grating with uniform line-spacing. The first mirror acts as a collimator in order to operate the grating in collimated light, while the second one as a condenser which focuses the beam on the exit slit. This design is commonly known as Czerny–Turner monochromator. The mirrors are generally operated at equal angle and unity magnification to minimize the aberrations at the output [65]. Once the exit arm of the focusing mirror q, has been defined, the output bandwidth is given by:

$$\Delta\lambda_{CDM} = \frac{cos\beta}{m\sigma_{CDM}q}\Delta s \tag{3.4}$$

where Δs is the width of the exit slit of the CDM monochromator. The pulse temporal half-width after the diffraction is:

$$\Delta\tau_{G,CDM} = \frac{1}{2}\frac{m\lambda}{c}S\frac{\sigma_{CDM}}{cos\alpha} \tag{3.5}$$

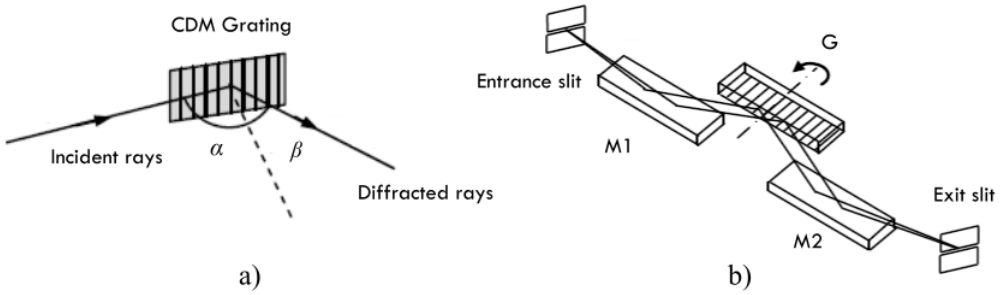

FIGURE 3.1: a) Classical Diffraction Mount (CDM) geometry. b) CDM plane grating monochromator.

The OPM, also called conical diffraction mount, differs from the CDM in the fact that the incident and diffracted wave vectors are almost parallel to the grooves. The OPM geometry is shown in Fig. 3.2 a). The direction of the incoming rays is defined by two parameters: the altitude and the azimuth. The altitude γ is the angle between the direction of the incoming rays and the direction of the grooves, while the azimuth μ of the incoming rays is defined to be zero if they lie in the plane perpendicular to the grating surface and parallel to the rulings. Let ν define the azimuth of the diffracted light at the wavelength λ and at the order m . The grating equation is $sin\gamma(sin\mu + sin\nu) = m\lambda\sigma_{OPM}$, where σ_{OPM} is the groove density of the grating. For an OPM monochromator the grating is operated in the condition $\mu = \nu$ and the wavelength selection is performed by rotating the grating around the axis that is tangent to the surface, passes through the grating center and is parallel to the grooves, following the relation

$$\mu = arcsin[\frac{m\lambda\sigma_{OPM}}{2sin\gamma}] \tag{3.6}$$

The number of illuminated grooves of the grating is $N_{OPM} = S\sigma_{OPM}/cos\mu$. The grating, in this case, can be used indifferently at the orders $m = \pm 1$, since this does not change the illuminated area. Again, once fixed the exit arm of the focusing mirror q the output bandwidth is given by:

$$\Delta\lambda_{OPM} = \frac{cos\mu}{m\sigma_{OPM}q}\Delta s \simeq \frac{\Delta s}{m\sigma_{OPM}q} \tag{3.7}$$

where Δs is the width of the exit slit of the OPM monochromator. The pulse temporal half-width after the diffraction is:

$$\Delta\tau_{G,OPM} = \frac{1}{2}\frac{m\lambda}{c}S\frac{\sigma_{OPM}}{cos\mu} \simeq \frac{1}{2}\frac{m\lambda}{c}S\sigma_{OPM} \tag{3.8}$$

The approximations in Eq. (3.6) and (3.7) are assumed for low resolution designs (when $\mu < 10°$). The design of an OPM plane-grating monochromator is shown in Fig. 3.2 b).

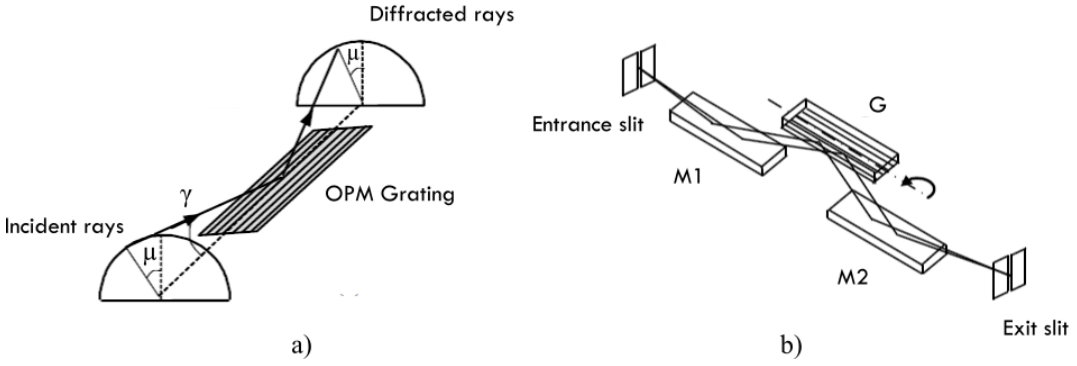

FIGURE 3.2: a) Off-Plane Mount (OPM) geometry. b) OPM plane grating monochromator.

The diffraction efficiency of both the schemes is maximized in the blaze condition. In case of saw-tooth profiles with blaze angle δ, the condition is verified for $\delta = (\alpha - \beta)/2$ in the CDM and for $\delta = \mu$ in the OPM. The main advantage of the OPM is the higher diffraction efficiency, which has been measured to be actually close to the coating reflectivity at the same altitude angle [66]. The resulting grating efficiency, when compared to a similar grating used in the CDM, is higher by a factor 2-3 [67]. It is worth to be noted that for a given beam section, the CDM and the OPM configurations have the same temporal response if $\sigma_{CDM}/cos\alpha = \sigma_{OPM}/cos\mu$.

Hence, the groove densities to be used to have the same resolutions and the same temporal responses is much lower in the CDM than in the OPM, because typically α is in the range of $74^\circ - 86^\circ$ for grazing-incidence configurations and μ is lower than 10°. It has been shown that the grating parameters required to give temporal responses below ≈ 100 fs in the CDM are at the limit of current feasibility, since the groove density is typically very low and the resulting blaze angle to maximize the efficiency is below the present manufacturing capabilities, resulting in a very poor grating efficiency. On the other side, the gratings to be used in the OPM are standard models, both in terms of groove density and blaze angles, providing simultaneously short temporal response and high efficiency [68]. This makes the OPM a suitable candidate for the realization of monochromators with ultrafast response.

3.1.2 General scheme of a High Harmonic beamline using a grating monochromator

A General scheme of a High Harmonic beamline using a grating monochromator is shown in Fig. 3.3. These facilities are based on a high repetition rate and ultra-short tunable laser source, which is used to produce ultra-fast XUV pulses through HH generation. The driving laser is typically focused on a gas-jet produced by a nozzle or a gas cell installed in the generation chamber. Here, the interaction of the ultrafast pulse with the gas (usually Argon, Krypton or Neon) produces high harmonics.

The generation efficiency can be maximized varying the laser intensity, the gas pressure inside the cell and the relative position of the laser focus within the cell. The monochromator chamber contains all the optical elements that perform the spectral selection of a single harmonic, or a sub-band of it. Depending on the requirements, it can be designed in the OPM geometry (with minimum pulse-front tilt for ultrafast response, although low resolution) or in the classical diffraction mount geometry (for high resolution, despite long temporal response). The exit slit block is placed right after the monochromator and it mounts a couple of slits (placed vertically in the case of CDM or horizontally in the case of OPM) which function is the control of the bandwidth at the output of the monochromator. The chamber mounts a calibrated detector that can be inserted in the beam path in order to measure the XUV photon flux at the output of the exit slit block. At this point the beam can be filtered through an Al filter, that may be inserted in the optical path to stop the residual diffused IR light, before it enters the refocusing chamber. The refocusing section hosts a grazing-incidence toroidal mirror to focus the XUV monochromatized beam at the sample position. For time resolved experiments, part of the driving power can be used as probe or can be sent to an Optical Parametric Amplifier (OPA) in order to obtain a desired wavelength. A delay-line installed in the section transporting the beam allows to control the optical path difference between the probe and the pump beams with sub-micrometer precision, in order to perform time-resolved experiments. The probe is recombined in the experimental chamber by means of a flat mirror hosted in the recombination section. The mirrors are usually installed in motorized mounts, in order to perform a good and remotely controlled spatial overlap between the pump and probe beams onto the target placed in the experimental chamber. The pump and probe beams are recombined almost collinearly in order to minimize the temporal resolution spread. Generally, the recombination and the refocusing sections are joined together in a single chamber. All the chambers are pumped by turbo pumps and connected fore-vacuum scroll pumps, in order to ensure an appropriate level of vacuum in the sections where XUV propagates. Each section of the vacuum-beamline can be isolated by means of manually or electrically controlled gates. A set of differential pumping pinholes, opportunely sized, is generally employed to guarantee the desired level of vacuum in each chamber of the system. In the generation chamber the pressure during operation is typically in the range of 10^{-3} mbar, while pressures in the monochromator and in the experimental chambers are, respectively, in the range of 10^{-6} mbar and 10^{-10} mbar.

3.2 The Beamline at Nanjing university

3.2.1 Beamline design

The beamline located at the Nanjing University is schematically shown in Figure 3.4. An innovative design using an OPM grating monochromator is able to minimize the stretch of the pulse duration.

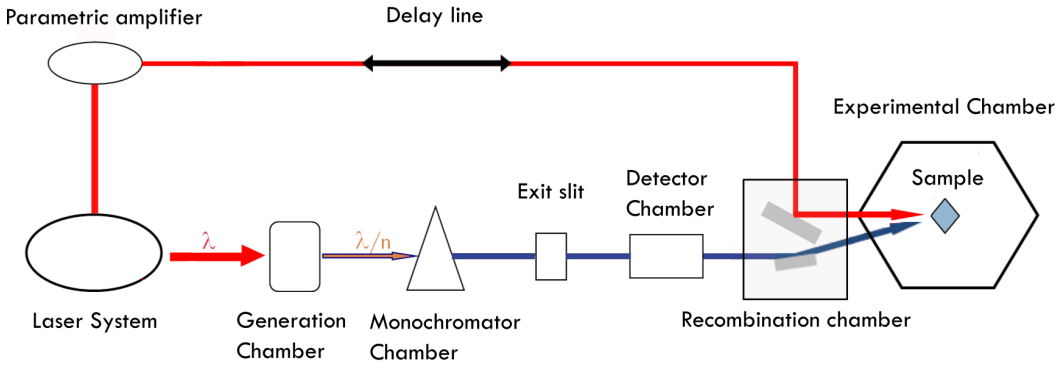

FIGURE 3.3: General scheme of a High Harmonic beamline using a grating monochromator.

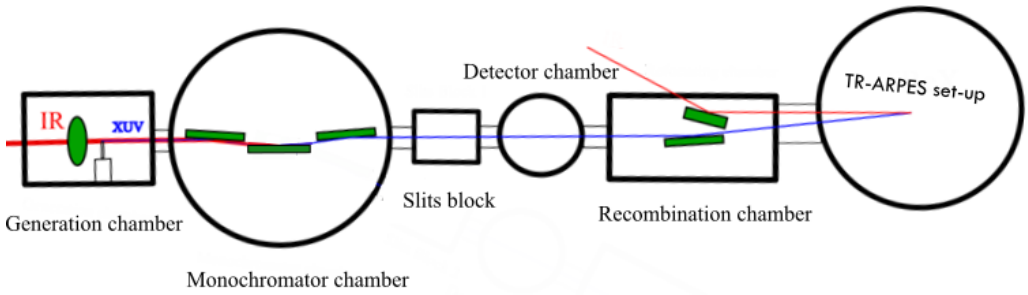

FIGURE 3.4: A Schematic of the Nanjing University High Harmonic beamline.

XUV radiation in the wavelength range 12.4 - 124 nm (10 – 100 eV) is produced by HH generation in a gas nozzle using 50-fs, 800 nm laser pulses at 1 kHz repetition rate, produced by a Ti:Sapphire. The generation chamber has been designed to install a 1 KHz pulsed gate valve for the gas injection. HHs can be generated by the laser fundamental wavelength (using a 4 mJ/pulse) or by its 2nd harmonics (generated by means of a thin BBO crystal). The laser pulses are focused on the gas nozzle through a lens. The spectral selection of a single harmonic is performed by an off-plane mount grating monochromator. The instrument consists of the following optical elements: two gold coated toroidal mirrors and an array of OPM plane gratings with uniform line-spacing. The optical design of the instrument is based on the Czerny-Turner monochromator described in the previous section. The mirrors are operated at equal grazing angle and unity magnification (i.e., the length of the input arm p is equal to the length of the output arm q), in order to minimize the aberrations at the output. The grazing angles and the lengths of the input and exit arms have been chosen to be respectively 3° and 500 mm. The instrument adopts three gratings having different grooves densities (150 gr/mm, 300 gr/mm and 600 gr/mm) to cover the whole spectral range. The parameters of the optical elements of the monochromator are reported in Table 3.1. In order to automatically perform the

TABLE 3.1: Parameters of the optical elements of the Nanjing University monochromator

Spectral region	10.8 - 100 eV	
Toroidal mirrors	Incidence angle	3°
	Input-output arms	500 mm
	Coated area	50 mm × 10 mm
	Coating	Gold
	Maximum acceptable angle	5 mrad × 5 mrad
Gratings	Ruled area	50 mm × 10 mm
	Altitude	3.5°
G1	Energy region	10.8 - 40 eV
	Groove density	150 gr/mm
	Bandwidth (100 μm slit)	$\Delta\lambda$= 1.3 nm, ΔE= 0.4 eV @ 20 eV
G2	Energy region	10.8 - 40 eV
	Groove density	300 gr/mm
	Bandwidth (100 μm slit)	$\Delta\lambda$= 0.7 nm, ΔE= 0.2 eV @ 20 eV
G3	Energy region	30 - 100 eV
	Groove density	600 gr/mm
	Bandwidth (100 μm slit)	$\Delta\lambda$= 0.3 nm, ΔE= 0.7 eV @ 50 eV

grating selection and rotation, a motorized rotator and a linear translation stage are installed inside the monochromator. The motors are connected together to realize the grating support. The required precisions for rotation and translation are respectively 0.01° and 50 μm, well within the capabilities of any commercial component. When the grating is rotated to perform the spectral selection of the harmonic, the IR beam is diffracted on the 0th-order, out of the optical axis and it is blocked by a suitable beam-stop placed before the last toroidal mirror. A picture of the chamber of the monochromator is shown in Fig. 3.5 a), while in Fig. 3.5 b) the optical elements of the instrument are clearly visible.

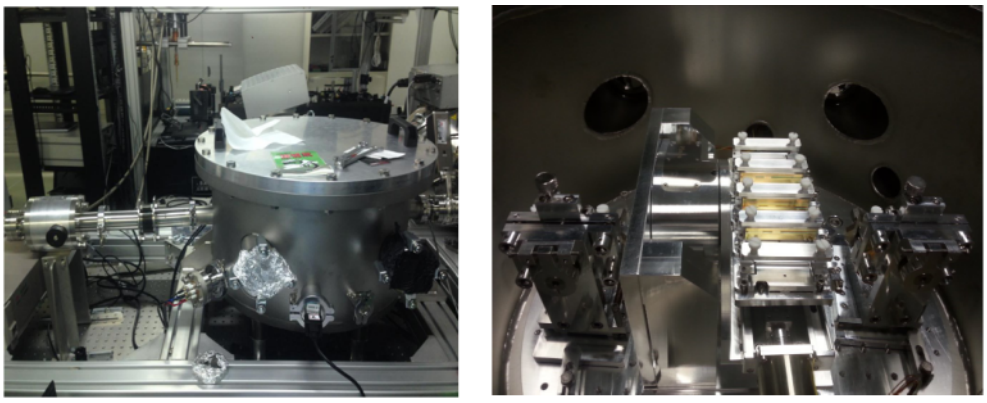

a) b)

FIGURE 3.5: a) Chamber of the monochromator. b) Optical elements and motors inside the monochromator.

The monochromator has been designed to provide an energy resolution sufficient to select a single harmonic, considering a separation between adjacent harmonics of 3.1 eV (with the 800 nm driving laser). The output bandwidth of the monochromator obtained on a 100 μm slit with different gratings is shown in Fig. 3.6 a). The ultimate temporal response of the monochromator is limited by the pulse-front tilt due to diffraction, that depends on the number of illuminated grooves, therefore on the XUV beam divergence. The pulse-front tilts calculated with a 2 mrad FWHM beam divergence are shown in Fig. 3.6 b).

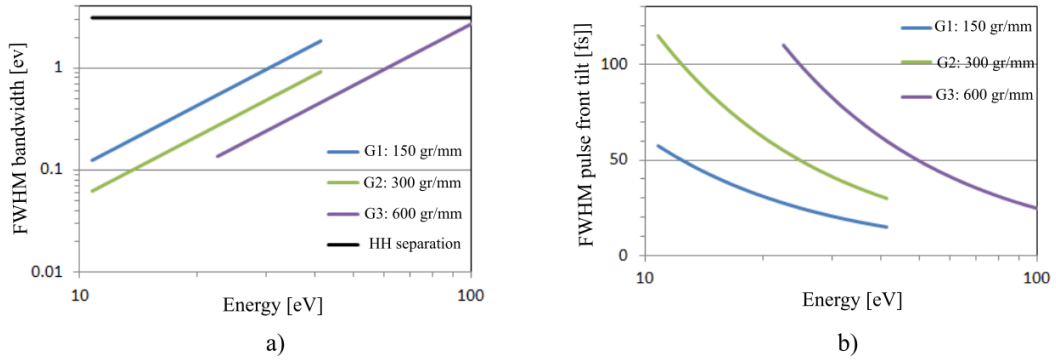

FIGURE 3.6: a) Calculated FWHM output bandwidth provided by the gratings on 100 μm slit. b) Calculated Pulse-front tilt given by the gratings for a 2 mrad FWHM beam divergence.

The exit slits block contains the horizontal slits that stop all the undesired radiation, performing the selection of a narrow band of the harmonics. The resolution of the monochromator can be increased by closing the slit, although losing part of the photon flux. The absolute monochromatic XUV photon flux can be measured with a calibrated NIST EUV photodiode, installed in a chamber after the exit slits block of the monochromator. The current emitted by the photodiode can be measured with a Keithley 6517 picoamperometer, which can be remote-controlled with a PC for consecutive current readings during the harmonics scanning. An overall view of the monochromator with its exit slit block and the chamber containing the detector is shown in Fig. 3.7 a). The refocusing chamber hosts a grazing-incidence gold coated toroidal mirror which focuses the monochromatized XUV light at the sample position with unity magnification. The grazing incidence angle and the length of the input and exit arms of the mirror have been chosen to be respectively 3° and 1000 mm. For Time resolved experiment, part of the driving laser power is sent to an OPA in order to obtain a desired wavelength. A delay-line made up of plane mirrors is installed in the section transporting the OPA beam and allows the control of the optical path difference between the IR and the XUV beam. The OPA beam is recombined in the end-station by means of a flat mirror hosted in the refocusing/recombination chamber. All the mirrors hosted in the refocusing/recombination section are installed in piezo motorized mounts that can be remotely controlled to perform a precise spatial overlap on the target between the pump and probe beams. The pump

and the probe beams are recombined almost collinearly. The end-station consists of a TR-ARPES set-up equipped with a Phoibos 100/150 hemispherical electron analyzer, conceived for high-resolution ARPES measurements. The sample is mounted on a manipulator supplied with a helium cryostat which enables the cooling of the sample. The preparation chamber of the set-up allows the cleaning and the preparation of the sample via sputtering by means of an ion-gun installed in the same vessel. A load-lock chamber based on a fast-entry arrangement allows the rapid insertion of samples in the facility. A picture of the beamline in which are visible the refocusing/recombination section and the experimental set-up is reported in Fig. 3.7 b). All the chambers are pumped by turbo pumps and connected fore-vacuum scroll pumps, in order to ensure an appropriate vacuum level in the sections where XUV propagates. Each chamber of the beamline is isolated from the others by means of manually controlled gates. The level of pressure in the generation chamber during gas-injection is in the range of 10^{-3} mbar. A set of differential pumping pinholes, opportunely sized, is employed to guarantee a vacuum level of 10^{-6} mbar in the monochromator and 10^{-10} mbar in the experimental chamber.

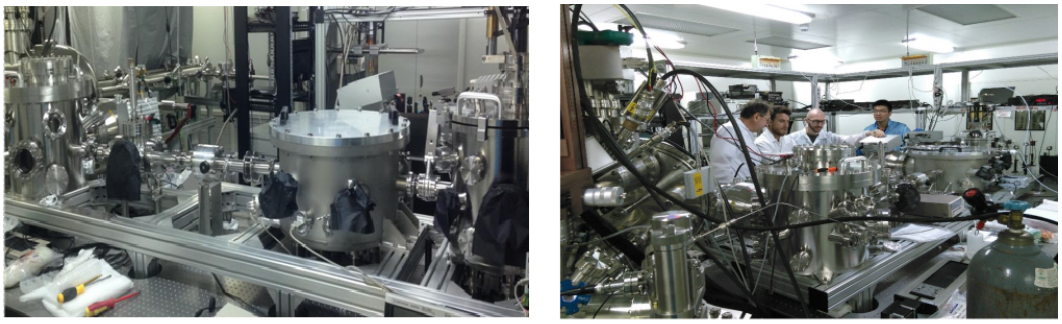

a) b)

FIGURE 3.7: a) Picture of the chamber of the monochromator with its exit slit block and the chamber containing the detector. b) Overall view of the beamline, with the refocusing/recombination section and the experimental chamber.

3.2.2 Installation and characterization of the beamline

The optical alignment of the beamline has been accomplished using a low-intensity visible red laser (He-Ne, $\lambda = 630$ nm), to achieve an appropriate displacement of the optical elements inside the chambers of the system. The optical path of the visible laser has been obtained using two plane mirrors mounted on kinematic mounts in order to center with high accuracy the beam with the entrance and exit ports of the generation chamber. Two iris diaphragms have been used to limit the effects of diffraction near the entrance of the monochromator and to "mark" the path of the laser beam. A 100 μm pinhole simulating the HH source has been then aligned with the beam and placed at the nominal distance from the center of the first toroidal

mirror. Then, the accurate precision adjustments of the rotations and of the positions of the optical elements of the monochromator have been performed. At this point, the verification of the spot profile at the exit of the monochromator has been accomplished through a beam-profiler camera. The beam profiles at the exit of the monochromator in the focal position are shown in Fig. 3.8. The measured exit spots are compatible with the size of the pin-hole placed in the experimental chamber.

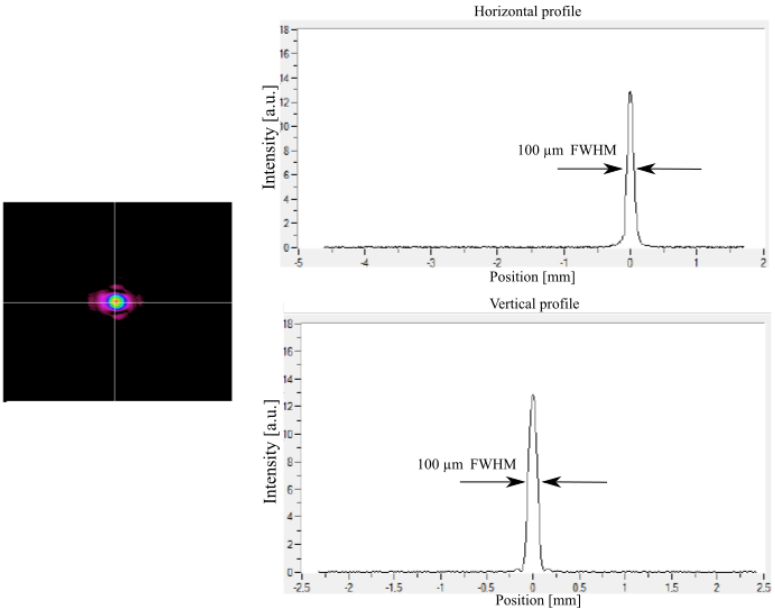

FIGURE 3.8: Beam profile in the visible at the exit of the monochromator.

Subsequently, the positioning and the alignment of the horizontal slits a have been achieved. When the alignment of these blocks has been finished, we dealt with the installation of the gas-nozzle. Particular attention has been paid to the alignment of the gas nozzle, in order to center the gas-jet with the beam coming from the driving laser. Once the preliminary alignment in air has been completed, the system has been sent in high-vacuum and the gas has been injected in the gas-nozzle. The pressure inside the generation chamber is in the 10^{-3} mbar range during the gas-injection.

HH spectra from Argon and Neon have been measured performing angular scans of the gratings of the monochromator through a LabVIEW control program. In Fig. 3.9 some typical HH spectra acquired with the laser fundamental at 800 nm are shown. The Ar harmonics reported in Fig. 3.9 a) are generated with a 1.6 mJ pulse, focused through a 50 cm focal length. A maximum flux of 5.5 x 10^{10} ph/s is measured at the HH17 (26.4 eV). Whereas, the HHG spectrum of Ne and reported in Fig. 3.9 b) is obtained using a 3mJ pulse with shorter focal length of 30 cm. Photon fluxes as high as 3 x 10^{8} ph/s at HH29 (45 eV) have been measured. It is worth to be noted that, due to its higher ionization potential, the generation efficiency in Neon is much lower than the generation efficiency in Argon.

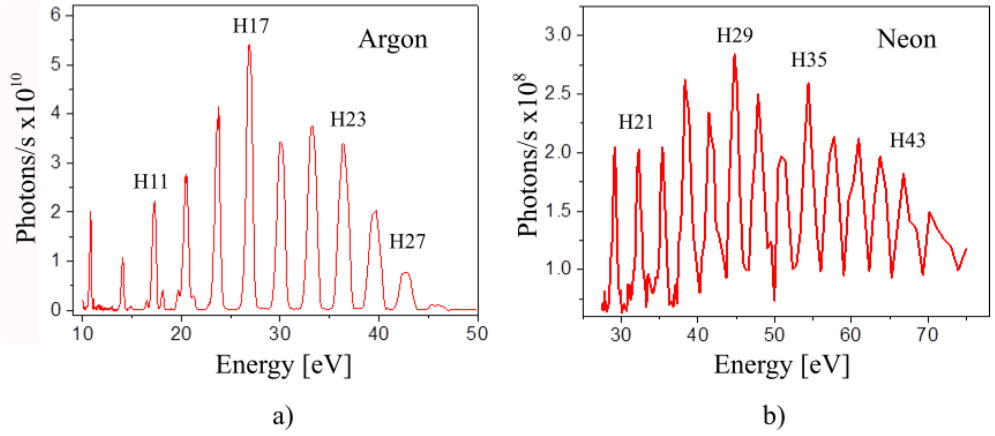

FIGURE 3.9: Typical HH spectra in Argon and in Neon generated with a 800 nm driving pulse. a) Harmonics generated in Argon with 1.6 mJ pulse, using a 50 cm focal length b) Harmonics generated in Neon with 3 mJ pulse using a 30 cm focal length.

Argon and Neon HH spectra obtained with the second harmonic generation (SHG) of the driving laser have been also measured. The second harmonic has been obtained focusing the fundamental of the laser through a thin BBO crystal. In Fig. 3.10 some typical HH spectra acquired with the second harmonic of the fundamental (400 nm) are shown. The Ar and Ne harmonics reported respectively in Fig. 3.10 a) and in Fig. 3.10 b) are generated with a 1.2 mJ pulse and focused through a 30 cm focal length. The HH spectrum of Ar, presents a maximum photon flux of 1.2 x 10^{11} ph/s, measured at the HH7 (21.7 eV). The HH spectrum of Ne, generated with the SHG laser pulse presents a maximum photon flux of 5.5 x 10^{9} ph/s, measured at HH15 (46.5 eV). Note that the spectral line separation of the HH generated with the second harmonic is twice the separation of HH obtained with the fundamental laser, which is estimated to be 3.1 eV. In accord with the theory, the generation efficiency is enhanced using a shorter wavelength.

The reported spectra confirm the capability to resolve adjacent harmonics separated by 3.1 eV, when XUV is generated using an 800 nm driving laser.

As also mentioned, the temporal response of the monochromator is limited by the pulse-front tilt, that depends on the number of illuminated grooves and therefore on the XUV beam divergence. The latter has been measured by a knife-edge technique to be 2 mrad for HH15 and 1.3 mrad for HH21. The corresponding pulse-front tilts are therefore in accord with those calculated and presented in the previous section. The XUV beam at the exit of the monochromator is focused on the sample placed in the ARPES apparatus by the toroidal mirror hosted in the refocusing chamber. The latter has been finely aligned with visible radiation, as well. The measure of the profiles of the XUV focal spot has been accomplished using a CE:YAG crystal which is placed into the center of the ARPES chamber. The fluorescence emitted by the CE:YAG and induced by the irradiated XUV is recorded by a CCD camera. In Fig. 3.11 a) the XUV focal spot of the HH15 on the CE:YAG crystal is shown.

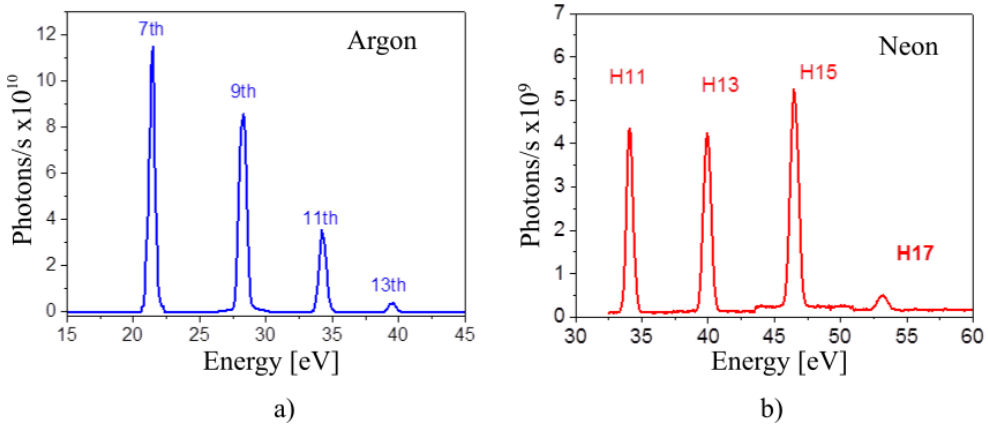

FIGURE 3.10: Typical HH spectra in Argon and in Neon generated with a 400 nm driving pulse with 1.2 mJ pulse using a 30 cm focal length. a) Harmonics generated in Argon b) Harmonics generated in Neon.

The vertical and horizontal profiles of the spot are fitted by Gaussian functions and the corresponding FWHM are 170 μm for the horizontal profile and 120 μm for the vertical profile, as shown in Fig. 3.11 b).

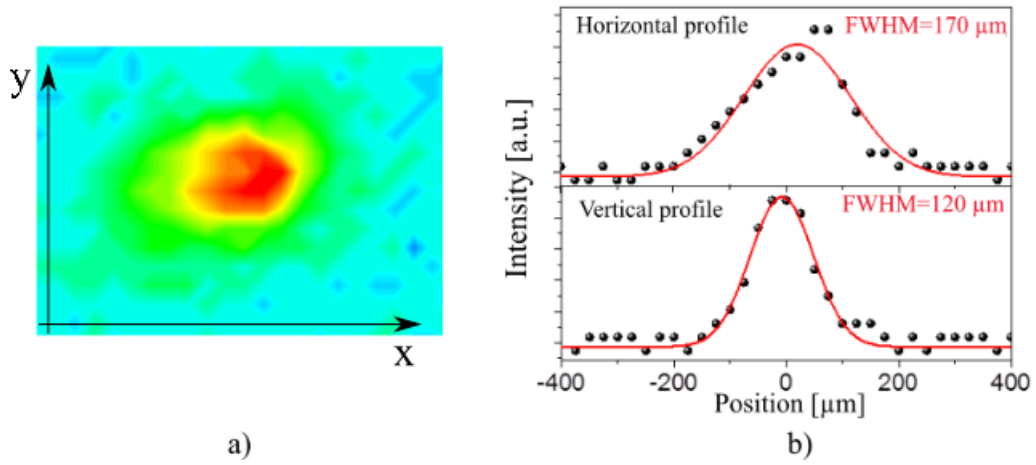

FIGURE 3.11: XUV focal spot. a) CCD image of the fluorescence emitted by the CE:YAG crystal. b) Measured focal spot profiles (Horizontal FWHM =170 μm, Vertical FWHM=120 μm).

3.2.3 Experimental results

First Static ARPES spectra have been obtained using the HH beamline. The sample consisted in a Cu (111) crystal at room temperature (T=300 K). The beamline has been operated at a repetition rate of 1 kHz using the fundamental of the driving laser. The photon flux of the XUV beam after the refocusing mirror has been estimated to be 6 x 10^8 ph/s and the spot size area on the sample was 170 μm x 120 μm. The harmonic HH13 (20.15 eV) has been selected using the grating G2 (300 gr/mm), while the

monochromator silts have been opened at 100 μm. In Fig. 3.12 a) the measured snapshot of the Cu (111) band structure, is shown. The spectrum has been recorded in a relatively short time (20 minutes). For comparison, in Fig. 3.12 b) an ARPES image obtained with radiation from He-I line (21.22 eV) is reported. The spectrum measured using the HH beamline as light-source is in full agreement with the data acquired using the Helium lamp.

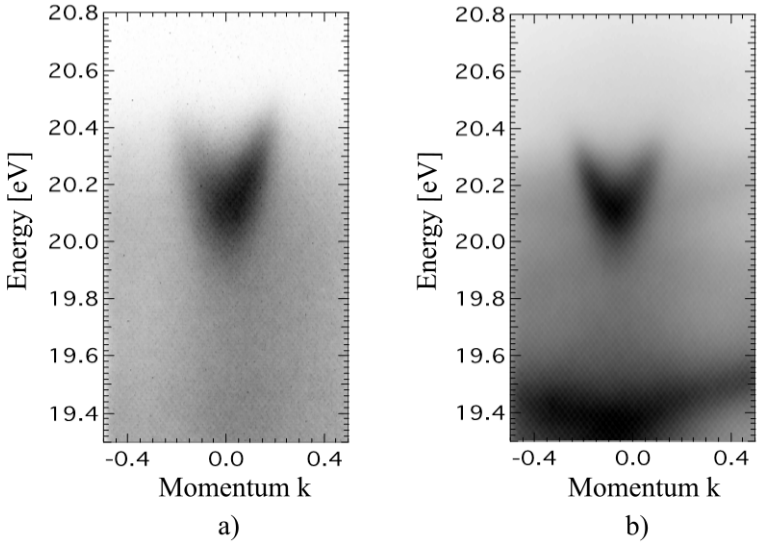

FIGURE 3.12: ARPES snapshots of Cu (111) at room temperature band structure. a) ARPES obtained using the HH beamline and selecting the HH13 (20.15 eV). b) ARPES obtained with a Helium lamp and using the He-I line at 21.22 eV.

The effect of space charge on the ARPES measurements, due to the high peak photon flux, was also evaluated at the Fermi-edge of the Cu (111) crystal, in order to characterize the ARPES energy resolution. Space charge effects occur when very intense and very short radiation pulses produces a huge number of photoelectrons that are emitted from the sample surface. When a sufficient number of electrons simultaneously leave the surface, their Coulombic interaction causes a variation in their kinetic energy and momentum that affects the features of the recorded energy spectrum, inducing broadenings and shifts of the photoelectrons spectra structures, with a consequent loss in energy resolution. For these tests, the XUV photon energy has been set at the harmonic HH13 using the grating G2 and the monochromator slits have been opened at 100 μm. The photon fluxes have been varied from 5.7 x10^9 to 6 x10^8ph/s and the space charge broadening and shifting of the Fermi-edge for different photon fluxes have been observed.

Evidently, in order to minimize the space charge effects, it is necessary to control the photon density on the sample. This can be achieved by increasing the XUV focal spot area at the sample (placing the sample slightly out of the focal position) or reducing the photon flux at the sample (closing the slits of the monochromator, decreasing the energy per pulse of the driving laser or detuning the gas-cell).

3.3 The Beamline at ELETTRA Sincrotrone Trieste

3.3.1 Beamline design

A novel source for TR-ARPES experiments, which is based on XUV high harmonics produced by a high-repetition-rate and ultra-short laser source, has been recently designed, installed and characterized at FERMI @ Elettra. The beamline is schematically shown in Fig. 3.13.

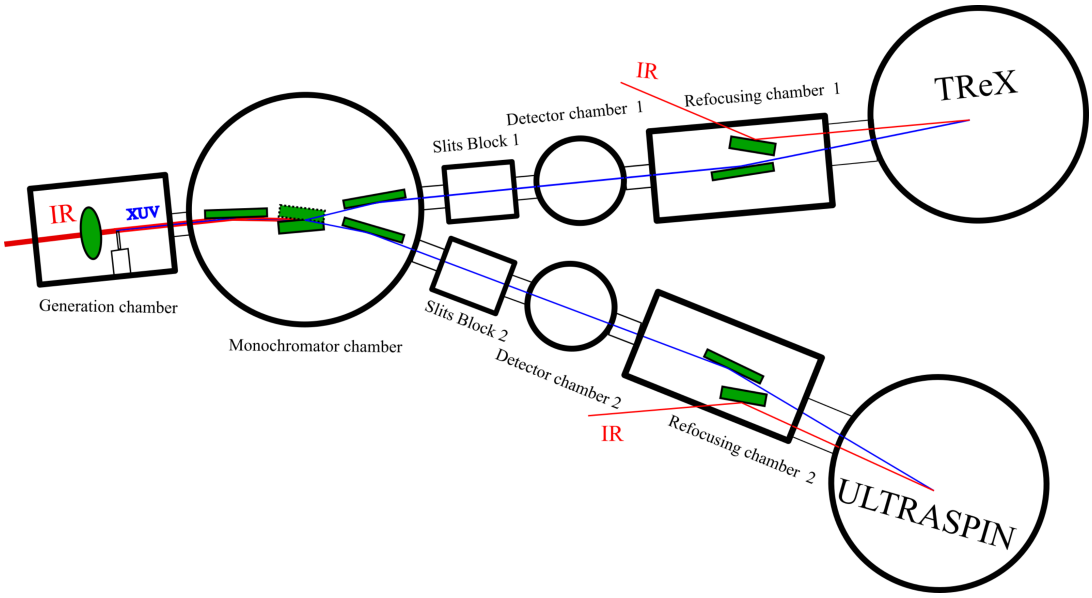

FIGURE 3.13: A Schematic of the Elettra High Harmonic beamline.

XUV radiation in the wavelength range 10 - 100 nm (12.4 – 124 eV) is produced by HH generation in a gas nozzle using 300-fs laser pulses at 50 kHz repetition rate, produced by an Yb:KGW amplifier (Light Conversion Pharos). HHs can be generated by the laser fundamental wavelength (using 400 μJ/pulse at 1030 nm) or by its 2nd harmonics (using 200 μJ/pulse at 515 nm). The laser pulses are focused on the gas nozzle through a f=10 cm lens. The generation chamber of the HHG beamline is shown in Fig. 3.14 a). The cube containing the gas nozzle is visible in Fig. 3.14 b). It is installed in an x-y-z manipulator to allow the alignment of the holes of the cube with the incoming IR-light and it is pumped through the bellow visible in the picture by means of a scroll pump. The gas inlet is also clearly represented as shown in Fig. 3.14 c); plasma on the gas-jet is clearly observable during operation of the laser system and it is also a good diagnostic for the optimization of the generation.

The spectral selection of a single harmonic is performed by an off-plane mount grating monochromator. The monochromator provides XUV monochromatic beam to two different setups, namely the T-ReX TR-ARPES endstation [69] and ULTRASPIN endstation [70]. The instrument consists of the following optical elements: two toroidal gold coated mirrors and two arrays of OPM plane gratings with uniform line-spacing. The optical design of the instrument is based on the Czerny-Turner

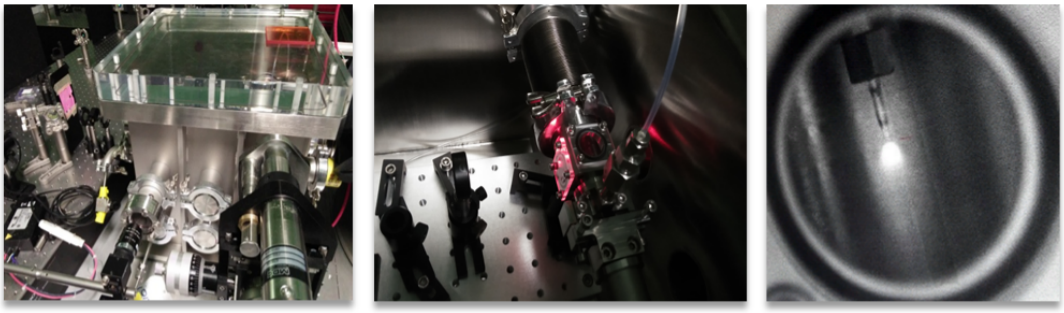

FIGURE 3.14: a) The generation chamber of the HHG beamline. b) The cube containing the gas nozzle. c) plasma on the gas-jet observable during the operation of the laser system.

monochromator. The mirrors are operated at equal grazing angle and unity magnification (i.e., the length of the input arm p is equal to the length of the output arm q), in order to minimize the aberrations at the output. The grazing angles and lengths of the input and exit arms of the mirrors have been chosen to be respectively 4° and 300 mm. The instrument adopts two arrays of grating each for one of the two end-stations. T-ReX branch use two gratings (200 gr/mm and 400 gr/mm) to cover the 10 - 30 eV range, while ULTRASPIN branch employs three grating to cover the 8 - 100 eV range (200 gr/mm, 400 gr/mm and 1200 gr/mm). An innovative and compact design allows sending the monochromatic beam to one of the two independent end-stations acting only on the grating selection, without any additional moving element. The parameters of the optical elements of monochromator are reported in Table 3.2.

TABLE 3.2: Parameters of the optical elements of the ELETTRA Trieste monochromator

Spectral region	10 - 100 eV	
Toroidal mirrors	Incidence angle	4°
	Input-output arms	300 mm
	Coated area	90 mm × 10 mm
	Coating	Gold
	Maximum acceptable angle	20 mrad × 20 mrad
Gratings	Ruled area	70 mm × 10 mm
	Altitude	5°
G1: TREX, ULTRASPIN	Energy region	8 - 32 eV
	Groove density	200 gr/mm
	Bandwidth (100 μm slit)	ΔE= 0.5 eV @ 20 eV
G2: TREX, ULTRASPIN	Energy region	30 - 50 eV
	Groove density	400 gr/mm
	Bandwidth (100 μm slit)	ΔE= 0.8 eV @ 40 eV
G3: ULTRASPIN	Energy region	50 - 100 eV
	Groove density	1200 gr/mm
	Bandwidth (100 μm slit)	ΔE= 1.45 eV @ 80 eV

In order to automatically perform the grating selection and rotation, a motorized rotator and a linear translation stage are installed inside the monochromator. A support holds the five gratings in sequence, which can be rotated and translated with a precision of 0.005° and 5 μm. When the gratings are rotated to perform the spectral selection of the harmonic, the IR beam is diffracted on the 0th-order, out of the optical axis and it is blocked by two suitable beam-stops placed before the last toroidal mirrors. A picture of the chamber of the monochromator is shown in Fig. 3.15 a), while in Fig. 3.15 b) the optical elements of the instrument are clearly visible.

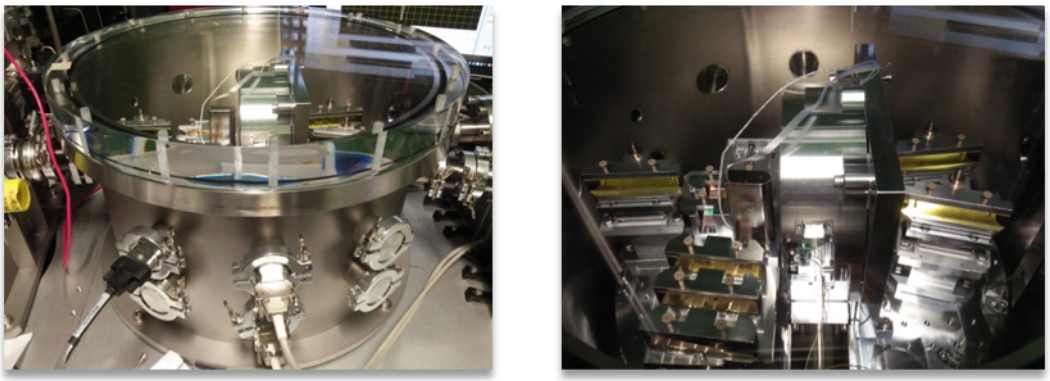

FIGURE 3.15: a) Chamber of the monochromator b) Optical elements and motors inside the monochromator chamber.

The monochromator has been designed to provide an energy resolution sufficient to select a single harmonic, considering a separation between adjacent harmonics of 2.4 eV (with the 1030 nm driving laser). The output bandwidth of the monochromator obtained on a 100 μm slit with different gratings is shown in Fig. 3.16 a). The ultimate temporal response of the monochromator is limited by the pulse-front tilt due to diffraction, that depends on the number of illuminated grooves, therefore on the XUV beam divergence. The pulse-front tilts calculated with a 10 mrad FWHM beam divergence are shown in Fig. 3.16 b).

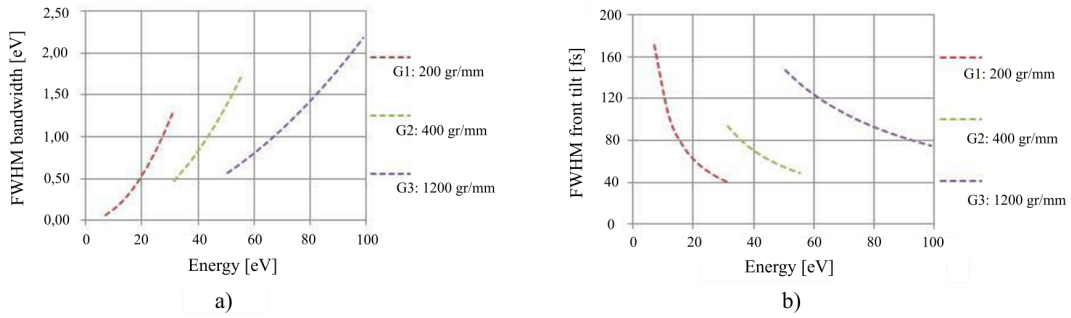

FIGURE 3.16: a) Calculated FWHM output bandwidth provided by the gratings on 100 μm slit. b) Calculated Pulse-front tilt given by the gratings for a 10-mrad FWHM beam divergence

The exit slits blocks contain the vertical slits that block all the undesired radiation, performing the selection of a narrow band of the harmonics. The resolution of the monochromator can be increased by closing the slit, although losing part of the photon flux. The detection of the photon fluxes can be performed by a couple of calibrated Dr. Sjuts Channel Electron Multiplier (CEM) installed in two vacuum chambers (each for one of the end-stations) placed after the exit slits of the monochromator. The current emitted by the CEM is then measured by a Keithley picoamperometer, which can be remote controlled with a PC for consecutive current readings during the rotation of the gratings. For Time resolved experiment, part of the driving laser power is sent to an OPA in order to obtain a desired wavelength. A delay-line made up of plane mirrors is installed in the section transporting the OPA beam and allows the control of the optical path difference between the IR and the XUV beams. The OPA beam is recombined in the end-stations by means of a flat mirror hosted in the recombination chambers. These chambers host also grazing-incidence toroidal mirrors to focus the XUV monochromatized beam at the sample position. The mirrors are operated with unity magnification. The length of the input and exit arms of these mirrors have been chosen to be 1300 mm. The mirrors are installed in a piezo motorized mounts, in order to perform a perfect spatial overlap between the pump and probe beams. The pump and probe beams are recombined almost collinearly. A scheme of the refocusing/recombination sections and of the two experimental chambers is reported in Fig. 3.17 a). As also mentioned the beamline provides XUV ultrafast pulses to the T-ReX TR-ARPES set-up (in the 15-35 eV range) and to the Ultraspin TR-ARPES end-station (in the 10-70 eV or 18-90 nm). The T-ReX TR-ARPES set-up is composed by three interconnected chambers. The experimental chamber is equipped with a Specs Phoibos 225 hemispherical electron-analyzer, conceived for high-resolution ARPES measurements. In this environment the sample is mounted on a six degrees of freedom manipulator supplied with a helium cryostat that enables the cooling of the sample. The preparation chamber of the set-up allows the cleaning of the sample via sputtering and annealing or by cleaving. The same chamber hosts a LEED (Low Energy Electron Diffraction) spectrometer, employed for the analysis of the surface quality of the sample. The growth of the sample can be also accomplished via electron beam deposition. Finally, the load-lock chamber is based on a fast-entry arrangement that permits the rapid insertion of samples in the facility. Similarly, the ULTRASPIN end-station consists in a series of interconnected vessels. The experimental chamber is equipped with a Scienta SES-2002 electron spectrometer. The sample can be cryogenic cooled and electric/magnetic fields can be applied to the sample. The preparation chamber allows the sample cleaning treatments (via sputtering-annealing or cleaving) and the deposition of ultrathin films via electron beam deposition. Low Energy Electron Diffraction and Auger Electron Spectroscopy characterizations of the surface are also achievable. Again, a fast-entry arrangement permits the insertion of samples in the facility in short times. A picture of the two experimental apparatus is reported in Fig. 3.17 b).

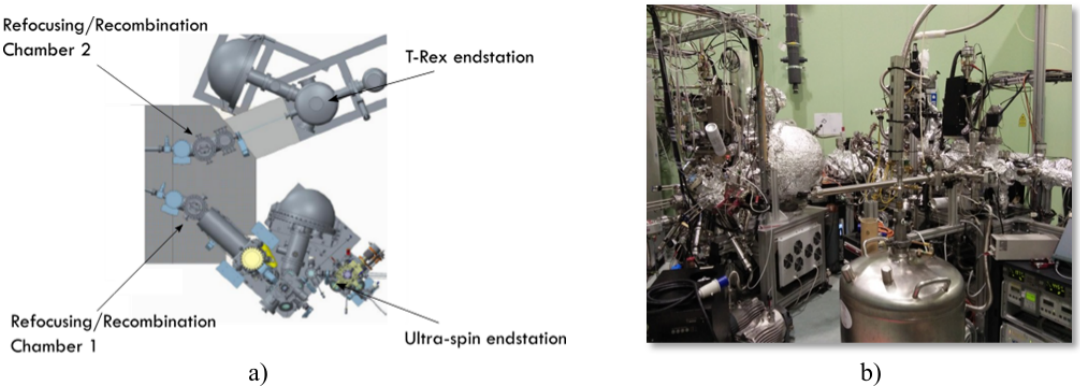

FIGURE 3.17: a) Schematic representing the refocusing/recombination sections and the two experimental chambers. b) A picture of the two experimental apparatus.

All the chambers are pumped by turbo pumps and connected fore-vacuum scroll pumps, in order to ensure the vacuum in the sections where XUV propagates. Each chamber can be isolated by means of electrically controlled gates. A set of differential pumping pinholes is employed to guarantee the desired level of vacuum in each chamber of the beamline. In the generation chamber the pressure during operation is typically in the range of $10^{-2} - 10^{-3}$ mbar, while pressures in the monochromator and in the experimental chambers are, respectively, in the range of 10^{-6} mbar and 10^{-10} mbar.

3.3.2 Installation and characterization of the beamline

The optical alignment procedure is similar to the one presented in the previous section. A picture taken during the fine-alignment of the optical elements of the instrument is shown in Fig. 3.18 a). The profile of the beam at the exit of the monochromator in the focal plane is shown in Fig. 3.18 b). The measured exit spot is compatible with the size of the pin-hole that simulates the HH source. Once the optical alignment has been achieved, the system has been sent in high-vacuum and the gas has been injected in the gas-nozzle. The pressure inside the generation chamber is in the 10^{-3} mbar range during the gas-injection. HH spectra from Argon and Neon have been measured performing angular scans of the gratings of the monochromator using a LabVIEW software that controls the motors of the monochromator and displays the consecutive currents read from the CEMs

Typical HH spectra generated in Argon and in Neon are reported in Fig. 3.20. The HH spectrum generated in Argon with $\simeq$ 200 μJ, 515 nm driving pulses and 10 cm focusing lens is shown in Fig. 3.19 a). The use of Argon as interacting gas gives harmonics in the photon energy range 15 - 35 eV, with a peak emission in the H9-H13 interval and a cut-off at 36.1 eV (H15). Photon fluxes as high as 3 x 10^7 ph/pulse at 26.5 eV (H11) has been measured at the output of the monochromator, corresponding to $\simeq$ 1.3 x10^{12} ph/s at 50 KHz repetition rate, available on the target

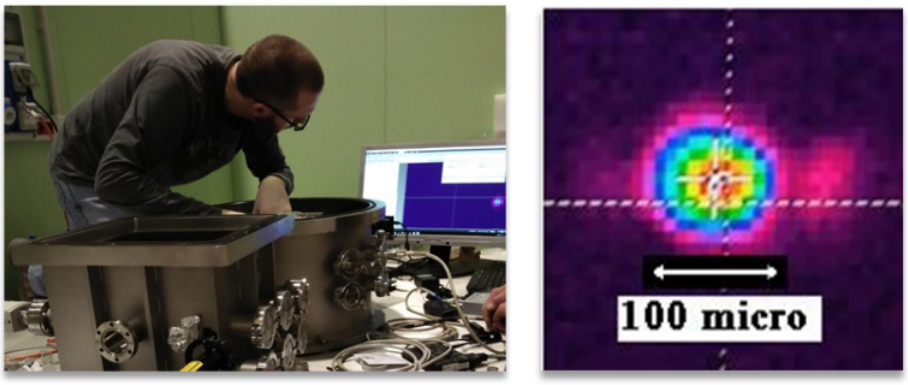

FIGURE 3.18: a) Fine-alignment of the optical elements of the instrument. b) Profile of the beam at the exit of the monochromator in the focal plane.

after the refocusing mirror. The HH spectrum generated in Neon with $\simeq$ 400 μJ, 1030 nm driving pulses and 10 cm focusing lens is shown in Fig. 3.19 b). The use of Neon as interacting gas gives harmonics in the photon energy range 35 - 80 eV, with a peak emission in the H53-H55 interval and a cut-off at 73.45 eV (H61). Photon fluxes as high as 1.2 x 10^4 ph/pulse at 63.8 eV (H53) has been measured at the output of the monochromator, corresponding to $\simeq$ 5 x 10^8 ph/s at 50 KHz repetition rate, available on the target after the refocusing mirror.

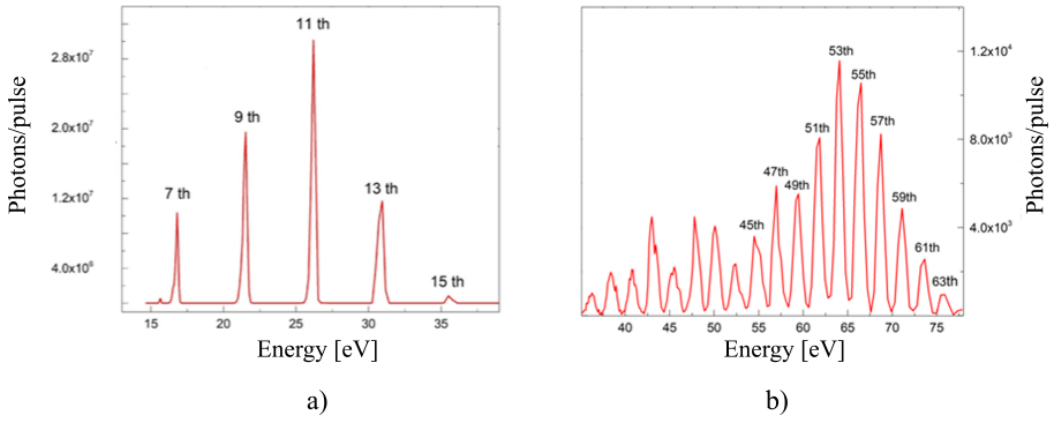

FIGURE 3.19: Typical HHG spectra in Argon and in Neon. a) Harmonics generated in Argon with $\simeq$200 μJ, 515-nm driving pulses b) Harmonics generated in Neon with $\simeq$ 400 μJ, 1030-nm driving pulses.

The reported spectra confirms the capability to resolve adjacent harmonics separated by 2.4 eV, when XUV is generated using a 1030 nm driving laser. The actual energy bandwidth on the target is limited by the intrinsic bandwidth of the HHs, which is evaluated to be in the 15-20 meV range. The temporal response of the monochromator is limited by the pulse-front tilt, that depends on the number of illuminated grooves and therefore on the XUV beam divergence. The latter has been

measured by a knife-edge technique to be 10 mrad for H11 in the plateau region and 7.5 mrad for H15 in the cut-off. The corresponding pulse-front tilts are in accord with those calculated and presented in the previous section. The front-tilts are lower than the duration of HHs, that is roughly estimated to be $\simeq$ 150 fs when 515 nm seeding is used (this corresponds to half the duration of the laser fundamental pulses). The XUV beam at the exit of the monochromator is focused on the sample placed in the experimental apparatus by the toroidal mirrors hosted in the refocusing chambers. The latter have been finely aligned with visible radiation, as well. The measure of the profile of the XUV focal spot has been accomplished using a YAG crystal placed into the center of the ULTRASPIN ARPES set-up experimental chamber. The fluorescence emitted by the YAG and induced by the harmonic is imaged on a CCD camera. In Fig. 3.20 a) the XUV focal spot on the YAG crystal of a harmonic in the plateau is shown. The horizontal profile of the XUV spot is fitted by Gaussian function and the corresponding FWHM is 185 μm, as reported in Fig. 3.20 b).

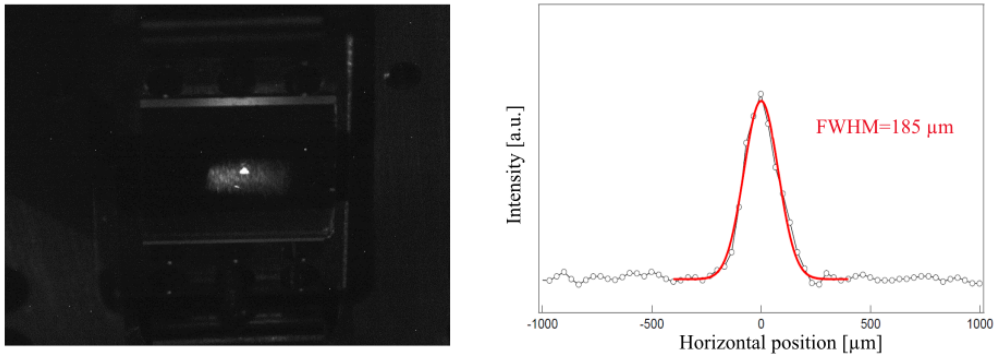

FIGURE 3.20: XUV focal spot. a) CCD image of the fluorescence emitted by the YAG crystal. b) Measured focal spot horizontal profile (FWHM =185 μm).

3.3.3 Experimental results

The first photoemission spectra using the HH beamline have been obtained using a gold sample at room temperature (T=300 K). The beamline has been operated at a repetition rate of 5 kHz using the second harmonic of the fundamental, with an energy of the driving laser equal to 400 μJ per pulse. The photon flux of the XUV beam after the refocusing chamber has been estimated to be 3 x 10^7 ph/pulse at 26.5 eV (H11) and the spot size area at the sample has been evaluated to be 185 μm x 250 μm. The monochromator silts have been opened at 100 μm. In Fig. 3.21 a) the Au photoemission spectrum obtained using the HH9 is shown. The spectrum has been recorded in a relatively short time (30 minutes). In Fig. 3.21 b) a comparison between the photoemission spectra around the Fermi edge acquired using respectively the HH source and a Helium-lamp is reported. The spectrum measured using the HH beamline as a source is in good agreement with the data acquired using the lamp.

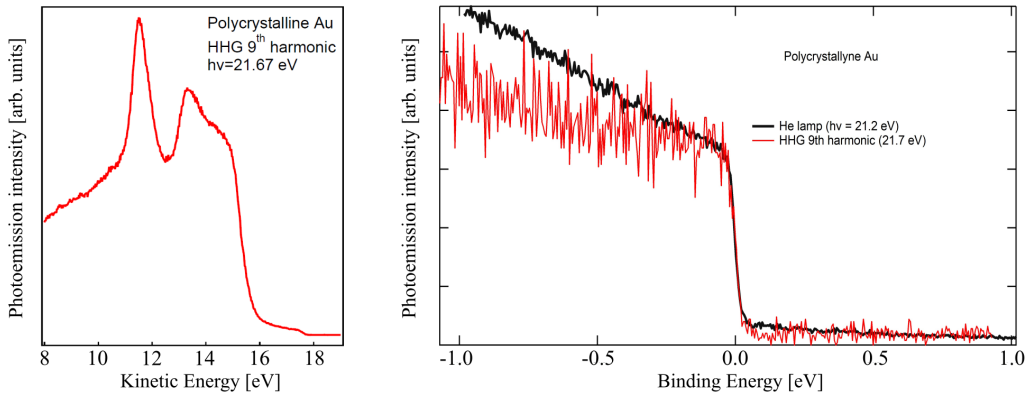

FIGURE 3.21: Photoemission spectra of Au at room temperature. a) Photoemission spectrum obtained using the HH beamline and selecting the HH11 (20.15 eV). b) A comparison between the photoemission spectra around the Fermi edge acquired using respectively the HH source and a Helium-lamp.

The effects of space charge on the measurements, due to the high peak photon flux, were also evaluated observing the features of the photoemission spectrum of the gold sample. First of all, to assess these effects, the position of the gas-cell has been detuned, in order to reduce the photon flux on the sample. The photoemission spectra obtained varying the position of the gas-cell are shown in Fig. 3.22 a). The spectrum acquired in the optimal position of the cell (the one that gives a higher photon flux at the output) presents more broadenings and positive shifts of the features respect to the spectra acquired in different positions. Moreover, the evaluation of the space charge effects has been continued by increasing the repetition rate of the driving laser, with a consequent reduction of the peak photon flux. The photoemission spectra obtained increasing the repetition rate of the driving laser are shown in Fig. 3.22 b). The 10 KHz spectrum, in contrast to the spectrum acquired at 5 KHz, presents less broadening and positive shifts of the features because the energy per pulse is decreasing by a factor 2. Permanence of space charge related effects, suggests that a lot of room for improvement is available at larger repetition rates. As also mentioned, these are only few of the many possible strategies that can be used to minimize this undesired effect.

First ARPES measurements have been also performed on a freshly-cleaved, high-quality single-crystal of Bi2Se3, known to be a topological insulator. The measurement is reported in Fig. 3.23. The sample was at room temperature (T=300 K), and the photon energy has been set at the harmonic HH7 ($\approx$ 16.85 eV). The acquisition time was $\approx$ 15 min. The ARPES map clearly evidences the topological surface state and the bulk conduction band.

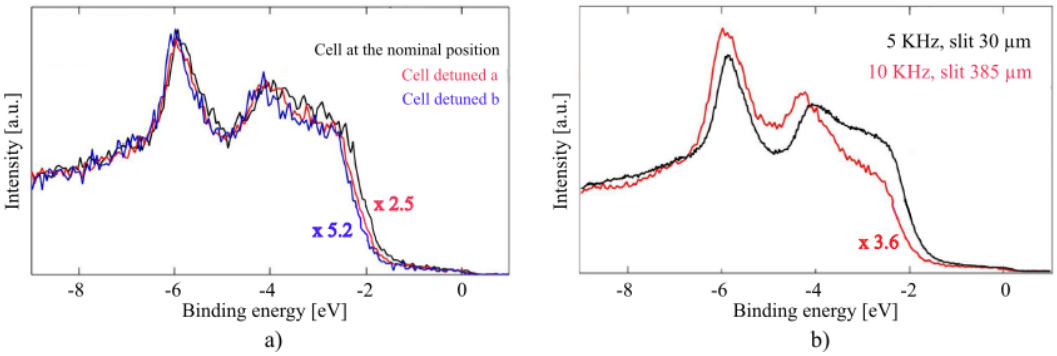

FIGURE 3.22: Photoemission spectra of Au at room temperature for the evaluation of space charge effects. a) Photoemission spectra obtained detuning the position of the gas-cell. b) Photoemission spectra obtained increasing the repetition rate of the laser.

3.4 Comparison between the two beamlines

The main difference between the beamline located in Nanjing and the beamline located in Trieste is the repetition rate of the driving laser. Typically, Ti:Sapphire lasers can provide high photon numbers per pulse at relatively low repetition rates (typically 10 Hz up to a few kHz). This is well suitable for experiments in gas phase, since the low density of the sample under test requires a number of interacting photons as high as possible to obtain a corresponding high number of generated secondary electrons. However, applications on solid targets require a lower number of interacting photons per pulse to minimize space charge effects, which induce broadenings and shifts of the photoelectrons spectra structures, with a consequent loss in energy resolution. Moreover, a high repetition rate is desirable to reduce the acquisition time. Since less XUV photons per pulse are required on the source side, the energy per pulse of the primary laser could be reduced and correspondingly the repetition rate could be increased. The beamline in Nanjing uses a standard Ti:Sa laser with 1 kHz repetition rate and up to 4 mJ per pulse. When 1.5 mJ is used to generate HHs, a strong space charge is observed on the static ARPES spectra acquired from the sample since the XUV photon flux is too high. Therefore either the pulse energy used to generate harmonics or the gas pressure on the cell have to be reduced to limit the XUV photon flux on the sample. Finally, the acquisition time is limited by the repetition rate of the laser. Novel laser technologies, employing Yb based materials allows to generate high repetition rate and femtosecond duration pulses with low energy per pulse with average output power even exceeding 1 KW. Using this type of laser, not only the repetition rate can be increased with respect to standard Ti:Sapphire systems but also the average photon flux of HH sources becomes higher by few orders of magnitude, being comparable to the flux available from a synchrotron ring. In addition, being the available energy per pulse lower, the number of XUV photons per pulse is reduced and the space-charge effect is mitigated. Therefore, techniques

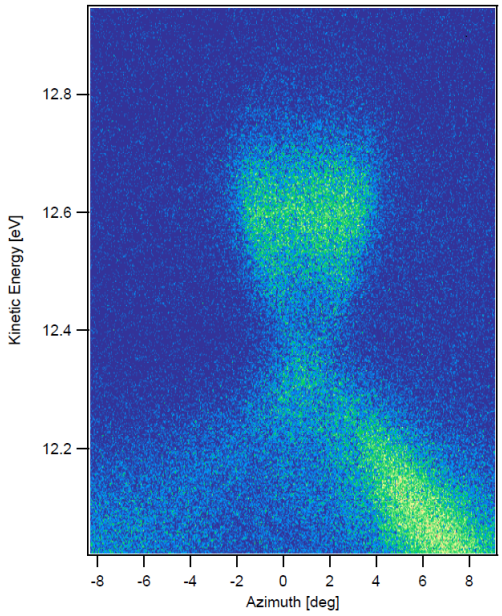

FIGURE 3.23: ARPES snapshots of Bi2Se3 at room temperature band structure, obtained using the HH beamline and selecting the HH7 (16.85 eV).

such as photo-emission spectroscopy from solid targets could take several advantages from these powerful and coherent short wavelength sources. The beamline located at Trieste employs an Yb:KGW laser with low energy per pulse (400 μJ/pulse) in order to reach repetition rates up to 100 KHz with high average power. Being the energy per pulse lower, a short focal length has to be used to generate harmonics, since this regime requires tight focusing of the moderate peak power driving pulses. In fact, in the beamline located at Trieste the generation is achieved using a 10 cm focal length lens, while in the beamline located in Nanjing harmonics in Argon and in Neon are generated respectively using a 50 cm and 30 cm focal length lenses. The temporal response of both beamlines is limited by the XUV response of the monochromator and by the duration of the generating laser. The temporal resolution of the beamline in Nanjing is in the range 40-100 fs, the lower limit being fixed by the laser duration, while the beamline in Trieste is used for longer dynamic effects, in the range 100-200 fs. The main differences can be finally resumed as follows, being both sources focused on TR-ARPES experiments:

- The beamline in Nanjing uses the conventional approach with a standard Ti:Sa laser limited to a relatively low repetition rate and aims to study dynamic effects shorter than 100 fs. The acquisition time for the experiment is limited by the low repetition rate and by the reduced XUV photons available per pulse to avoid the space charge effect

- The beamline in Trieste uses a fiber-based laser at high repetition rate and low energy per pulse, to avoid space charge effects and reduce the acquisition time

for the experiment by at least one order of magnitude, although for dynamics longer than 100 fs.

3.5 Conclusions

The design, the installation and the characterization of two HH beamlines for TR-ARPES experiments have been presented. HH spectra in the XUV/soft X-ray domain, using Argon and Neon as interacting gas, have been successfully and reproducibly acquired. The characterization has proved that the two setups fulfill all the desired specifications in terms of spectral and temporal resolutions. Moreover, first experimental results (e.g. photoemission spectra from solid targets) have shown that the beamlines are nearly at their full capacities. These sources will enable pump and probe experiments with femtosecond resolution with the aim of using novel spectroscopy techniques to gain insight into ultrafast phenomena. Low repetition rate HH beamlines, such as the one located at Nanjing, allow the generation of soft X-ray/XUV radiation suitable for Time Resolved analysis of ultrafast phenomena in gas samples. On the other hand, high repetition rate HH beamlines like the one located at Trieste are specifically conceived for Time Resolved experiments on solid targets, since their design allow to limit space charge effects which induce a loss in energy resolution. It is worth mentioning that the repetition rate at which the Trieste source is operating (50 KHz) constitutes an improvement of almost one order of magnitude compared to the repetition rate of the most common HHG sources. These high repetition rate beamlines are nowadays producing intense and coherent ultrashort soft X-ray/XUV radiation suitable for a wide range of time resolved spectroscopy techniques and are becoming the future trend for the designing of HH beamline.

Chapter 4

Grating compressor for extreme-ultraviolet chirped ultrafast pulses

The CPA scheme on seeded FELs tested at the FERMI FEL, using a XUV grating compressor specifically designed for the purpose, is presented in this chapter. The development and the characterization of the instrument are reported respectively in sections 4.1 and 4.2. The overview of the experiments regarding the CPA technique on seeded FELs, performed at FERMI in the last years, is presented in section 4.3.

4.1 Development of a XUV grating compressor for CPA experiments in seeded FELs

The grazing-incidence grating compressor realized for CPA experiments in seeded FELs consists of two identical CDM plane gratings having constant grooves spacing, mounted in the compensated configuration and operated in parallel light, as shown in Fig. 4.1. The first grating (G1) diffracts the light and introduces different optical paths for different wavelengths. The pulse-front tilt after the first diffraction is tilted and has to be corrected by a second grating (G2). The compensation is realized by a scheme with the gratings mounted with opposite diffraction orders. The first grating is mounted in the so-called anti-blaze configuration ($\alpha < \beta$, first external order) and the second one in the blaze configuration ($\alpha > \beta$, first internal order). In such a way, the incidence angle on G2, $\alpha_2(\lambda)$, is equal to the diffraction angle from G1, $\beta_1(\lambda)$, and the diffraction angle from G2, $\beta_1(\lambda)$, is constant with the wavelength and equal to the incidence angle on G1, $\beta_2 = \alpha_1$. Therefore, the output rays are parallel to the input for all the wavelengths. From the point of view of the ray paths, the differences in the path lengths of rays with the same wavelength but with different entrance directions within the beam aperture that are caused by G1 are compensated by G2, e.g., all the rays with the same wavelength make the same optical path. In addition, G2 compensates for the spectral dispersion caused by G1, i.e., all the rays at different wavelengths within the pulse spectrum exit the second grating with parallel directions. Aim of the compressor is to introduce a suitable

Group Delay Dispersion (GDD), that is the variation of the propagation time of the rays with different wavelengths.

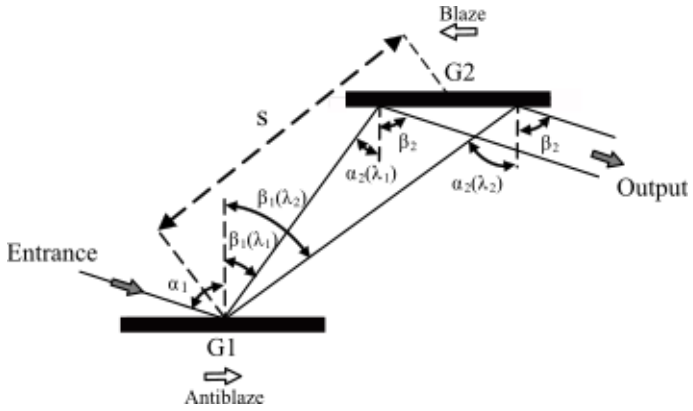

FIGURE 4.1: Schematic layout of a basic grating compressor.

The phase chirp introduced by the system is calculated as the difference in the optical path between rays at different wavelengths. The optical path as a function of the wavelength is expressed, for less than a constant term, as

$$OP(\lambda) = s\frac{cos\beta_c}{cos\beta}(1 - sin\alpha sin\beta) \tag{4.1}$$

where s is the grating-to-grating distance, α is the incidence angle on G1, β is the diffraction angle from G1 at a generic wavelength and β_c is the diffraction angle from G1 at the central wavelength of operation λ_c. In case of a narrow-band pulse with $\Delta\omega/\omega = \Delta\lambda/\lambda < 10\%$, such as is the case for FELs, the optical path is increasing linearly with the wavelength and the Group Delay Dispersion (GDD) is constant and defined as:

$$GDD = -\frac{s\lambda_c^3\sigma^2}{2\pi c^2 cos^2\beta_c} \tag{4.2}$$

where, σ is the groove density of the grating and c is the speed of light in vacuum. As also mentioned, G1 is normally operated in the anti-blaze configuration, i.e., $\beta > \alpha$ and $cos\beta < cos\alpha$ since this gives a shorter distance s once the required GDD has been fixed, and therefore a more compact compressor. The grating rotation is chosen as:

$$\alpha = \frac{K}{2} - arcsin[\frac{\lambda_c\sigma}{2cos(K/2)}] \tag{4.3}$$

and the diffraction angle is:

$$\beta_c = K - \alpha = \frac{K}{2} + arcsin[\frac{\lambda_c\sigma}{2cos(K/2)}] \tag{4.4}$$

where K is the subtended angle. Once the FEL wavelength has been fixed, the GDD is tuned by choosing the proper subtended angle. The schematic layout of the

optical configuration realized for the XUV grating compressor for CPA experiments is shown in Fig. 4.2. The instrument consists of four optical elements: two CDM gratings (G1 and G2) and two plane mirrors (M1 and M2). As illustrated above, the control of the optical delay between different spectral components of the FEL radiation is performed through the variation of the FEL incident angles on the gratings. The latter can be varied independently. The mirrors are employed to steer the beam back to its original propagation axis.

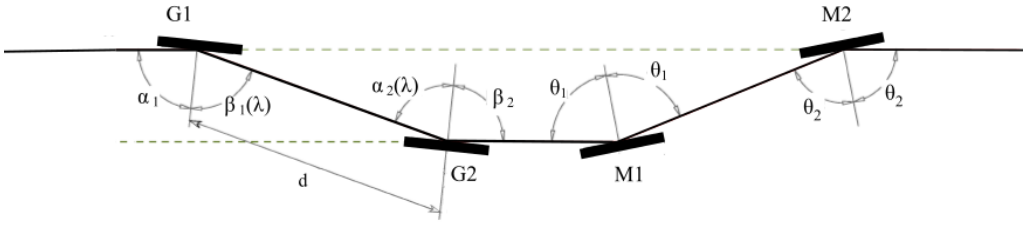

FIGURE 4.2: Schematic layout of the optical configuration realized for the XUV grating compressor for CPA experiments.

Depending on the working spectral range, couples of saw-tooth profile gratings having different groove densities and blaze angles can be adopted. In particular, for the CPA experiments described in the next sections two couples of gratings have been used: the first one, having 600 gr/mm density and a 2° blaze angle gratings, operates in the 20 - 40 nm range; while the second one, having 1200 gr/mm density and a 4.128° blaze angle gratings, operates in the 8 - 20 nm range. The optical parameters of the compressor are resumed in Tab. 4.1.

As also mentioned, the compressor is tunable in wavelength and time delay by changing the subtended angle K. For instance, in Fig. 4.3 the variation of the group delay introduced by the compressor using the 600 gr/mm gratings within a pulse bandwidth of 0.125 nm at different subtended angles and for different wavelengths is shown. The choice of the included angle makes the instrument very flexible, being able to introduce variable delays in a wide spectral range.

Careful considerations should be given to the compensation of the wave-front tilt due to the divergence of the FEL beam. If the beam is divergent and the gratings are parallel, the second grating is illuminated in a larger area than the first one. The illumination of a higher number of grooves on the second grating gives an undesired pulse-front tilt. This effect can be avoided positioning the second grating not parallel to the first one. Obviously, the difference between the two subtended angles will depend on the divergence of the FEL beam. This difference is generally expected to be quite small (i.e., fractions of degrees). The described adjustment avoids the use of a pre-collimating optical element, incrementing the instrumental throughput and simplifying the optical design of the compressor. The optics of the compressor are hosted in an ultra high-vacuum chamber, shown in Fig 4.4 a). Each of the optical elements is mounted on a roto-translation stage moved by external stepper motors. The translations of G1 and M2 are used to remove the optical elements from the light

TABLE 4.1: Compressor parameters

Gratings [configuration 1]	
Range	20 - 40 nm
Groove density	600 gr/mm
Blaze angle	2°
Ruled area	80 mm × 20 mm
Coating	Gold
Gratings [configuration 2]	
Range	10 - 20 nm
Groove density	1200 gr/mm
Blaze angle	4.128°
Ruled area	70 mm × 25 mm
Coating	Gold
Mirrors	
Reflecting area	140 mm × 20 mm
Coating	Gold
Distances	
G1-G2	0.4 m
G2-M1	0.14 m
M1-M2	0.48 - 0.50 m
G1-M2	1 m
Motorized movements	
G1	
Included angle	156° − 166°
Translation	20 - 30 mm
G2	
Included angle	156° − 166°
Translation	40 mm
M1	
Included angle	156° − 166°
Translation	40 mm
M2	
Included angle	168° − 173°
Translation	20 - 30 mm

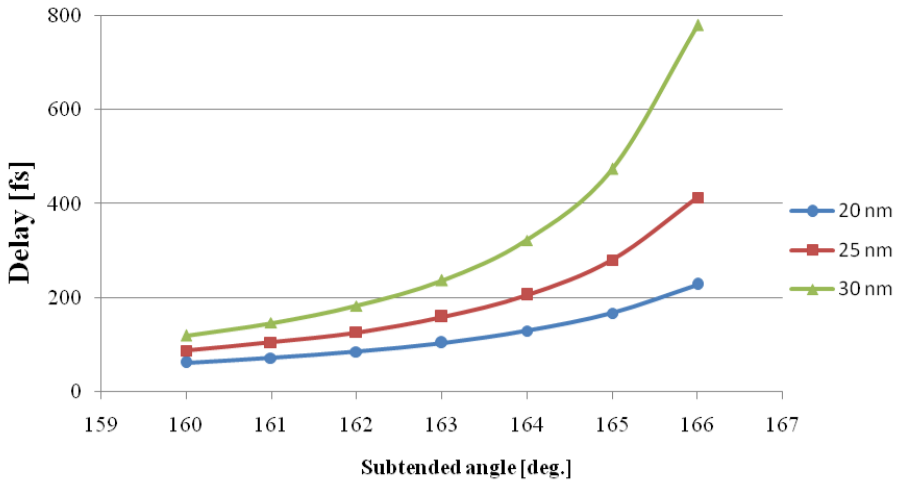

FIGURE 4.3: Variation of the group delay introduced by the compressor using the 600 gr/mm gratings within a pulse bandwidth of 0.125 nm at different subtended angles and for different wavelengths.

path and let the FEL beam propagate. The rotation of G1 and rotation/translation of G2 are used to tune the compressor and to change the subtended angles on the two gratings. The rotations of the gratings can be varied independently to compensate the front tilt due to the divergence of the FEL beam. The angular resolution of the rotation stage is 65.8 μrad/step in a full step mode; controllers have a 1/8-step resolution. The incident angles of the gratings can be selected in the range $-0.5°/14.5°$. The use of the mirrors M1 and M2 achieve the FEL output beam to be sent on the original optical path. The design of the instrument is quite compact, with an envelope that is less than 1.5 m. The compressor chamber, now installed at FERMI is shown in Fig. 4.4 b).

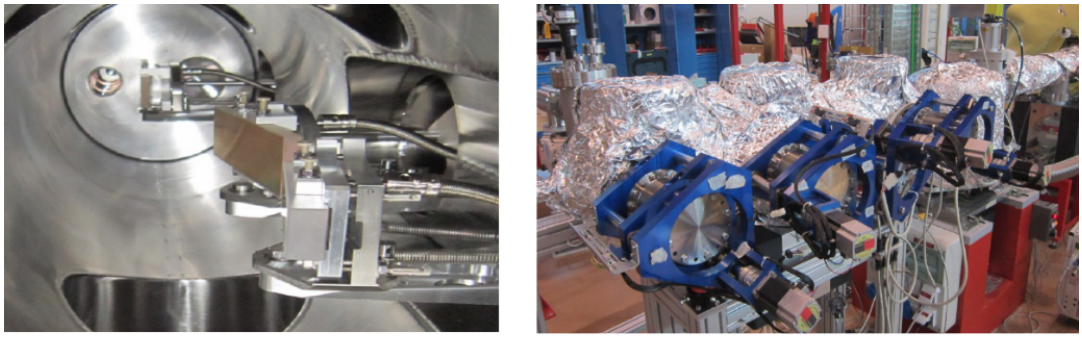

a) b)

FIGURE 4.4: a) Optical elements of the compressor mounted in supports moved by external stepper motors. b) The compressor chamber, now installed at FERMI.

4.2 Gratings characterization

The throughput of the compressor is predominantly determined by the gratings efficiencies. Blazed saw-tooth profile gratings have been chosen for the realization of the instrument, since they gives high peak efficiency at the blazed wavelengths. As also mentioned, couple of gratings having different groove densities and blaze angles have been adopted, depending on the working wavelength range of the experiments. The diffraction efficiencies of two gratings used in a first experiment regarding the CPA on seeded FELs, and described in the next section, have been measured at the facility available at CNR-IFN Padova [71]. These gratings are plane, gold coated, with 600 gr/mm line density and 2° blaze angle, commercially available from Newport – Richardson Gratings (USA). The gratings have been inserted in the experimental chamber of the facility and the diffracted radiation has been acquired with a Channel Electron Multiplier (CEM) detector. A hollow cathode lamp has been used as light source. The emitted radiation is almost unpolarized. The spectral range covered by the facility is 25 - 45 nm, therefore the measurements here presented cover the upper wavelength interval of operation of the instrument. The selection of the lines of interest has been achieved by a spherical grating monochromator. The monochromatized light has been focused on the grating under test through a toroidal mirror. Gratings have been mounted in the chamber with their blaze arrows in opposite direction, i.e., the first one has its blaze arrow pointing to the detector, the second one has its blaze arrow pointing to the source. The efficiencies at the first order have been measured in the blaze (i.e., diffraction angle lower than incidence angle) and in anti-blaze (i.e., diffraction angle higher than incidence angle) geometries at different subtended angles. The measurements are shown in Fig. 4.5. There are no significant differences in the efficiencies measured in the blaze and in the anti-blaze configurations.

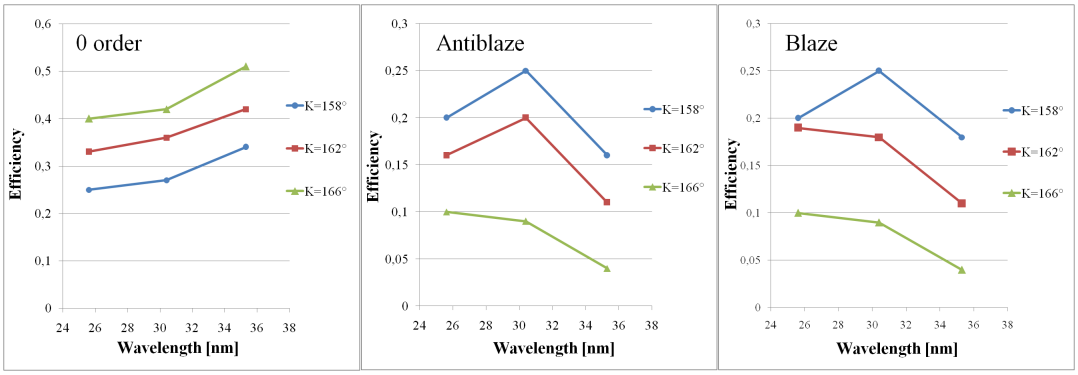

FIGURE 4.5: 600 gr/mm gratings efficiencies at the first orders measured in the blaze and in anti-blaze at different subtended angles for almost unpolarized radiation.

The overall efficiency of the double grating compressor can be calculated taking into account also the reflectivity of the two gold-coated mirrors. The throughput of the instrument in this configuration is between 1%-6 % in the whole spectral range of operation. The diffraction efficiencies of other two gratings to be used for a second experiment regarding CPA on seeded FELs and described in the next section have been measured at the facility available at the Circular Polarization (CiPo) beamline at Elettra, Trieste [72]. These gratings are plane, gold-coated, with 1200 gr/mm line density and 4.128° blaze angle, commercially available from Newport. The surface morphology of the diffraction gratings have been analyzed by atomic force microscopy (AFM) using a facility available at CNR-IFN Padova [73]. The scans have been performed by using the AFM operating in non–contact mode. A reference sample has been used to calibrate the height scaling of the instrument and to optimize the AFM scanning parameters. This step is pivotal for the accurate characterization of the gratings. An AFM image of one of the grating, having a 10 μm x 10 μm scan size and acquired at 0.5 Hz scan rate is shown in Figure 4.6. The groove profiles of the gratings are well defined, along with portions of the profile that are rougher than others. The measured parameters (grooves height and grooves period) are in acceptable agreement with the nominal specifications of the grating.

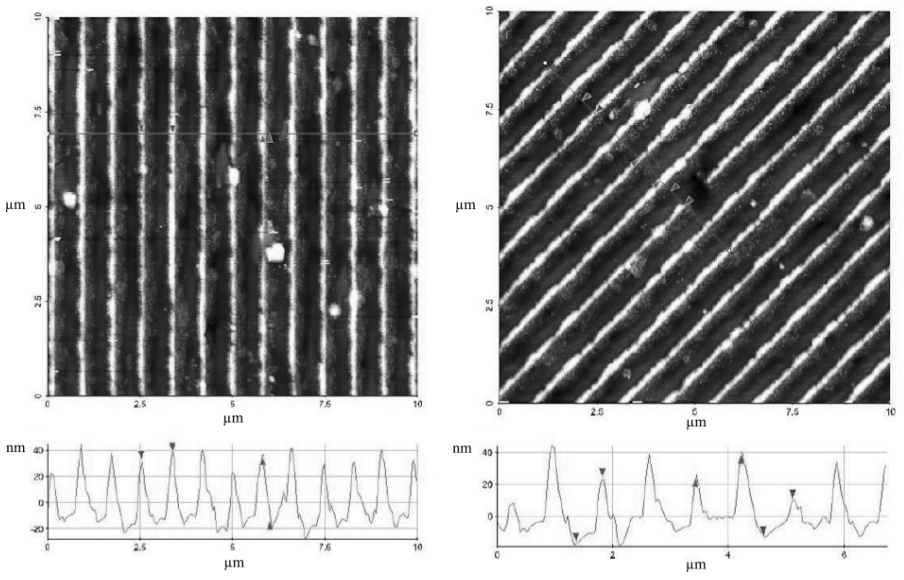

FIGURE 4.6: AFM imaging of two portion of the 1200 gr/mm blazed profile grating. a) AFM topography with image size 10 μm x 10 μm; b) AFM topography with image size 2 μm x 2 μm.

The CiPo beamline provides synchrotron radiation beam of variable polarization (Circular to Linear) in a very broad range of photon wavelengths, from 248 to 1.4 nm. The photon beam is produced by an Electromagnetic Elliptical Wiggler and is dispersed by means of two collinear monochromators, a Normal Incidence Monochromator (NIM) and a Spherical Grating Monochromator (SGM), that alternatively provide two beams in the UV-XUV (248 - 31 nm) and soft X-rays (31 - 1.4

nm) respectively. The gratings to be tested have been mounted on a reflectometer realized by CNR-IFN Padova that has been installed at the output of the beamline. The sample is mounted on motorized stages to select the measurement geometry (e.g., reflectivity, diffraction efficiency, transmission). The radiation is detected through a Channel Electron Multiplier (CEM). The synchrotron emission is p-polarized. The efficiency curves of the external orders, i.e., $\alpha < \beta$, measured in the anti-blaze condition at different incidence angles are shown in Figure 4.7. The efficiency curves of the internal orders, i.e., $\alpha > \beta$, measured in the blaze condition at different incidence angles are shown in Figure 4.8. The measured values are in slight disagreement with the simulated ideal saw-tooth profile grating's efficiencies obtained with a code using the grating EM theory and also plotted in Figure 4.9 and Figure 4.10; This may be justified with a clear mismatch between the ideal saw-tooth blazed profile and the real structure of the grating revealed by the AFM analysis. The throughput of the instrument in this configuration has been calculated to be between 0,5%-2% in the whole spectral range of operation.

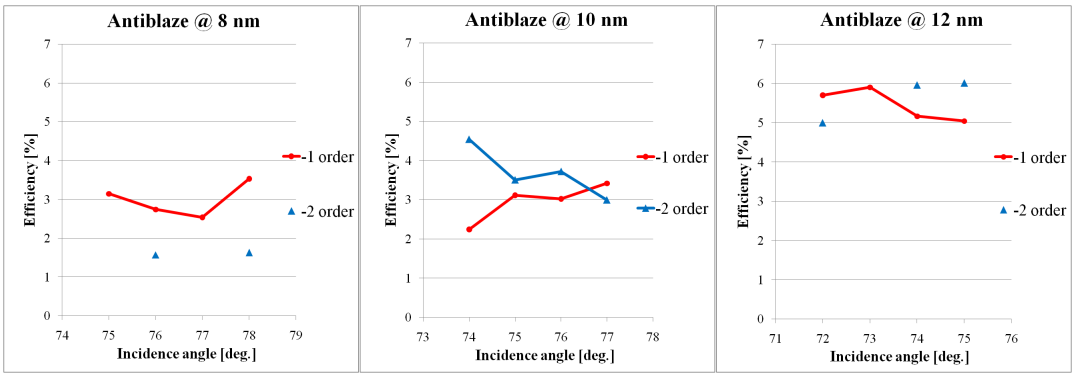

FIGURE 4.7: 1200 gr/mm gratings measured p-polarization efficiency curves of the external orders measured in the antiblaze condition at different incidence angles.

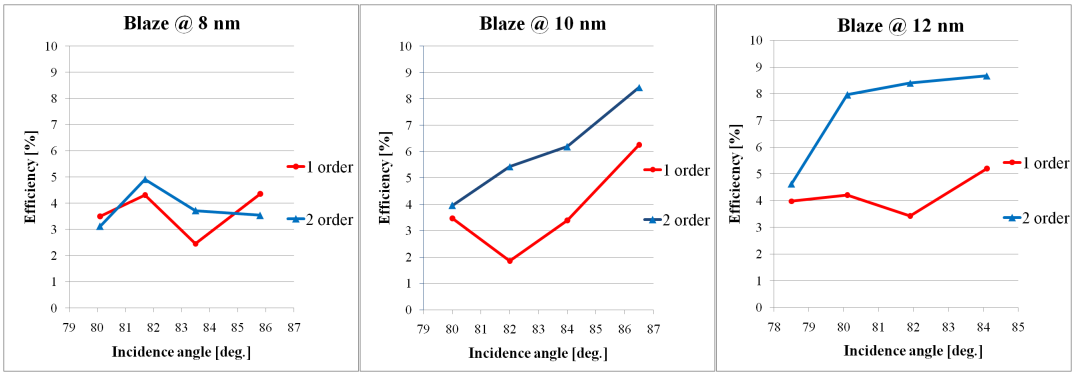

FIGURE 4.8: 1200 gr/mm gratings p-polarization efficiency curves of the internal orders measured in the blaze condition at different incidence angles.

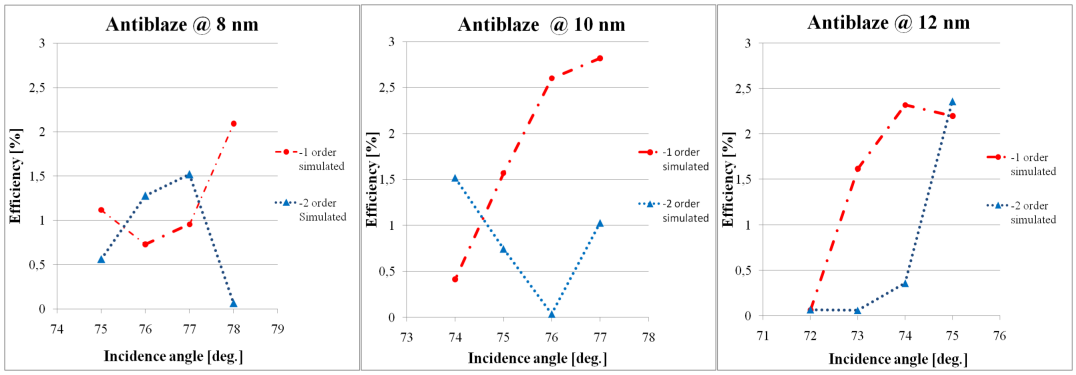

FIGURE 4.9: 1200 gr/mm gratings simulated p-polarization efficiency curves of the external orders in the antiblaze condition at different incidence angles.

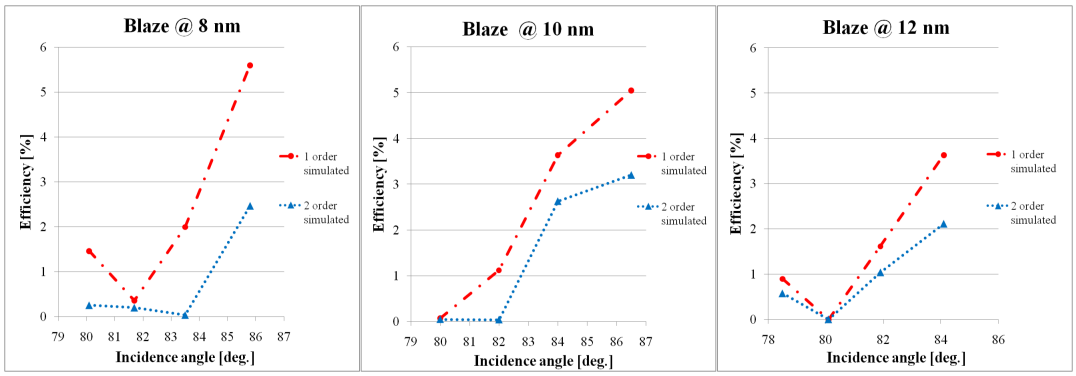

FIGURE 4.10: 1200 gr/mm gratings simulated p-polarization efficiency curves of the internal orders in the blaze condition at different incidence angles.

4.3 Experimental results at FERMI

The experiments carried out at FERMI were aimed at demonstrating the feasibility of the CPA scheme for seeded FELs. As also mentioned, this technique gives the possibility of introducing, under proper conditions and in a controlled way, a linear frequency chirp from the seed to the FEL pulse, and then of recompressing it by using an optical compressor. In the experiments that will be described in this section the grating compressor outlined in section 4.1 has been employed for the compression of the FEL pulse. A first experiment has been performed in April 2015 [8], in order to assess the CPA technique on seeded FELs using the grating compressor. The setup of the experiment is schematically shown in Fig. 4.11.

The seed for the FEL was given by the third harmonic of a Ti:Sapphire laser (λ_{seed} =261 nm, with a gaussian profile). The seed-pulse before stretching had a FWHM duration of 170 fs and a FWHM bandwidth of 0.7 nm. The FEL has been tuned at 37.3 nm. The FEL pulse duration was measured using a cross-correlation scheme [74], based on the photo ionization of He by the FEL pulse assisted by an

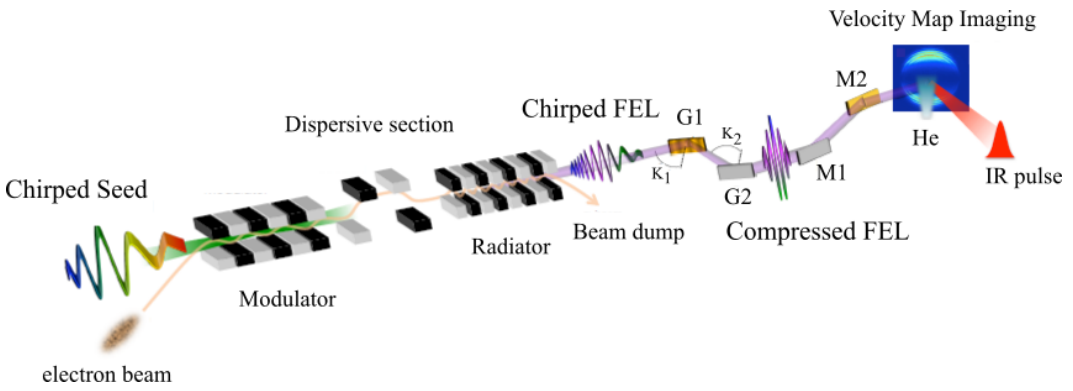

FIGURE 4.11: The setup of the CPA experiment.

intense infrared (IR) laser with a variable time-delay and a known pulse duration (90 fs FWHM). The images of the photo-electron distribution are acquired with a Velocity Map Imaging spectrometer (VMI). Inverting the VMI image and integrating over the angular dependence of the electron emission, the photo-electron energy spectrum can be obtained. It consists of a main peak, associated to the direct photoemission process, and of sidebands that results in the interaction with the variable delayed IR. The cross-correlation curves associated to the sidebands, from which the FEL pulse profile can be deconvolved, are obtained by integrating the electron signal over all emission angles and plotting the area under the corresponding peaks as a function of the FEL-IR delay. First of all, the FEL spectrum and pulse duration have been measured in the normal working conditions, i.e., no stretching of the seed, and no FEL compression. The measured FWHM bandwidth and the pulse duration have been measured to be 0.038 nm and 91 fs, respectively. The corresponding time-bandwidth product is a factor of 1.7 above the transform limit. The measured pulse duration is in good agreement with the one calculated using the theory (see section 2.1.1), that is 89 fs. At this point, a positive linear frequency chirp in the seed pulse has been induced by propagating it through a calcium fluoride crystal, The stretched pulse had a duration of 290 fs FWHM. In these conditions, the FEL pulse has been characterized before and after the compression performed using the grating compressor. In Fig. 4.12 a) three measured single-shot spectral profiles of the FEL beam are shown. The average FWHM bandwidth is 0.046 nm. In Fig. 4.12 b) three measured cross-correlation curves, associated to the second sideband of the photo-electron spectrum for the non-compressed case are shown. In this case, the measured FWHM pulse duration is about 143 fs (see the red dotted curve), which is in good agreement with the theoretical expectation of about 152 fs. In Fig. 4.12 c) the same curves are presented for the case of maximum compression. Apparently, the increment of the FEL pulse bandwidth with respect to that of the unchirped seed allows to obtain, after compression, a significant shortening of the FEL pulse with respect to the no-CPA mode. The measured time duration of the pulse is about 50 fs (see the red dotted curve). The value is in discrete agreement to the one predicted by

the theory, that is about 40 fs. The CPA technique is therefore able to compensate not only the linear frequency chirp in the FEL pulse induced through the seed control, but also the unwanted residual generated by other sources [75].

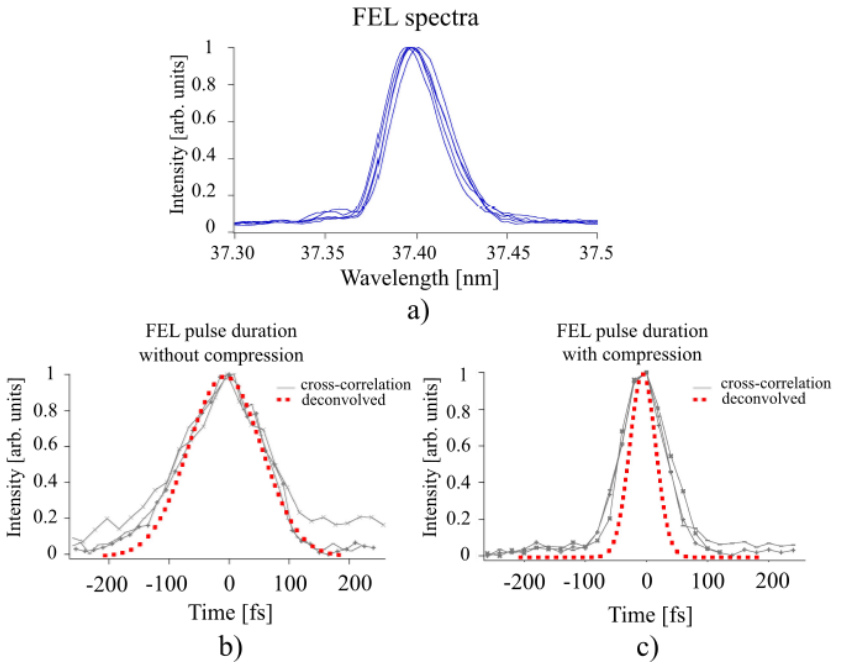

FIGURE 4.12: a) Normalized single-shot spectra of the FEL pulse generated after stretching of the seed pulse. b) Three cross-correlation curves associated to a sideband for three FEL-IR delay scans.. c) Same as b) for the FEL operated in CPA mode for maximum compression. The dotted curves represent the deconvolved FEL pulse.

The control of the optical delay between different FEL spectral components have been achieved through the variation of the FEL subtended angles on the gratings of the compressor. Once the required delay has been tuned positioning the gratings at the proper subtended angles (K_1=K_2= 162°) a fine tuning of the angles taken singularly has been then performed in order to compensate the pulse-front tilt due to the divergence of the FEL beam. The measured pulse duration as a function of the difference between the FEL incident angles on the two gratings is shown in Fig. 4.13. It is worth to be noted that the maximum compression has been obtained at a difference between the subtended angles of the gratings equals to 0.6°.

In September 2016 another CPA experiment has been carried out at FERMI. The experiment had the following purposes: to confirm the results obtained during the previous experiment and to generate shorter (< 30 fs) pulses. The experimental set-up was identical to the one of the experiment described above. Unfortunately, major issues with the FERMI accelerator, i.e., the failure of the RF cavity responsible of the linearization of electron-beam phase space happened and it hasn't been possible to generate shorter FEL pulses. However, the CPA effect - i.e., the possibility to stretch the seed laser, generate a chirped FEL pulse and re-compress it - has been confirmed

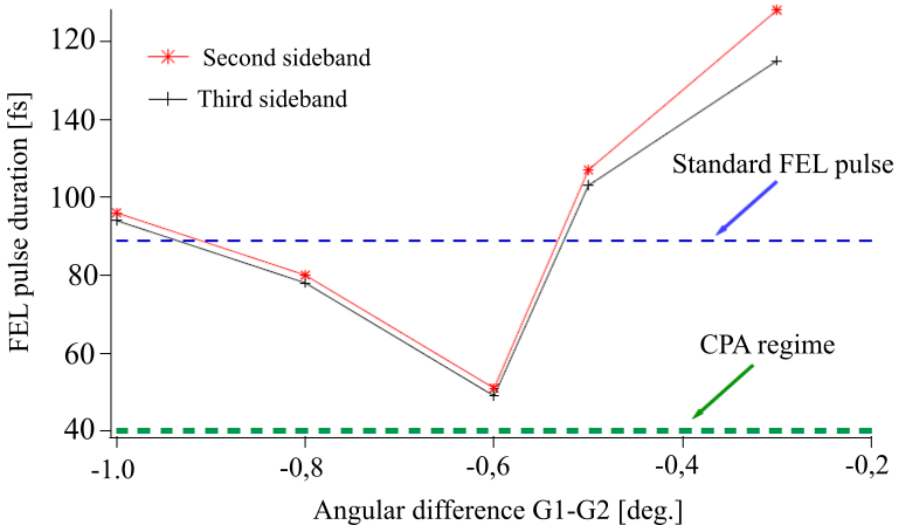

FIGURE 4.13: Measured pulse duration as a function of the difference between the incidence angles of the gratings of the compressor. The durations obtained from the second and the third sidebands of the photoelectron energy spectrum are reported. The horizontal dashed lines correspond to the theoretical pulse duration when the FEL is operated in standard or CPA regime.

again.

In September 2017 a further experiment has been performed at FERMI, in order to validate the CPA technique for shorter wavelengths. The seed for the FEL was given by the third harmonic of a Ti:Sapphire laser (λ_{seed} =261 nm, with a gaussian profile). The seed-pulse before stretching had a FWHM duration of 70 fs and a FWHM bandwidth of 1.8 nm. The FEL has been tuned at 17.6 nm. Because the pulse duration of the compressed FEL pulse was expected to be short, about 5-10 fs, it has been averted to measure it with a cross-correlation scheme as it has been done in the previous experiments, being the probe laser pulse 80-90 fs (therefore too large). The solution is the use of an auto-correlation technique. A transient grating technique has been used to perform an auto-correlation measurement of the FEL pulse duration [76]. In this technique the FEL pulse is split in two and focalized on a solid sample, while the second harmonic of the Ti:Sa laser is focalized on the sample and synchronized with the two FEL pulses. The autocorrelation curves are obtained by varying the delay between the two FEL pulses. Unfortunately, it wasn't possible measuring the FEL duration after the compression, due to the low flux at the output of the compressor and to the lack of the efficiency of the transient grating technique.

4.4 Conclusions

The development and the characterization of the XUV grating compressor installed at the FERMI seeded FEL at Elettra Sincrotrone Trieste have been described. The proper operation of the compressor has been demonstrated, since the Chirped Pulse

Amplification technique performed on the FERMI seeded FEL has been carried out with success in a first experiment at 37.3 nm. The technique achieved a relevant reduction of the FEL pulse duration with respect to that obtained in the standard operation mode. Moreover, a second experiment performed after some time confirmed the results obtained during the first run. A further investigation has been performed, in order to validate the CPA technique for shorter wavelengths, e.g. 17.6 nm. However, the experiment didn't provide a clear evidence of pulse compression because the sensitivity of the Transient Grating autocorrelation technique used to measure the pulse durations, coupled to the low transmission of the compressor, hasn't allowed to measure the FEL pulse duration after the compression. These are technical problems that, in principle, could be solved. The actual low transmission of the compressor around this wavelength (below 2 %) could be improved by adopting the off-plane mounting geometry for the gratings. This solution would enhance the efficiency of the compressor to a value around 10 %. This adjustment would make the instrument potentially interesting for CPA applications in the short wavelength domain. On the other hand, the instrument would become much more bulky, passing from a total envelope on the order of about two meters to an envelope of several meters. This would involve the redesigning of the mechanical components and the realization of two vacuum chambers, in order to install the gratings in two separated vessels. However, in a future perspective, the extension of the first obtained results could allow to generate fully-coherent femtosecond FEL pulses at wavelengths down to the water window.

Chapter 5

Soft X-ray Second Harmonic Generation in graphite

The observation of soft x-ray SHG generated by high intensity, coherent FEL pulses at FERMI FEL is presented in this chapter. The experiments were conducted at the EIS-TIMEX end station [77, 78] using a compact spectrometer conceived and realized by CNR-IFN Luxor and described in section 5.1. The experimental set-up and the results of the experiments are reported respectively in section 5.2 and in section 5.3. The intensity calibration of the spectrometer performed to evaluate the intensity of the SH photon flux after the sample is described in detail in section 5.4.

5.1 The spectrometer for photon in-photon out experiments

The optical design of the instrument consists of a couple of diffraction gratings working in grazing incidence and a detector. The gratings have a spherical shape with variable line spacing (VLS) along their surfaces, to provide a flat spectral focal plane that is almost perpendicular to the direction of the diffracted light [79]. The instrument is able to operate in the 25 - 800 eV spectral range. The 25 – 250 eV region is covered by a grating having a 1200 gr/mm central groove density (Hitachi cod. 001-0437), while the region 200 - 800 eV is covered by a grating having 2400 gr/mm central groove density (Hitachi cod. 001-0450). The gratings are mounted on a manual linear translation stage in order to perform the grating selection. The detector is a back-illuminated Charge-Coupled Device (CCD) camera (Princeton Instruments PIXIS XO 400B), having an array composed of 1340 X 400 pixels, with a 20 μm pixel size. Since the length of the focal plane of the 1200 gr/mm grating is longer than the array size, the detector is mounted on a PI miCos motorized linear translation stage connected to the gratings stage by a bellow. Therefore, it can be moved so that the desired energy can be acquired at the center of the detector plane. The instrument, which layout is shown in Fig. 5.1, is equipped with a variable entrance slit that can be manually adjusted from outside. It is independently pumped by a high-vacuum pumping system and shielded in order to maintain the pressure gradient between the instrument and the experimental chamber. A photograph of the instrument is shown in Fig. 5.2. The total envelope of the instrument is about 700 mm X 250 mm

X 250 mm. The main instrumental parameters of the spectrometer are summarized in Tab. 5.1. The calculated spectral extension of the spatial resolving element, which is the energy dispersion on the 20 μm detector pixel, is shown in Fig. 5.3 a). The efficiency of each element (the gratings, the detector), have been measured using the facilities available at CNR-IFN Padova. The total throughput of the instrument, in terms of counts per input photon, is shown in Fig. 5.3 b). The collected angle in the direction of the spectral dispersion is limited by the angular acceptance of the gratings. In the direction perpendicular to the dispersion, the collected angle is limited by the size of the array of pixels of the detector, whose area is 26.8 mm X 8 mm. These values are resumed in Tab. 5.2.

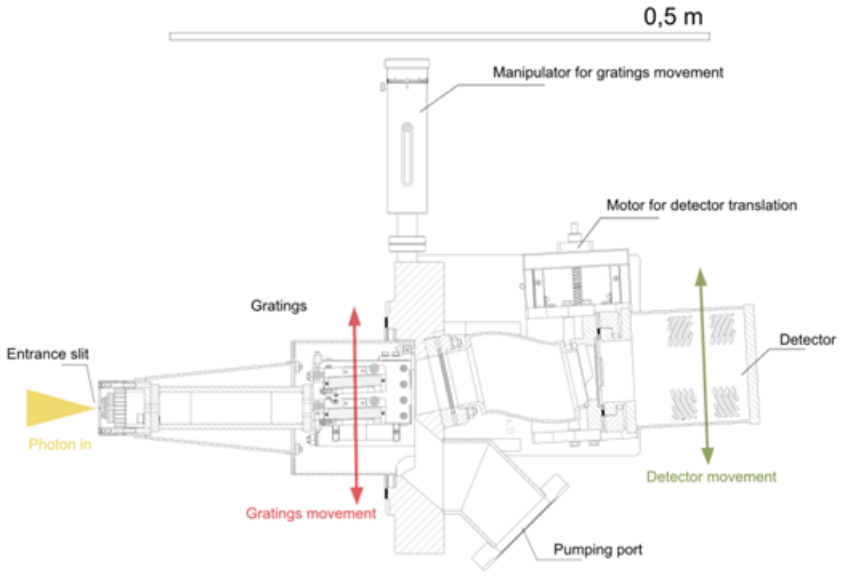

FIGURE 5.1: Layout of the spectrometer.

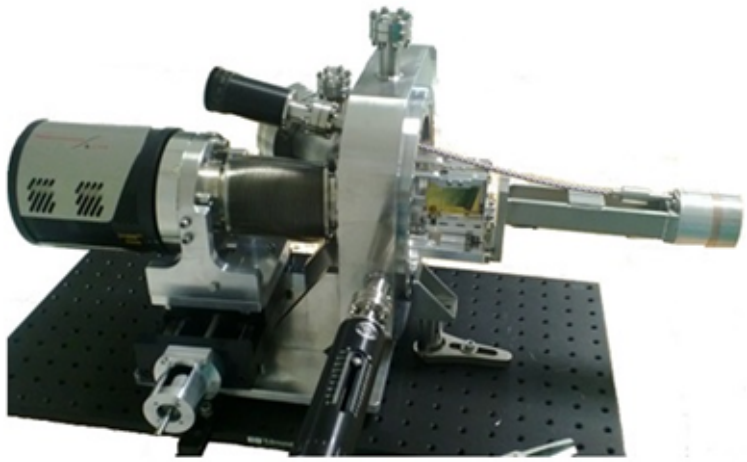

FIGURE 5.2: A photograph of the spectrometer.

TABLE 5.1: Instrumental parameters of the spectrometer

Grating G1200	
Groove density	1200 gr/mm
Energy	25 - 250 eV
Incidence angle	87°
Entrance arm	237 mm
Grating - detector distance	235 mm
Grating G2400	
Groove density	2400 gr/mm
Energy	180 - 800 eV
Incidence angle	88.7°
Entrance arm	237 mm
Grating - detector distance	235 mm
CCD detector	
Format	1340 $\times$ 400 μm
Pixel size	20 $\times$ 20 mm
Detector area	26.8 $\times$ 8 mm
Entrance slit + grating	
Entrance slit width	0.02 - 1 mm
Slit - Grating distance	237 mm

TABLE 5.2: Other instrumental parameters of the spectrometer

Detector spectral extension (long side, 26.8 mm)	
G1	25 - 50 eV
	40 - 112 eV
	60 - 250 eV
G2	180 - 800 eV
Detector spectral extension (short side, 8 mm)	
G1 (some examples)	25 - 30 eV
	40 - 51 eV
	100 - 160 eV
	140 - 250 eV
G2	180 - 270 eV
	330 - 600 eV
	400 - 800 eV
Acceptance angle, spectral dispersion plane	
G1200	10 mrad
G2400	5 mrad
Acceptance angle, plane $\perp$ spectral dispersion plane	
Detector short side $\perp$ to the dispersion	17 mrad
Detector long side $\perp$ to the dispersion	57 mrad

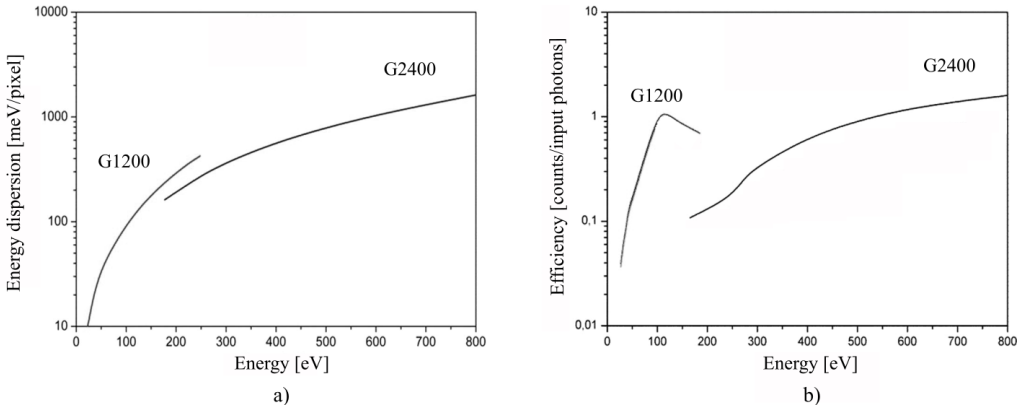

FIGURE 5.3: a) Spectral extension of the spatial resolving element, defined as the energy dispersion on the detector pixel. b) Total throughput of the instrument, defined as counts on the detector per input photon.

The instrument has been characterized at the Gas Phase beamline [80] of Elettra synchrotron, Trieste by measuring fluorescence spectra from solid and gas targets. Initially, the synchrotron beam at known energies has been directed toward the spectrometer in order to calibrate both the gratings (G1200 and G2400). The synchrotron bandwidth was narrower than the spectral extension of the CCD pixel. Sharp spectral lines have been acquired, about 3 pixels wide when using a 100 μm slit, confirming the good spectral focusing of the spectrometer. Furthermore, several spectra at different energies that confirm the dispersion curve presented in Fig. 5.3 a) have been measured. Although the signal had a relatively low photon flux, it has been acquired in 0.1 – 1 s. This confirms the good instrumental sensitivity. The characterization of the spectrometer as an instrument for photon in-photon out experiments has been initially performed by investigating fluorescence from solid samples. Measurements were performed on silicon, boron and boron nitride. A fluorescence spectrum of Si taken at the Si L edge is shown in Fig. 5.4 a). B and BN fluorescence spectra have been acquired at the B K edge and are shown in Fig. 5.4 b). The spectra are in overall agreement with previously published data [81, 82]. The spectrometer was characterized also measuring fluorescence from gas-phase targets. Fluorescence spectra from helium and krypton have been acquired. He spectra emitted when the exciting photon energy was fixed to the (3,0) resonance at 64.118 eV has been measured and is shown in Fig. 5.5 a). The emission lines observed using the spectrometer are in agreement with the data already available and the acquired spectra exhibit a higher signal-to-noise ratio than those reported in the literature [83]. Fluorescence emission from Kr has been also measured using an exciting photon energy on the Kr resonance at the 91.2 eV and is shown in Fig. 5.5 b).

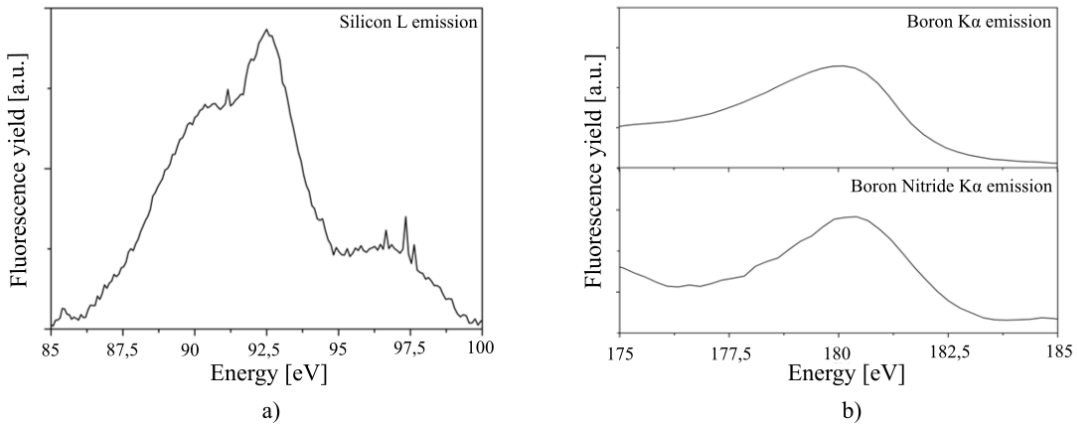

FIGURE 5.4: Fluorescence spectra from solids acquired using the spectrometer. a) Si L emission fluorescence spectrum for crystalline Si sample. The exciting photon energy is 100,5 eV. b) B and BN Kα emission fluorescence spectra. In case of B, the exciting photon energy is 220 eV. In case of BN, the exciting photon energy is 200 eV.

5.2 The SHG in graphite experiment

5.2.1 Experimental Set-up

A first SHG experiment has been conducted at the EIS-TIMEX end station [55]. The beamline is very flexible and can accommodate various possible configurations for single-shot experiments, such as XUV and Soft x-ray absorption/reflection and pump-probe experiments where the probe can be either an external laser or the FEL pulse. The experimental chamber of the end-station is equipped with a 5-axis motorized sample manipulator, which allows an accurate sample alignment. A long-distance microscope is employed for the fine alignment and the rough beam profile measurements. The main chamber is also equipped with a set of detectors for transmission and reflectivity measurements. The sample environment can be interfaced through a translation stage with a preparation chamber equipped for surface characterizations before one-shot experiments. Further instrumentation for the diagnostic of the transmitted beam can be installed after the experimental chamber. A schematic of the experimental set-up employed for the SHG in graphite experiment is shown in Fig. 5.6. A soft x-ray FEL pulse (having a pulse duration of 25 fs, a pulse energy of about 1–5 μJ, and a spot size of more or less 350 μm^2) is passed through a 2 mm diameter iris in order to attenuate the off-axis second harmonic contamination from the FEL source (the latter is more divergent than the fundamental) and focused onto the graphite samples placed in the center of the experimental chamber described above. Moreover, the FEL beam and the collinear SH signal are passed through a 600 nm aluminum filter to attenuate the fundamental pulse. The spectrometer is finally employed to acquire the signal, being able to spatially separate the SH from the fundamental. The instrument has been installed in a dedicate

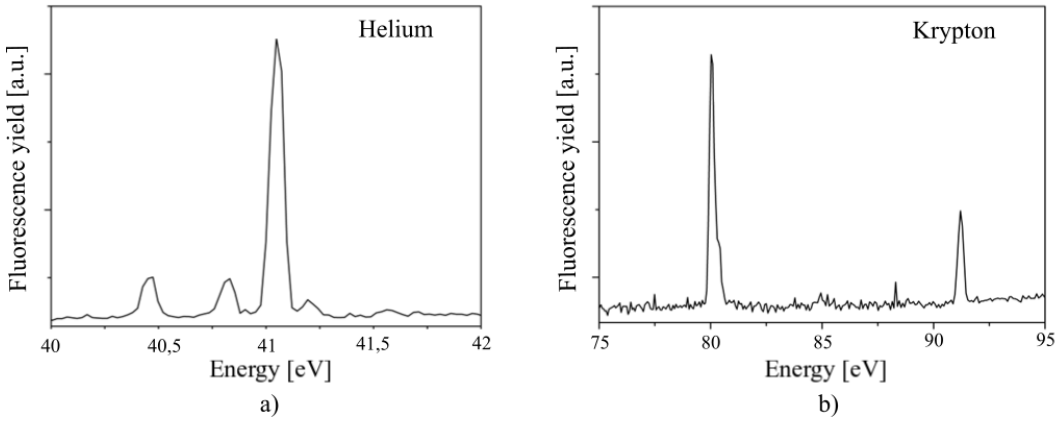

FIGURE 5.5: Fluorescence spectra from gases acquired using the spectrometer. a) He fluorescence spectra on the (3,0) resonance at 64,114 eV. b) Krypton fluorescence spectrum at 91,2 eV.

chamber placed after the experimental chamber and has been mounted collinearly with the direction of FEL beam (i.e., the propagation direction of the FEL and the optical axis of the spectrometer are parallel). The entrance slits of the spectrometer was opened at 40 μm during the experiment. Besides the slits of the spectrometer a couple of horizontal slits have been employed to attenuate the SH contamination from the FEL beam. The grating having a 2400 gr/mm central groove density has been selected to cover the 200 - 800 eV region, being the Carbon K-edge peaked at 285 eV. The sample was scanned to probe pristine graphite for each laser pulse, in order to mitigate the effects of the sample damage. The sample has been moved shot by shot along the beam axis in order to place it was always at the focal point of the FEL.

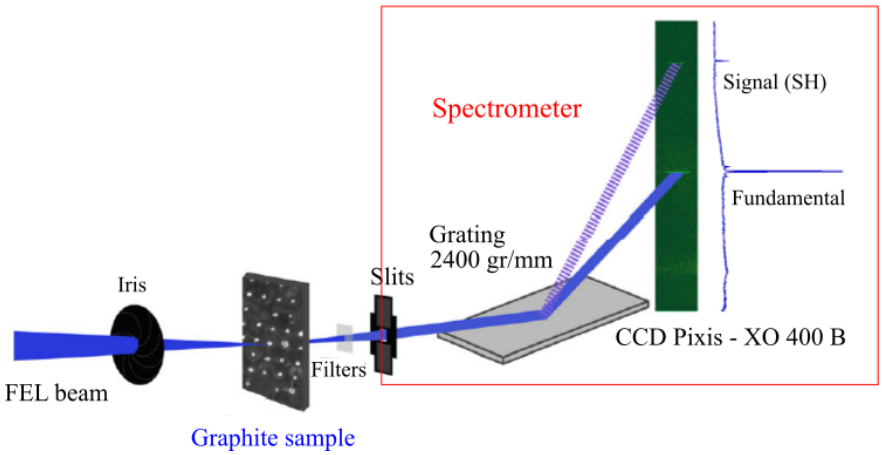

FIGURE 5.6: A schematic of the set-up employed for the SHG experiment.

In order to demonstrate the effects of resonant enhancement of the second harmonic generation, measurements have been made using three photon energies chosen to lay below (260.5 eV), on (284.18 eV) and above (307.86 eV) the Carbon K-edge absorption edge of graphite, as shown in Fig. 5.7 a), where the linear total electron yield x-ray absorption spectrum of a 500 nm graphite sample is reported. On and above the Carbon K-edge absorption edge, the photon energy is resonant with the intermediate state and generates a non-resonant signal enabling transmission experiments, as shown in the schematic energy level diagram of the SHG process in Fig. 5.7 b).

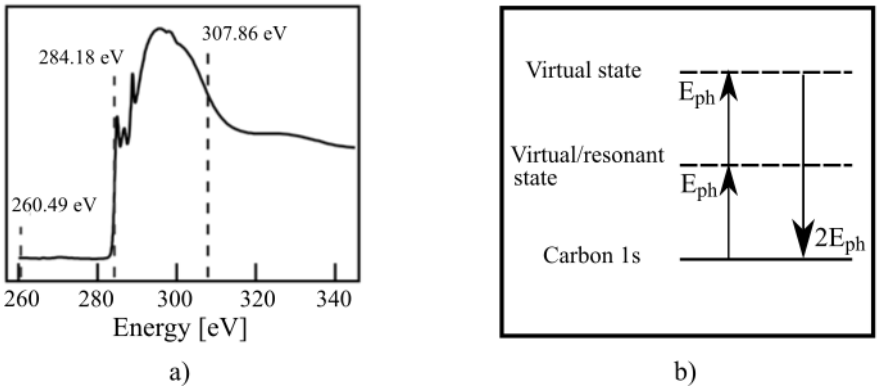

FIGURE 5.7: a) Total electron yield x-ray absorption spectrum of a 500 nm graphite sample. SHG measurements have been made at the three discrete photon energies shown in the dashed lines. b) Schematic energy level diagram of the SHG process.

5.2.2 Results

The dependence of the second harmonic signal on the FEL pulse energy measured for different thicknesses of graphite (from 100 to 720 nm) at 260.49, 284.18 and 307.86 eV is reported in Fig. 5.8 a), 5.8 b) and 5.8 c). The energy of the pulse of the FEL beam before the sample has been calculated from the absolute number of the soft x-ray photons incident on the graphite sample, measured by the spectrometer without the sample in the beam path. The intensity calibration of the spectrometer will be described in detail in the next section. The dashed lines on the plots represent the quadratic fit to the SH response with respect to input intensity at a given photon energy. It is worth to be noted that for each of the reported energies, the power dependence of the SH signal is invariant with the thickness of the sample. This is compatible with the surface sensitivity in a centrosymmetric sample. Moreover, this invariance is also measured at resonant photon energies. When off resonance (at 260.49 eV), a pulse energy of 3.5 μJ per pulse is required for a sufficient SH signal-to-noise ratio, as it is shown in Fig. 5.8 a). At the resonant photon energies, a significant enhancement of the SH signal has been observed. In fact, on and above the resonance, the required pulse energy necessary for the detection of the signal is visibly

lower, 0.7 and 0.3 μJ at 284.18 and 307.86 eV, respectively. The resonance enhancement means that the technique can be used to generate a surface-specific soft x-ray spectrum with sensitivity to the chemical composition of the material. The slope of the linearized power dependence curve (SH response vs. $|inputpower|^2$) is shown in Fig. 5.8 d). In the reported plots the vertical and horizontal error bars represent the standard error of the SH response and the standard deviation of the pulse energies, respectively.

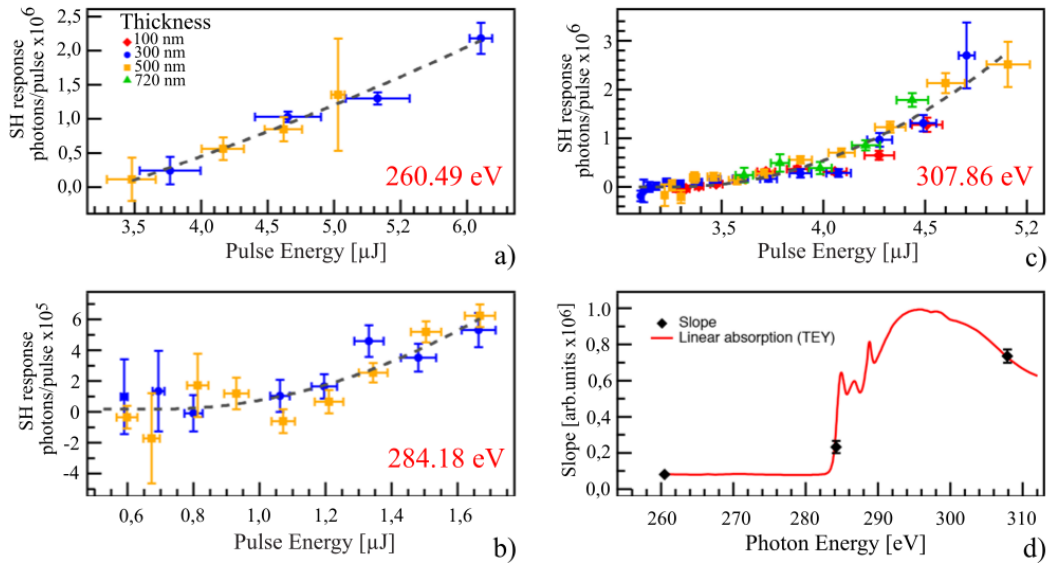

FIGURE 5.8: Pulse energy dependence of soft x-ray SHG. a) The second harmonic response at 260.49 eV , b) The second harmonic response at 284.18 eV. c) The second harmonic response at 307.86 eV. d) The slope of the linearized pulse energy dependence curve for each photon energy.

The illustrated results demonstrate a significant SHG in graphite response in the Soft x-ray regime. It can be concluded that Soft x-ray second harmonic generation is a powerful elemental and chemical specific spectroscopy that is highly symmetry sensitive. This novel technique will allow a new class of interface studies experiments with higher interfacial specificity than other existing soft x-ray methods.

5.2.3 Intensity calibration of the spectrometer

The amount of the signal blocked by the spectrometer entrance slits and horizontal slits placed before the spectrometer was determined using the spatial profiles of the fundamental beam on the spectrometer, along with the size of the horizontal and vertical entrance slits. From this, utilizing the shadow cast on the CCD from the slits, the percentage of the flux transmitted through the slits can be calculated, providing a direct measurement of the fundamental beam intensity. In particular, the contribute I gave in the framework of the data analysis procedure was in analyzing the sets of spectral images at the different wavelengths in order to calculate the photon flux

emitted by the sample. This analysis was done using a MATLAB code and allowed the calculation of the multiplicative factor that must be taken in account for the collection efficiency of the spectrometer and for the optics and detector response. Using this factor, the measurement of the photon flux emitted by the sample as second harmonic signal and propagating toward the spectrometer can be accomplished, once the spectrum on the CCD has been acquired. In the following the method for the estimation of the multiplicative factors is described in detail. For each image of the shots of the different sets, the σ parameters of the interpolating gaussian fits have been calculated. In Fig. 5.9 single shot spectra of the fundamental signal at 307.86 eV and of the second harmonic signal acquired with the spectrometer are reported respectively in the upper and lower part of the picture. Moreover, in the upper part of Fig. 5.10 the fundamental x and y profiles of one shot at 307.86 eV are reported. Whereas, in the lower part of Fig. 5.10 the window considered for the values to fit and the applied gaussian fit are reported. For each set, the number of images having a y-profile gaussian fit with a sigma parameter that is lower than the width of the window from the spatial slit has been subsequently calculated. Only the fits giving a sigma value not larger than the spatial window of the signal have been considered for the calculations. The Gaussian fit doesn't work when, for example, the FEL has an emission with a non-Gaussian spatial mode (e.g. donut-shape profile).

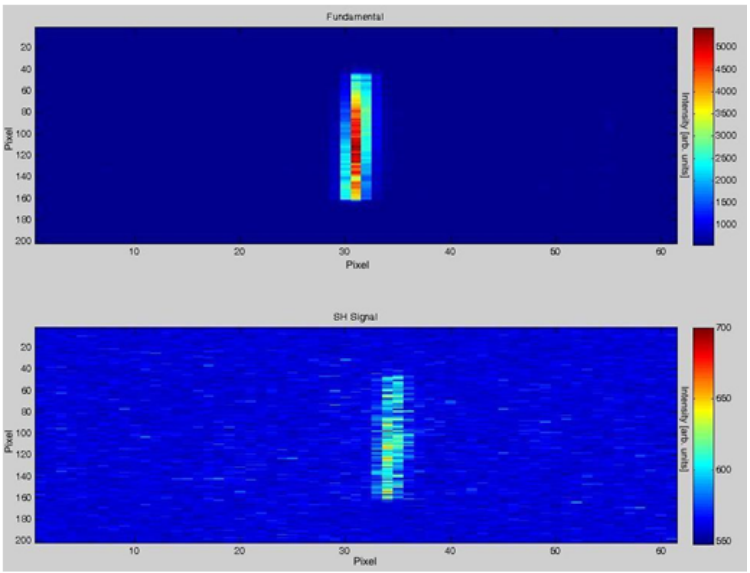

FIGURE 5.9: Single shot spectra of the fundamental signal and of the second harmonic signal acquired with the spectrometer.

At 260.5 eV the gaussian fit works well on 93% of the images. The average σ parameters obtained in the two available sets differ from about 10%, confirming the stability of the FEL emission when the spatial mode is gaussian. The results of the calculation for the two sets of spectral images available at 260.5 eV are reported in Fig. 5.11.

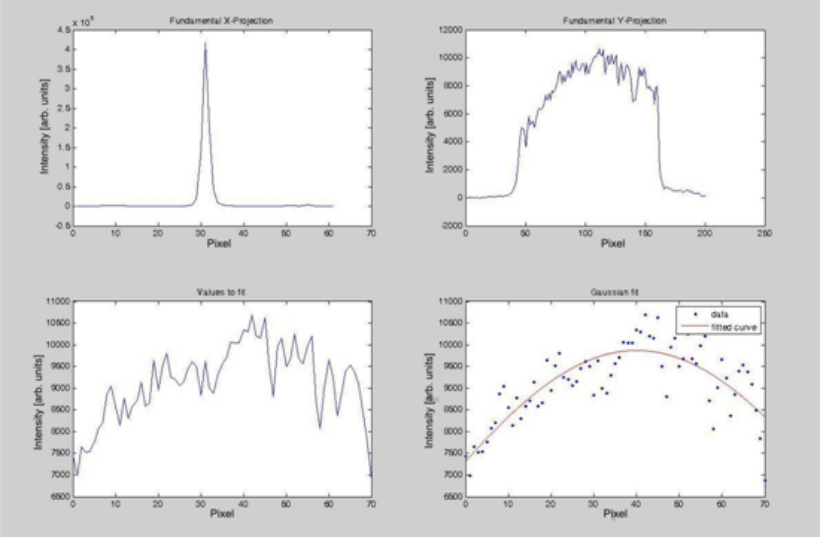

FIGURE 5.10: In the upper part of the picture the fundamental x and y profiles of one shot at 307.86 eV acquired with the spectrometer are reported. In the lower part of the picture the window considered for the values to fit and the applied gaussian fit are respectively reported.

At 284.18 eV the gaussian fit worked well on 85 % of the images. For the calculations only the images with a gaussian profile have been considered. The results of the calculation for the set of spectral images available at 284.18 eV are reported in Fig. 5.12.

At 307.86 eV the gaussian fit works well on 58% of the images, while it diverges for the remaining. Again, for the calculations only the images with a gaussian profile have been considered. The average σ parameters obtained from the 3 different available sets are in very good agreement. The results of the calculation for the three sets of spectral images available at 307.86 eV are reported in Fig. 5.13.

Finally, the multiplicative factors which allows to calculate the photon flux before the slits has been estimated. The fraction of photons cut by the horizontal and vertical slits has been obtained, knowing the divergence of the beam. The profiles have been projected from the CCD plane to the entrance slits plane and to the horizontal slits plane and the fraction of photons transmitted has been calculated. The effect of the slits on the FEL beam, supposed to have a two-dimensional gaussian shape at the vertical (or horizontal) slit plane of the spectrometer is schematically shown in Fig. 5.14. The slits apertures are W_h and W_v, respectively for the horizontal and vertical slits. These contributions are joined together to obtain the multiplicative factor that gives the number of photons before the spectrometer, once the number of photons on the CCD is calculated from the measured intensities. The number of photons on the CCD has been obtained taking in to account the total throughput of the instrument, defined as counts on the detector per input photon. The diffraction grating efficiency and the CCD response have been measured at the facility available at CNR-IFN Padova. The pulse energies obtained from the CCD counts has to

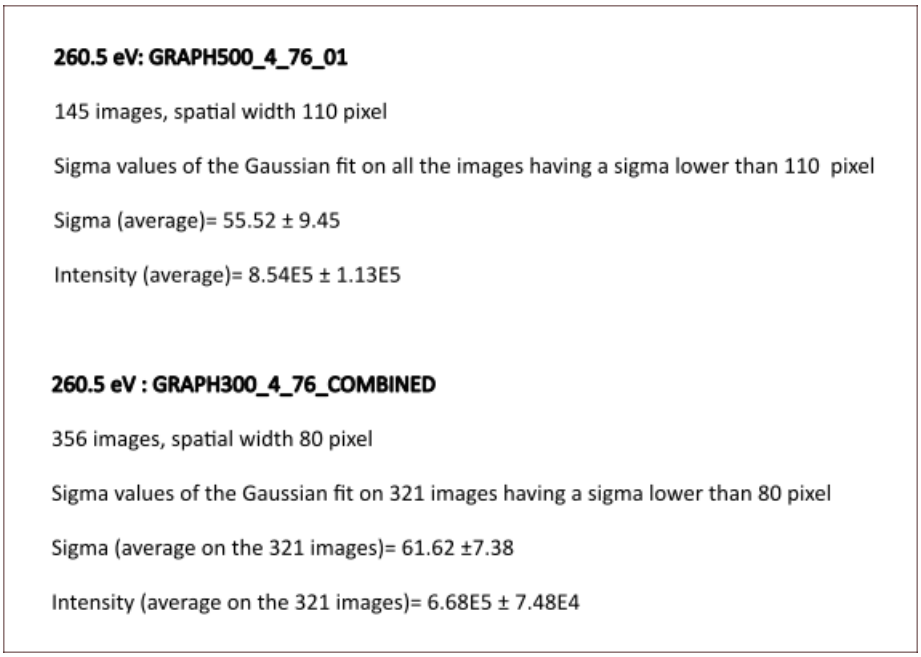

FIGURE 5.11: Results of the analysis for the two sets of spectral images available at 260.5 eV.

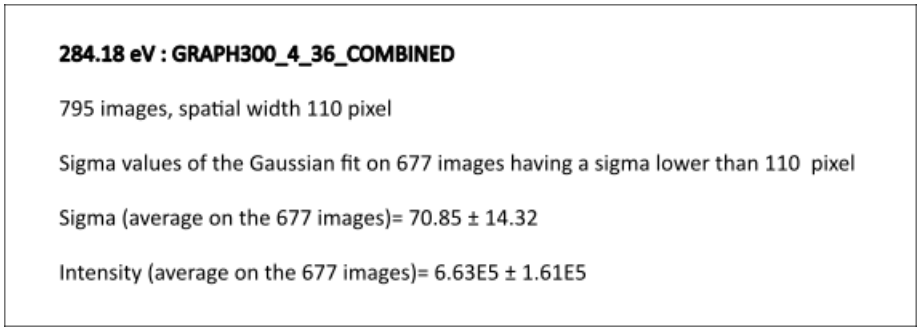

FIGURE 5.12: Results of the analysis for the set of spectral images available at 284.18 eV.

be multiplied by the multiplicative factor reported in tab. 5.3.

5.3 Conclusions

The design and characterization of a portable and compact photon spectrometer to be used for XUV/soft X-ray photon in-photon out experiments at synchrotron and FEL sources have been reported. The instrument has been fully characterized with synchrotron radiation by measuring fluorescence spectra both from solid and gas targets. These spectra are in full agreement with data reported in the literature. Besides the use in synchrotron beamlines, the instrument has been specially designed to be interfaced on the beamlines at FERMI, where several research activities in the field of atomic and molecular physics and in condensed matter has been conducted.

307.86 eV: GRAPH800_4_02_004

681 images, spatial width 110 pixel

Sigma values of the Gaussian fit on 438 images having a sigma lower than 110 pixel

Sigma(average on the 438 images)= 73.06 ± 16.17

Intensity(average on the 438 images)= 1.28E6 ± 2.99E5

307.86 eV: GRAPH720_4_02_002_003_COMBINED

379 images, spatial width 110 pixel

Sigma values of the Gaussian fit on 246 images having a sigma lower than 110 pixel

Sigma(average on the 246 images)= 75.03 ± 14.74

Intensity(average on the 246 images)= 1.70E6 ± 3.10E5

307.86 eV :GRAPH300_4_02_001

500 images, spatial width 110 pixel

Sigma values of the Gaussian fit on 228 images having a sigma lower than 110 pixel

Sigma(average on the 228 images)= 75.03 ± 17.25

Intensity(average on the 228 images)= 1.18E6 ± 4.00E5

FIGURE 5.13: Results of the analysis for the set of spectral images available at 307.86 eV.

Recently, the apparatus has been used for a Second Harmonic Generation in graphite experiment described clearly in the previous sections. The reported results demonstrate the proper operation of the instrument and the success of the experiment. The methods employed to provide the intensity calibration of the spectrometer, in order to calculate the intensity of the photon flux emitted by the sample in second harmonic, have been exhaustively described. XUV/soft X-ray SHG has been demonstrated to be a symmetry sensitive spectroscopic technique which will allow a new class of interface studies experiments with higher interfacial specificity than other existing soft X-ray approaches.

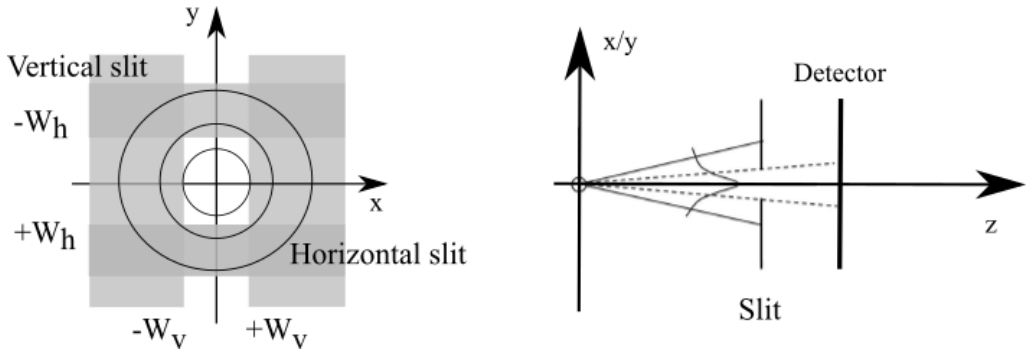

FIGURE 5.14: The effect of the slits on the FEL beam, supposed to have a two-dimensional gaussian shape at the vertical (or horizontal) slits plane of the spectrometer.

TABLE 5.3: Calculated multiplicative factors

DATASET	**MULTIPLICATIVE FACTOR**
260.5 eV: DATASET 1	74
260.5 eV : DATASET 2	105
284.18 eV : DATASET 1	105
307.86 eV: DATASET 1	114
307.86 eV: DATASET 2	116
307.86 eV: DATASET 3	116

Chapter 6

General conclusions

In this dissertation the work performed in the framework of the development of spectroscopic instrumentation for ultrafast pulses in the XUV domain has been presented. An introduction has been given and the theory behind each one of the three main activities that have been carried out during the PhD period has been reported. The work on the installation, development and characterization of ultrafast instrumentation for handling, conditioning and detection of ultrashort pulses has been described in detail. Moreover, the technical and scientific advances achieved, as well as the experimental results obtained, have been reported and discussed. In summary, ultrafast technologies in the XUV domain has become very useful tools for the study of the dynamics of atoms and molecules in a wide range of applications. Research and developments of ultrafast instrumentation are clearly essential for providing novel approaches for high-resolution time-domain spectroscopy. It can be expected that ultrafast technology will gain further relevance and will allow new developments on the study of ultrafast dynamics in the matter.

Chapter 7

Publications

List of publications on international journals and volumes

- J1: F. Frassetto, P. Miotti, L. Poletto, "Compression of extreme-ultraviolet ultrashort pulses by grating configurations", REVIEW PAPER, J. Spectrosc. Volume 2015, Article ID 495914, 9 pages, http://dx.doi.org/10.1155/2015/495914 (2015)

- J2: A. Kivimäki, M. Coreno, P. Miotti, F. Frassetto, L. Poletto, C. Stråhlman, M. de Simone, and R. Richter, "The multielectron character of the S 2p $\rightarrow$ 4eg shape resonance in the SF6 molecule studied via detection of soft x-ray emission and neutral high-Rydberg fragments", Journal of Electron Spectroscopy and Related Phenomena 209, 26-33 (2016)

- J3: D. Gauthier, E. Allaria, M. Coreno, I. Cudin, H. Dacasa, M. B. Danailov, A. Demidovich, S. Di Mitri, B. Diviacco, E. Ferrari, P. Finetti, F. Frassetto, D. Garzella, S. Künzel, V. Leroux, B. Mahieu, N. Mahne, M. Meyer, T. Mazza, P. Miotti, G. Penco, L. Raimondi, P. R. Ribič, R. Richter, E. Roussel, S. Schulz, L. Sturari, C. Svetina, M. Trovò, P. A. Walker, M. Zangrando, C. Callegari, M. Fajardo, L. Poletto, P. Zeitoun, L. Giannessi and G. De Ninno "Chirped pulse amplification in an extreme-ultraviolet free-electron laser" Nature Communications 7, Article number: 13688 (2016). DOI:10.1038/ncomms13688

- J4: L. Poletto, N. Fabris, F. Frassetto P. Miotti "Design Study of Time-Preserving Grating Monochromators for Ultrashort Pulses in the Extreme-Ultraviolet and Soft X-Rays" Photonics 4(1):14 March 2017. DOI: 10.3390/photonics4010014

- J5: D. Gauthier, P. R. Ribič, G. Adhikary, A. Camper, C. Chappuis, R. Cucini, L. F. DiMauro, G. Dovillaire, F. Frassetto, R. Gèneaux, P. Miotti, L. Poletto, B. Ressel, C. Spezzani, M. Stupar, T. Ruchon and G. De Ninno "Tunable orbital angular momentum in high-harmonic generation" Nature Communications 8, Article number: 14971 (2017). DOI:10.1038/ncomms14971

- J6: R.K. Lam, S.L. Raj, T.A. Pascal, C.D. Pemmaraju, L. Foglia, A. Simoncig, N. Fabris, P. Miotti, C.J. Hull, A.M. Rizzuto, J.W. Smith, R. Mincigrucci, C. Masciovecchio, A. Gessini, E. Allaria, G. De Ninno, B. Diviacco, E. Roussel, S.

Spampinati, G. Penco, S. Di Mitri, M. Trovò, M. Danailov, S.T. Christensen, D. Sokaras, T.-C. Weng, M. Coreno, L. Poletto, W.S. Drisdell, D. Prendergast, L. Giannessi, E. Principi, D. Nordlund, R.J. Saykally, C.P. Schwartz, "Soft X-ray Second Harmonic Generation as an Interfacial Probe", Phys. Rev. Lett. 120, 023901 (2018)

- J7: R. Lam, S. Raj, T. Pascal, C.D. Pemmaraju, L. Foglia, A. Simoncig, N. Fabris, P. Miotti, C. Hull, A. Rizzuto, J. Smith, R. Mincigrucci, C. Masciovecchio, A. Gessini, G. De Ninno, B. Diviacco, E. Roussel, S. Spampinati, G. Penco, S. Di Mitri, M. Trovo, M. Danailov, S. Christensen, D. Sokaras, T.-C. Weng, M. Coreno, L. Poletto, W. Drisdell, D. Prendergast, L. Giannessi, E. Principi, D. Nordlund, R. Saykally, and C. Schwartz, "Two-photon absorption of soft X-ray free electron laser radiation by graphite near the carbon K-absorption edge", Chem. Phys. Letters 703, 112-116 (2018)

List of publications on volumes

- V1: D. Gauthier, P. Rebernik Ribič, G. Adhikary, A. Camper, C. Chappuis, R. Cucini, L.F. DiMauro, G. Dovillaire, F. Frassetto, R. Géneaux, P. Miotti, L. Poletto, B. Ressel, C. Spezzani, M. Stupar, T. Ruchon, and G. De Ninno, "Tunable orbital angular momentum in high-harmonic generation", ELETTRA Highlights 2016-2017, 138-139 (2017)

- V2: D. Gauthier, E. Allaria, M. Coreno, I. Cudin, H. Dacasa, M.B. Danailov, A. Demidovich, S. Di Mitri, B. Diviacco, E. Ferrari, P. Finetti, F. Frassetto, D. Garzella, S. Kunzel, V. Leroux, B. Mahieu, N. Mahne, M. Meyer, T. Mazza, P. Miotti, G. Penco, L. Raimondi, P. Rebernik Ribic, R. Richter, E. Roussel, S. Schulz, L. Sturari, C. Svetina, M. Trovò, P.A. Walker, M. Zangrando, C. Callegari, M. Fajardo, L. Poletto, P. Zeitoun, L. Giannessi, G. De Ninno, "Chirped pulse amplification in a XUV free-electron laser", ELETTRA Highlights 2016-2017, 140-141 (2017)

List of publications on conference proceedings

- C1: S. Bonora, N. Fabris, F. Frassetto, E. Giovine, P. Miotti, M. Quintavalla, L. Poletto, "Design of compressors for FEL pulses using deformable gratings", SPIE Proc. 10237, X-Ray Free-Electron Lasers: Advances in Source Development and Instrumentation IV, 102370T (2017)

- C2: L. Poletto, S. Bonora, N. Fabris, F. Frassetto, E. Giovine, P. Miotti, and M. Quintavalla, "Design of deformable-grating compressors for free-electron-laser pulses", in Conference on Lasers and Electro-Optics CLEO Europe 2017, OSA Technical Digest Series, paper JSI-P.4 (2017)

- C3: D. Gauthier, P. Rebernik Ribic, G. Adhikary, A. Camper, C. Chappuis, R. Cucini, L.F. Di Mauro, G. Dovillaire, F. Frassetto, R.Geneaux, P. Miotti, L. Poletto, B. Ressel, C. Spezzani, M. Stupar, T. Ruchon, G. De Ninno, "Tunable

orbital angular momentum in high-harmonic generation", ICOAM17 - 4th International Conference on Optical Angular Momentum, Anacapri (Italy), 18-22 September 2017, pag. 68

- C4: P. Miotti, N. Fabris, F. Frassetto, P. Zuppella, L. Poletto, "Soft x-ray grating compressors for free-electron-laser pulses", SPIE Proc. 10386, Advances in X-Ray/EUV Optics and Components XII, 10386-26 (2017)

- C5: P. Miotti, F. Cilento, R. Cucini, F. Frassetto, D. Kopir, D. Payne, T. Pincelli, G. Panaccione, L. Poletto, "A Novel high order harmonic source for time- and angle-resolved photoemission experiments", OSA High-brightness Sources and Light-driven Interactions Congress 2018, Strasbourg, 26-328 March 2018, EW2B.5

- C6: P. Miotti, N. Fabris, F. Frassetto, E. Giovine, C. Spezzani, P. Zuppella, and L. Poletto, "Fabrication and performances of laminar gratings for the soft X-ray region", IWXM 2018 – 6th International Workshop on X-Ray Optics and Metrology, National Synchrotron Radiation Research Center, Hsinchu, Taiwan, June 6-9, 2018, Book of abstracts, 57 (2018)

- C7: P. Miotti, L. Poletto, F. Frassetto, and N. Fabris, "Design and realization of a XUV plane-grating monochromator at variable subtended angle", Synchrotron Radiation Instrumentation 2018 Conference, 10-15 June 2018, Taipei, Taiwan, Book of poster abstracts, PD2-09, 239 (2018)

Bibliography

[1] Marciak-Kozlowska, J.; Kozlowski, M., *From Femto-To Attoscience and Beyond*, Nova Science Publisher: Hauppauge, NY, USA, (2009).

[2] Krausz, F.; Ivanov, M., *Attosecond physics*, Rev. Mod. Phys. 81, 163–234 (2009)

[3] Jaeglè, P., *Coherent Sources of XUV Radiation*, Springer: New York, NY, USA, 277–344 (2006).

[4] Ackermann, W. et al., *Operation of a free-electron laser from the extreme ultraviolet to the water window*, Nat.Photonics 1, 336–342 (2007).

[5] Emma, P. et al., *First lasing and operation of an angstrom-wavelength free-electron laser*, Nat. Photonics 4, 6641–6647 (2010).

[6] K. Midorikawa, *High-Order Harmonic Generation and Attosecond Science*, Japanese J. Appl. Phys., 50 (2011).

[7] Sansone, G.; Poletto, L.; Nisoli, M., *High-energy attosecond light sources*, Nat. Photonics 5, 655–663 (2011).

[8] D. Gauthier, E. Allaria, M. Coreno, I. Cudin, H. Dacasa, M. B. Danailov, A. Demidovich, S. Di Mitri, B. Diviacco, E. Ferrari, P. Finetti, F. Frassetto, D. Garzella, S. Künzel, V. Leroux, B. Mahieu, N. Mahne, M. Meyer, T. Mazza, P. Miotti, G. Penco, L. Raimondi, P. R. Ribič, R. Richter, E. Roussel, S. Schulz, L. Sturari, C. Svetina, M. Trovò, P. A. Walker, M. Zangrando, C. Callegari, M. Fajardo, L. Poletto, P. Zeitoun, L. Giannessi and G. De Ninno, *Chirped pulse amplification in an extreme-ultraviolet free-electron laser*, Nature Communications 7, Article number: 13688 (2016).

[9] Corkum P. B., *Plasma perspective on strong field multiphoton ionization*, Phys. Rev. Lett. 71 (1994).

[10] Kulander K.C., Schafer K.J. and Krause J.L., *Proc.Work-shop on Super-Intense Laser Atom Physics (SILAP) III*, ed. B. Piraux (New York: Plenum) pp 95–110 (1993).

[11] Salièeres P., L'Huillier A. and Lewenstein M., *Coherence Control of High-Order Harmonics*, Phys. Rev. Lett. 74, 3776 (1995).

[12] Lewenstein M., Salièeres P. and L'Huillier A., *Phase of the atomic polarization in high-order harmonic generation*, Phys. Rev. A 52, 4747 (1995).

[13] Salièeres P et al., *Feynman's Path-Integral Approach for Intense-Laser-Atom Interactions*, Science 292, 902 (2001).

[14] Nisoli M. et al., *High-Brightness High-Order Harmonic Generation by Truncated Bessel Beams in the Sub-10-fs Regime*, Phys. Rev. Lett. 88, 033902 (2002).

[15] Zhou J. et al. *Enhanced High-Harmonic Generation Using 25 fs Laser Pulses*, Phys. Rev. Lett. 76, 752 (1996).

[16] Nisoli M. et al., *Spectral analysis of high-order harmonics generated by 30-fs and sub-10-fs laser pulses*, Appl. Phys. B 70, 215 (2000).

[17] Tamaki Y. et al., *Highly Efficient, Phase-Matched High-Harmonic Generation by a Self-Guided Laser Beam*, Phys. Rev. Lett. 82, 1422 (1999).

[18] Tosa V., Takahashi E., Nabekawa Y. and Midorikawa K., *Generation of high-order harmonics in a self-guided beam*, Phys. Rev. A 67, 063817 (2003).

[19] Strickland, D. and Mourou, G., *Compression of amplified chirped optical pulses*, Opt. Commun. 56, 219 (1985).

[20] Zholents A. A. and Fawley W.M., *Proposal for Intense Attosecond Radiation from an X-Ray Free-Electron Laser*, Phys. Rev. Lett. 92, 224801 (2004)

[21] Emma, P. et al., *Femtosecond and Subfemtosecond X-Ray Pulses from a Self-Amplified Spontaneous EmissionBased Free-Electron Laser*, Phys. Rev. Lett. 92, 074801 (2004).

[22] Saldin E.L., Schneidmiller E. A., Yurkov M. V., *Self-amplified spontaneous emission FEL with energy-chirped electron beam and its application for generation of attosecond x-ray pulses*, Phys. Rev. ST Accel. Beams 9, 050702 (2006).

[23] Thompson N.R. and McNeil B.W.J, *Mode Locking in a Free-Electron Laser Amplifier*, Phys. Rev. Lett. 100, 20390 (2008).

[24] Prat E. and Reiche S. , *Simple Method to Generate Terawatt-Attosecond X-Ray Free-Electron-Laser Pulses*, Phys.Rev. Lett. 100, 203901 (2008).

[25] Gauthier D. et al., *Spectro-temporal shaping of seeded free-electron laser pulses*, Phys. Rev. Lett. 98, 115 (2015).

[26] Yu L.H., Johnson E., Li D., Umstadter D. , *Femtosecond free-electron laser by chirped pulse amplification*, Phys. Rev. E Stat. Phys. Plasmas Fluids Relat. Interdiscip. Topics 49(5), 4480-4486 (1994).

[27] Moore, G. T., *Frequency chirping of the free-electron laser*, Phys. Rev. Lett. 60, 1825 (1988).

[28] E.L. Saldin, E.A. Schneidmiller, M.V. Yurkov, *The Physics of Free Electron Lasers*, Springer, Berlin-Heidelberg (2000)

[29] K.J. Kim, *Three-Dimensional Analysis of Coherent Amplification and Self-Amplified Spontaneous Emission in Free-Electron Lasers*, Phys. Rev. Lett. 57, 1871 (1986).

[30] S. Krinsky and L.H. Yu, *Output power in guided modes for amplified spontaneous emission in a single-pass free-electron laser*, Phys. Rev. A35, 3406 (1987).

[31] R. Bonifacio, C. Pellegrini and L.M. Narducci, *Collective instabilities and high-gain regime in a free electron laser*, Opt. Commun. 50, 373 (1984).

[32] S. Reiche, *Overview of seeding methods*, Proceedings of IPAC2013, Shanghai, China (2013).

[33] Shu, X. et al., *Chirped pulse amplification in a free electron laser amplifier*, of Electron Spectroscopy and Related Phenomena 184, 350 (2011).

[34] Ratner, D. et al. , *Laser phase errors in seeded free electron lasers*, Phys. Rev. ST Accel. Beams 15, 030702 (2012).

[35] Gauthier, D. et al., *Direct spectrotemporal characterization of femtosecond extreme-ultraviolet pulses*, Phys. Rev. A 88, 033849 (2013).

[36] U. Bergmann and P. Glatzel, *X-ray emission spectroscopy*, Photosynth. Res. 102, 255 (2009).

[37] J. Yano and V. K. Yachandra, *X-ray absorption spectroscopy*, Photosynth. Res. 102, 241 (2009).

[38] W. Schuelke, *Electron Dynamics by Inelastic X-Ray Scattering*, Oxford University Press, Oxford (2007).

[39] F. De Groot and A. Kotani, *Core Level Spectroscopy of Solids*, CRC Press (2008).

[40] M. Beye, F. Sorgenfrei, W. F. Schlotter, W. Wurth, and A. Föhlisch, *The liquid-liquid phase transition in silicon revealed by snapshots of valence electrons*, Proc. Natl. Acad. Sci. U.S.A. 107, 16772 (2010).

[41] M. Altarelli, *Opportunities for resonant elastic X-ray scattering at X-ray free-electron lasers*, Eur. Phys. J.: Spec. Top. 208, 351 (2012)

[42] D. Zhu, M. Cammarata, J. M. Feldkamp, D. M. Fritz, J. B. Hastings, S. Lee, H. T. Lemke, A. R. James, L. Turner, and Y. Feng, *A single-shot transmissive spectrometer for hard x-ray free electron lasers*, Appl. Phys. Lett. 101, 034103 (2012)

[43] K. Kunnus, I. Rajkovic, S. Schreck, W. Quevedo, S. Eckert, M. Beye, E. Suljoti, C. Weniger, C. Kalus, S. Grübel, M. Scholz, D. Nordlund, W. Zhang, R. W. Hartsock, K. J. Gaffney, W. F. Schlotter, J. J. Turner, B. Kennedy, F. Hennies, S. Techert, P. Wernet, and A. Föhlisch, *A setup for resonant inelastic soft x-ray scattering on liquids at free electron laser light sources*, Rev. Sci. Instrum. 83, 123109 (2012).

[44] T. Katayama, T. Anniyev, M. Beye, R. Coffee, M. Dell'Angela, A. Föhlisch, J. Gladh, S. Kaya, O. Krupin, A. Nilsson, D. Nordlund,W. F. Schlotter, J. A. Sellberg, F. Sorgenfrei, J. J. Turner, W. Wurth, H. Öström, and H.Ogasawara, *Ultrafast soft X-ray emission spectroscopy of surface adsorbates using an X-ray free electron laser*, J. Electron Spectrosc. Relat. Phenom. 187, 9–14 (2013).

[45] W. Zhang, V. Carravetta, O. Plekan, V. Feyer, R. Richter, M. Coreno, and K. C. Prince, J. , *Electronic structure of aromatic amino acids studied by soft x-ray spectroscopy*, Chem. Phys. 131, 035103 (2009).

[46] M. Coreno, M. de Simone, R. Coates, M. S. Denning, R. G. Denning, J. C. Green, C. Hunston, N. Kaltsoyannis, and A. Sella, *Variable Photon Energy Photoelectron Spectroscopy and Magnetism of YbCp3 and LuCp3*, Organometallics 29, 4752 (2010).

[47] L. Ravagnan, T. Mazza, G. Bongiorno, M. Devetta, M. Amati, P. Milani, P.Piseri, M. Coreno, C. Lenardi, F. Evangelista, and P. Rudolf, *sp hybridization in free carbon nanoparticles—presence and stability observed by near edge X-ray absorption fine structure spectroscopy*, Chem. Commun. 47, 2952 (2011).

[48] P. Glatzel, M. Sikora, and M. Fernandez-Garcia, *Resonant X-ray spectroscopy to study K absorption pre-edges in 3d transition metal compounds*, Eur. Phys. J.: Spec. Top. 169, 207 (2009).

[49] T. Kita, T. Harada, N. Nakano, and H. Kuroda, *Mechanically ruled aberration-corrected concave gratings for a flat-field grazing-incidence spectrograph*, Appl. Opt. 22, 512 (1983).

[50] J.H. Underwood, *Spectrographs and monochromators using varied line spacing gratings*, Vacuum Ultraviolet Spectroscopy II, J.A. Samson and D.L. Ederer editors, 55-72 Elsevier (1999).

[51] J. F. Wu, Y. Y. Chen, and T. S. Wang, *Flat field concave holographic grating with broad spectral region and moderately high resolution*, Appl. Opt. 51(4), 509–514 (2012).

[52] P. A. Franken, A. E. Hill, C.W. Peters, and G. Weinreich, *Generation of Optical Harmonics*, Phys. Rev. Lett. 7, 118 (1961).

[53] Y.-R. Shen, *Fundamentals of Sum-Frequency Spectroscopy*, Cambridge University Press, Cambridge, England (2016).

[54] T. E. Glover, D.M. Fritz, M. Cammarata, T. K. Allison, S.Coh, J. M. Feldkamp, H. Lemke, D. Zhu, Y. Feng, R. N.Coffee, M. Fuchs, S. Ghimire, J. Chen, S. Shwartz, D. A.Reis, S. E. Harris, and J. B. Hastings, *X-ray and optical wave mixing*, Nature (London) 488, 603 (2012).

[55] R.K. Lam, S.L. Raj, T.A. Pascal, C.D. Pemmaraju, L. Foglia, A. Simoncig, N. Fabris, P. Miotti, C.J. Hull, A.M. Rizzuto, J.W. Smith, R. Mincigrucci, C. Masciovecchio, A. Gessini, E. Allaria, G. De Ninno, B. Diviacco, E. Roussel, S. Spampinati, G. Penco, S. Di Mitri, M. Trovò, M. Danailov, S.T. Christensen, D. Sokaras, T.-C. Weng, M. Coreno, L. Poletto, W.S. Drisdell, D. Prendergast, L. Giannessi, E. Principi, D. Nordlund, R.J. Saykally, C.P. Schwartz, *Soft X-ray Second Harmonic Generation as an Interfacial Probe*, Phys. Rev. Lett. 120, 023901 (2018).

[56] A. Damascelli, Z. Hussain, and Z. X. Shen, *Angle-resolved photoemission studies of the cuprate superconductors*, Rev. Mod. Phys. 75, 473 (2003).

[57] M. Hajlaoui, E. Papalazarou, J. Mauchain, Z. Jiang, I. Miotkowski, Y.P. Chen, A. Taleb-Ibrahimi, L. Perfetti, and M. Marsi, *Time resolved ultrafast ARPES for the study of topological insulators: The case of Bi2Te3*, Eur. Phys. J. Special Topics 222, 1271–1275 (2013).

[58] Wieland M., Frueke R., Wilhein T., Spielmann C., Pohl M., Kleinenberg U., *Submicron extreme ultraviolet imaging using high-harmonic radiation*, Appl. Phys. Lett. 81, 2520–2522 (2002).

[59] Bartels R., Backus S., Zeek E., Misoguti L., Vdovin G., Christov I.P., Murnane M.M., Kapteyn H.C., *Shaped-pulse optimization of coherent emission of high-harmonic soft X-rays*, Nature 406, 164–166. (2000).

[60] Gaudin J., Rehbein S., Guttmann P., Godé S., Schneider G., Wernet P., Eberhardt W., *Selection of a single femtosecond high-order harmonic using a zone plate based monochromator*, J. Appl. Phys. 104, 033112 (2008).

[61] Sekikawa T., *Gratings for ultrashort coherent pulses in the extreme ultraviolet*, Optical Technologies for Extreme-Ultraviolet and Soft X-ray Coherent Sources 1st ed.; Canova, F., Poletto, L., Eds.; Springer: Berlin, Germany, pp. 175–193 (2015).

[62] T. Sekikawa, T. Okamoto, E. Haraguchi, M. Yamashita, and T. Nakajima, *Two-photon resonant excitation of a doubly excited state in He atoms by high-harmonic pulses*, Opt. Express 16, 21922–21929 (2008).

[63] W. Cash, *Echelle spectrographs at grazing incidence*, Appl. Opt. 21, 710–717 (1982)

[64] L. Poletto and F. Frassetto, *Time-preserving monochromators for ultrafast extreme-ultraviolet pulses*, Appl. Opt. 49, 5465–5473 (2010)

[65] L. Poletto, G. Tondello, and P. Villoresi *Optical design of a spectrometer–monochromator for the extreme-ultraviolet and soft-xray emission of high-order harmonics*, Appl. Opt. 42, 6367–6373 (2003).

[66] W. Werner, *X-ray efficiencies of blazed gratings in extreme off-plane mountings*, Appl. Opt. 16, 2078–2080 (1977).

[67] M. Pascolini, S. Bonora, A. Giglia, N. Mahne, S. Nannarone, L. Poletto, *Gratings in the conical diffraction mounting for an EUV time-delay compensated monochromator*, Appl. Opt. 45, 3253-3262 (2006)

[68] L. Poletto, N. Fabris, F. Frassetto P. Miotti, *Design Study of Time-Preserving Grating Monochromators for Ultrashort Pulses in the Extreme-Ultraviolet and Soft X-Rays*, Photonics 4(1):14 (2017).

[69] F. Cilento, A. Crepaldi, G. Manzoni, A. Sterzi, M. Zacchigna, Ph. Bugnon, H. Berger, and F. Parmigiani, *Advancing non-equilibrium ARPES experiments by a 9.3 eV coherent ultrafast photon source*, J. Electr. Spectrosc. Relat. Phenom. 207, 7 (2016).

[70] T. Pincelli, V. N. Petrov, G. Brajnik, R. Ciprian, V. Lollobrigida, P. Torelli, D. Krizmancic, F. Salvador, A. De Luisa, R. Sergo, A. Gubertini, G. Cautero, S. Carrato, G. Rossi, and G. Panaccione, *Design and optimization of a modular setup for measurements of three-dimensional spin polarization with ultrafast pulsed sources*, Rev. Sci. Instrum. 87, 035111 (2016).

[71] Poletto L., Boscolo A., and Tondello G., *Characterization of a Charge-Coupled-Device detector in the 1100-0.14 nm (1-eV to 9-keV) spectral region.*, Appl. Opt. 38, 29-36 (1999).

[72] D. Desiderio, S.Difonzo, B. Dlviacco, W. Jark, J. Krempasky, R. Krempaska, F. Lama, M. Luce, H. C. Mertins, M. Placentini, T.Prosperi, S. Rinaldi, G. Soullie, F. Schäfers, F. Schmolle, L. Stichauer, S. Turchini, R. P. Walker and N. Zema, *The elettra circular polarization beamline and electromagnetic elliptical wiggler insertion device*, Synchrotron Radiation News Vol. 12 , Iss. 4, (1999).

[73] Paola Zuppella, Elisabetta Pasqualotto, Sara Zuccon, Francesca Gerlin, Alain Jody Corso, Matteo Scaramuzza, Alessandro De Toni, Alessandro Paccagnella, and Maria Guglielmina Pelizzo, *Palladium on Plastic Substrates for Plasmonic Devices*, Sensors (Basel). 15(1): 1138–1147 (2015).

[74] Maquet A. and Taleb R. *Two-colour IR+XUV spectroscopies: the soft-photon approximation*, Journal of Modern Optics 54, 1487 (2007).

[75] Ratner D. et al., *Laser phase errors in seeded free electron lasers*, Phys. Rev. ST Accel. Beams 15, 030702 (2012).

[76] L. Foglia, M. Kiskinova, C. Masciovecchio, R. Mincigrucci, D. Naumenko, E. Pedersoli, A. Simoncig and F. Bencivenga, *Characterization of ultrafast free-electron laser pulses using extreme-ultraviolet transient gratings*, J. Synchrotron Rad. 25, 32-38 (2018).

[77] A. Simoncig, R. Mincigrucci, E. Principi, F. Bencivenga, A.Calvi, L. Foglia, G. Kurdi, L. Raimondi, M. Manfredda, N.Mahne, R. Gobessi, S. Gerusina, C. Fava,

M. Zangrando, A.Matruglio, S. Dal Zilio, V. Masciotti, and C. Masciovecchio, *The EIS beamline at the seeded free-electron laser FERMI*, Proc. SPIE Int. Soc. Opt. Eng. 10243, 102430L (2017).

[78] C. Masciovecchio et al., *EIS: the scattering beamline at FERMI*, J. Synchrotron Radiat. 22, 553 (2015).

[79] T. Kita, T. Harada, N. Nakano, and H. Kuroda, *Mechanically ruled aberration-corrected concave gratings for a flat-field grazing-incidence spectrograph*, Appl. Opt. 22, 512 (1983).

[80] R. R. Blyth, R. Delaunay, M. Zitnik, J. Krempasky, R. Krempaska, J.Slezak, K. C. Prince, R. Richter, M. Vondracek, R. Camilloni, L. Avaldi, M. Coreno, G. Stefani, C. Furlani, M. de Simone, S. Stranges, and M.-Y.Adam, *The high resolution Gas Phase Photoemission beamline, Elettra*, Electron Spectrosc. Relat. Phenom. 101–103, 959 (1999).

[81] J. A. Carlisle, A. Chaiken, R. P. Michel, L. J. Terminello, J. J. Jia, T. A. Callcott, and D. L. Ederer, *Soft-x-ray fluorescence study of buried silicides in antiferromagnetically coupled Fe/Si multilayers*, Phys. Rev. B 53, R8824 (1996).

[82] Y. Muramatsu, M. Oshima, and H. Kato, *Resonant x-ray Raman scattering in B K alpha emission spectra of boron oxide (B2O3) excited by undulator radiation*, Phys. Rev. Lett. 71, 448 (1993).

[83] K.-H. Schartner, B. Zimmermann, S. Kammer, S. Mickat, H. Schmoranzer, A. Ehresmann, H. Liebel, R. Follath, and G. Reichardt, *Radiative cascades from doubly excited He states*, Phys. Rev. A 64,040501 (2001).